ABSTRACT

Title of Document: PROGNOSTICS OF INSULATED GATE BIPOLAR TRANSISTORS.

Nishad Patil, Doctor of Philosophy, 2011

Directed By: Professor Michael Pecht
Department of Mechanical Engineering

Insulated gate bipolar transistors (IGBTs) are the devices of choice for medium and high power, low frequency applications. IGBTs have been reported to fail under excessive electrical and thermal stresses in variable speed drives and are considered as reliability problems in wind turbines, inverters in hybrid electric vehicles and railway traction motors. There is a need to develop methods to detect anomalous behavior and predict the remaining useful life (RUL) of IGBTs to prevent system downtime and costly failures.

In this study, a framework for prognostics of IGBTs was developed to provide early warnings of failure and predict the remaining useful life. The prognostic framework was implemented on non punch through (NPT) IGBTs. Power cycling of IGBTs was performed and the gate-emitter voltage, collector-emitter voltage, collector-emitter current and case temperature was monitored in-situ during aging. The on-state collector-emitter current ($I_{CE(ON)}$) and collector-emitter voltage ($V_{CE(ON)}$) were identified as precursors to IGBT failure. Electrical characterization and X-ray

analysis was performed before and after aging to map degradation in the devices to observed trends in the precursor parameters.

A Mahalanobis distance based approach was used for anomaly detection. The initial $I_{CE(ON)}$ and $V_{CE(ON)}$ parameters were used to compute the healthy MD distance. This healthy MD distance was transformed and the mean and standard deviation of the transformed MD data was obtained. The $\mu+3\sigma$ upper bound obtained from the transformed healthy MD was then used as a threshold for anomaly detection. This approach was able to detect anomalous behavior in IGBTs before failure.

Upon anomaly detection, a particle filter approach was used for predicting the remaining useful life of the IGBTs. A system model was developed using the degradation trend of the $V_{CE(ON)}$ parameter. This model was obtained by a least squares regression of the IGBT degradation curve. The tracking and prediction performance of the model with the particle filter was demonstrated.

PROGNOSTICS OF INSULATED GATE BIPOLAR TRANSISTORS

By

Nishad Patil

Dissertation submitted to the Faculty of the Graduate School of the
University of Maryland, College Park, in partial fulfillment
of the requirements for the degree of
Doctor of Philosophy
2011

Advisory Committee:
Professor Michael G. Pecht, Chair
Professor Martin Peckerar
Professor Donald Barker
Professor Peter Sandborn
Associate Professor Patrick McCluskey
Dr. Diganta Das

© Copyright by
Nishad Patil
2011

Acknowledgements

I thank my advisor, Prof. Michael Pecht, for his guidance and support during the course of my graduate studies. I thank Prof. Peckerar, Prof. Barker, Prof. Sandborn, Prof. McCluskey and Dr. Das for serving on my dissertation committee and providing me valuable advice.

I thank the current and former students, faculty and staff of CALCE for the discussions and help provided in my research. I thank Dr. Kai Goebel for giving me an opportunity to work on power semiconductor prognostics. I thank Dr. Jose Celaya for the numerous discussions we have had and the assistance he has provided in completing my dissertation research. I thank Dr. Bhaskar Saha for the several discussions on particle filters.

I thank my family and friends for supporting me through the duration of my graduate studies.

Table of Contents

Acknowledgements ii
Table of Contents iii
List of Tables v
List of Figures vi
Chapter 1. Introduction 1
  Insulated Gate Bipolar Transistor (IGBT) 2
  Prognostic Approaches 6
  IGBT Prognostics 9
  Motivation 14
  Dissertation Scope and Outline 15
Chapter 2. Power Semiconductor Aging System 17
  Hardware 18
  Software 22
Chapter 3. Aging Tests and Degradation Analysis 27
  Aging Procedure 28
  Test Condition 1 29
  Data Analysis for Test Condition 1 32
  Electrical Characterization for Test Condition 1 33
  X-ray Analysis for Test Condition 1 35
  Test Condition 2 36
  Data Analysis for Test Condition 2 37
  X-ray Analysis for Test Condition 2 39
  Failure Mechanisms and Acceleration Factor 39
  Measurement of Junction Temperature 42
  Summary 44
Chapter 4. Anomaly Detection 46
  Mahalanobis Distance 47
  Anomaly Detection Approach 47
  Anomaly Detection for Test Condition 1 51
  Anomaly Detection for Test Condition 2 55
  Comparison of the MD Approach with a Fixed $V_{CE(ON)}$ Threshold for Anomaly Detection 59
  Summary 61
Chapter 5. Prognostics 62
  Particle Filter: General Description 62
  RUL Estimation for IGBTs 66
  Computational Complexity 70
  Effect of Number of Particles on Failure Prediction 71
  Predictions for N=10, 30,100 and 300 at 3 minutes 72
  Predictions for N=10, 30,100 and 300 at 6 minutes 73
  Predictions for N=10, 30,100 and 300 at 12 minutes 75
  Predictions for N=10, 30,100 and 300 at 18 minutes 77

Effect of Increased Number of Parts in Development of System Model 81
Effect of Number of Particles on the Confidence of the Failure Prediction Distribution 83
Implementation of the Particle Filter using $I_{CE(ON)}$ 85
Summary 85
Chapter 6. Contributions and Future Work 88
Future Work 88
Appendix A 90
Appendix B 97
Appendix C 104
Predictions for “N4” IGBT after 3, 6, 12 and 18 minutes 104
Prediction for10 particles 104
Prediction for 30 particles 106
Prediction for 100 particles 107
Prediction for 300 particles 109
Predictions for “N5” IGBT after 3, 6, 12 and 18 minutes 111
Prediction for 10 particles 111
Prediction for 30 particles 112
Prediction for 100 particles 114
Prediction for 300 particles 115
Predictions for “N6” IGBT after 3, 6, 12 and 18 minutes 117
Prediction for 10 particles 117
Prediction for 30 particles 119
Prediction for 100 particles 121
Prediction for 300 particles 123
Predictions for “N7” IGBT after 3, 6, 12 and 18 minutes 125
Prediction for 10 particles 125
Prediction for 30 particles 127
Prediction for 100 particles 128
Prediction for 300 particles 130
Predictions for “N8” IGBT after 3, 6, 12 and 18 minutes 132
Prediction for 10 particles 132
Prediction for 30 particles 133
Prediction for 100 particles 135
Prediction for 300 particles 136
Predictions for “N9” IGBT after 3, 6, 12 and 18 minutes 138
Prediction for 10 particles 138
Prediction for 30 particles 139
Prediction for 100 particles 141
Prediction for 300 particles 143
Predictions for “N10” IGBT after 3, 6, 12 and 18 minutes 144
Prediction for 10 particles 144
Prediction for 30 particles 146
Prediction for 100 particles 147
Prediction for 300 particles 149
Bibliography 151

List of Tables

Table 3-1: Failure time and failure mode for NPT IGBTs under test condition 1...... 30
Table 3-2: Failure time and failure mode for test condition 2 36
Table 4-1: Anomaly detection times obtained for test condition 1............................. 55
Table 4-2: Anomaly detection times obtained for test condition 2............................. 58
Table 4-3: Detection time comparison for test condition 1 60
Table 4-4: Detection time comparison for test condition 2 60
Table 5-1: RUL prediction for IGBTs in test condition 1 69
Table 5-2: RUL prediction for IGBTs in test condition 2 70
Table 5-3: Effect of particle size on failure prediction time for IGBT N3 (Actual Failure=21.4 minutes)... 79
Table 5-4: System model parameters... 81
Table 5-5: Mean time to failure prediction using particle filters for the four system models 82

List of Figures

Figure 1-1: Schematic of n-channel IGBT operation 3
Figure 1-2: Overview of IGBT technologies 5
Figure 1-3: $V_{CE(sat)}$ variation observed with power cycling in IGBT module [20] 9
Figure 1-4: Changes in the ringing characteristic of the new (i.e., T1) and aged (T2, T3, and T4) IGBTs [21] 11
Figure 1-5: Boundary to identify defective IGBTs from healthy IGBTs [23]............ 12
Figure 1-6: Particle filter framework [24] 14
Figure 1-7: RUL prediction for PT IGBT [24] 14
Figure 2-1: IGBT under a resistive load 18
Figure 2-2: IGBT Aging System 19
Figure 2-3. Gate Driver Board 20
Figure 2-4: Main board 21
Figure 2-5: Assembled test board 22
Figure 2-6: Schematic of the aging process 23
Figure 2-7: Example of waveforms acquired by the oscilloscope 25
Figure 2-8. MATLAB structure array 26
Figure 3-1: Aging Schematic 29
Figure 3-2: Latch-up of NPT IGBT "N3" aged under test condition 1 31
Figure 3-3: Collector-emitter current response to input gate pulse 31
Figure 3-4: Collector-emitter voltage response to input gate pulse 32
Figure 3-5: $I_{CE(ON)}$ and $V_{CE(ON)}$ vs. aging time for NPT IGBT "N3" aged by test condition 1 33
Figure 3-6: I-V characteristics (room temperature) for IGBT N3 aged by test condition 1 34
Figure 3-7: I-V characteristics (room temperature) for IGBT N2 aged by test condition 1 35
Figure 3-8: Before (left) and after (right) X-ray images of NPT IGBT aged by test condition 1 35
Figure 3-9: Latch-up of NPT IGBT "NPT2" aged by test condition 2 37
Figure 3-10: NPT IGBT "NPT3" aged by test condition 2 failed to turn-on 37
Figure 3-11: $I_{CE(ON)}$ and $V_{CE(ON)}$ vs. aging time for NPT IGBT "NPT3" 38
Figure 3-12: I-V characteristics (room temperature) for IGBT NPT2 aged by test condition 2 39
Figure 3-13: Before (left) and after (right) X-ray images of NPT IGBT aged by test condition 2 39
Figure 3-14: Calibration curve (T_j versus V_{CE} at I_{CE} = 100mA) [26] 43
Figure 3-15: V_{CE} measurement during aging process at I_{CE} = 100mA [26] 44
Figure 4-1: Histogram of the healthy MD values for IGBT "N3" 52
Figure 4-2: Normal probability plot of the healthy MD data for IGBT N3 52
Figure 4-3: Transformed healthy MD data for IGBT N3 53
Figure 4-4: Normal probability plot of the transformed healthy MD data for IGBT N3 53
Figure 4-5: Transformed MD data vs.ing time for IGBT "N3" 54

Figure 4-6: Histogram of the healthy MD values for IGBT “NPT3” 56
Figure 4-7: Normal probability plot of the healthy MD data for IGBT NPT3 56
Figure 4-8: Transformed healthy MD data for IGBT NPT3.. 57
Figure 4-9: Normal probability plot of the transformed healthy MD data for IGBT NPT3 57
Figure 4-10: Transformed MD data vs. aging time for IGBT “NPT3” 58
Figure 4-11: Comparison of transformed MD and fixed 5% $V_{CE(ON)}$ threshold for IGBT “N3” 59
Figure 5-1: State estimation and RUL prediction of IGBT “N3” 68
Figure 5-2: State estimation and RUL prediction of IGBT “NPT3” 69
Figure 5-3: Computational complexity of the particle filter as a function of the number of particles 71
Figure 5-4: Prediction for N= 10 particles and time t= 3minutes 72
Figure 5-5: Prediction for N= 30 particles and time t= 3 minutes 72
Figure 5-6: Prediction for N= 100 particles and time t= 3 minutes 73
Figure 5-7: Prediction for N= 300 particles and time t= 3 minutes 73
Figure 5-8: Prediction for N= 10 particles and time t= 6 minutes 74
Figure 5-9: Prediction for N= 30 particles and time t= 6 minutes 74
Figure 5-10: Prediction for N= 100 particles and time t= 6 minutes 74
Figure 5-11: Prediction for N= 300 particles and time t= 6 minutes 75
Figure 5-12: Prediction for N= 10 particles and time t= 12 minutes 75
Figure 5-13: Prediction for N= 30 particles and time t= 12 minutes 76
Figure 5-14: Prediction for N= 100 particles and time t= 12 minutes 76
Figure 5-15: Prediction for N= 300 particles and time t= 12 minutes 76
Figure 5-16: Prediction for N= 10 particles and time t= 18 minutes 77
Figure 5-17: Prediction for N= 30 particles and time t= 18 minutes 77
Figure 5-18: Prediction for N= 100 particles and time t= 18 minutes 78
Figure 5-19: Prediction for N= 300 particles and time t= 18 minutes 78
Figure 5-20: Failure prediction for part N6 using three part system model 82
Figure 5-21: Failure prediction for part N6 using four part system model................... 82
Figure 5-22: Failure prediction for part N6 using five part system model 83
Figure 5-23: Particle filter prediction using $I_{CE(ON)}$ for part "N3" 85
Figure 6-1: $I_{CE(ON)}$ and $V_{CE(ON)}$ vs. aging time for “N1” aged by test condition 1......... 90
Figure 6-2: $I_{CE(ON)}$ and $V_{CE(ON)}$ vs. aging time for “N2” aged by test condition 1......... 90
Figure 6-3: $I_{CE(ON)}$ and $V_{CE(ON)}$ vs. aging time for “N4” aged by test condition 1......... 91
Figure 6-4: $I_{CE(ON)}$ and $V_{CE(ON)}$ vs. aging time for “N5” aged by test condition 1......... 91
Figure 6-5: $I_{CE(ON)}$ and $V_{CE(ON)}$ vs. aging time for “N6” aged by test condition 1......... 92
Figure 6-6: $I_{CE(ON)}$ and $V_{CE(ON)}$ vs. aging time for “N7” aged by test condition 1......... 92
Figure 6-7: $I_{CE(ON)}$ and $V_{CE(ON)}$ vs. aging time for “N8” aged by test condition 1......... 93
Figure 6-8: $I_{CE(ON)}$ and $V_{CE(ON)}$ vs. aging time for “N9” aged by test condition 1......... 93
Figure 6-9: $I_{CE(ON)}$ and $V_{CE(ON)}$ vs. aging time for “N10” aged by test condition 1....... 94
Figure 6-10: $I_{CE(ON)}$ and $V_{CE(ON)}$ vs. aging time for “NPT1” aged by test condition 2 .. 94
Figure 6-11: $I_{CE(ON)}$ and $V_{CE(ON)}$ vs. aging time for “NPT2” aged by test condition 2 .. 95
Figure 6-12: $I_{CE(ON)}$ and $V_{CE(ON)}$ vs. aging time for “NPT4” aged by test condition 2 .. 95
Figure 6-13: $I_{CE(ON)}$ and $V_{CE(ON)}$ vs. aging time for “NPT5” aged by test condition 2 .. 96
Figure 6-14: Transformed MD data vs. aging time for IGBT “N1”............................. 97

Figure 6-15: Transformed MD data vs. aging time for IGBT “N2” 97
Figure 6-16: Transformed MD data vs. aging time for IGBT “N4” 98
Figure 6-17: Transformed MD data vs. aging time for IGBT “N5” 98
Figure 6-18: Transformed MD data vs. aging time for IGBT “N6” 99
Figure 6-19: Transformed MD data vs. aging time for IGBT “N7” 99
Figure 6-20: Transformed MD data vs. aging time for IGBT “N8” 100
Figure 6-21: Transformed MD data vs. aging time for IGBT “N9” 100
Figure 6-22: Transformed MD data vs. aging time for IGBT “N10” 101
Figure 6-23: Transformed MD data vs. aging time for IGBT “NPT1” 101
Figure 6-24: Transformed MD data vs. aging time for IGBT “NPT2” 102
Figure 6-25: Transformed MD data vs. aging time for IGBT “NPT4” 102
Figure 6-26: Transformed MD data vs. aging time for IGBT “NPT5” 103
Figure 6-27: Prediction for N= 10 particles and time t= 3 minutes 104
Figure 6-28: Prediction for N= 10 particles and time t= 6 minutes 104
Figure 6-29: Prediction for N= 10 particles and time t= 12 minutes 105
Figure 6-30: Prediction for N= 10 particles and time t= 18 minutes 105
Figure 6-31: Prediction for N= 30 particles and time t= 3 minutes 106
Figure 6-32: Prediction for N= 30 particles and time t= 6 minutes 106
Figure 6-33: Prediction for N= 30 particles and time t= 12 minutes 106
Figure 6-34: Prediction for N= 30 particles and time t= 18 minutes 107
Figure 6-35: Prediction for N= 100 particles and time t= 3 minutes 107
Figure 6-36: Prediction for N= 100 particles and time t= 6 minutes 108
Figure 6-37: Prediction for N= 100 particles and time t= 12 minutes 108
Figure 6-38: Prediction for N= 100 particles and time t= 18 minutes 109
Figure 6-39: Prediction for N= 300 particles and time t= 3 minutes 109
Figure 6-40: Prediction for N= 300 particles and time t= 6 minutes 109
Figure 6-41: Prediction for N= 300 particles and time t= 12 minutes 110
Figure 6-42: Prediction for N= 300 particles and time t= 18 minutes 110
Figure 6-43: Prediction for N= 10 particles and time t= 3 minutes 111
Figure 6-44: Prediction for N= 10 particles and time t= 6 minutes 111
Figure 6-45: Prediction for N= 10 particles and time t= 12 minutes 111
Figure 6-46: Prediction for N= 10 particles and time t= 18 minutes 112
Figure 6-47: Prediction for N= 30 particles and time t= 3 minutes 112
Figure 6-48: Prediction for N= 30 particles and time t= 6 minutes 112
Figure 6-49: Prediction for N= 30 particles and time t= 12 minutes 113
Figure 6-50: Prediction for N= 30 particles and time t= 18 minutes 113
Figure 6-51: Prediction for N= 100 particles and time t= 3 minutes 114
Figure 6-52: Prediction for N= 100 particles and time t= 6 minutes 114
Figure 6-53: Prediction for N= 100 particles and time t= 12 minutes 115
Figure 6-54: Prediction for N= 100 particles and time t= 18 minutes 115
Figure 6-55: Prediction for N= 300 particles and time t= 3 minutes 115
Figure 6-56: Prediction for N= 300 particles and time t= 6 minutes 116
Figure 6-57: Prediction for N= 300 particles and time t= 12 minutes 116
Figure 6-58: Prediction for N= 300 particles and time t= 18 minutes 117
Figure 6-59: Prediction for N= 10 particles and time t= 3 minutes 117
Figure 6-60: Prediction for N= 10 particles and time t= 6 minutes 118

Figure 6-61: Prediction for N= 10 particles and time t= 12 minutes 118
Figure 6-62: Prediction for N= 10 particles and time t= 18 minutes 119
Figure 6-63: Prediction for N= 30 particles and time t= 3 minutes 119
Figure 6-64: Prediction for N= 30 particles and time t= 6 minutes 120
Figure 6-65: Prediction for N= 30 particles and time t= 12 minutes 120
Figure 6-66: Prediction for N= 30 particles and time t= 18 minutes 121
Figure 6-67: Prediction for N= 100 particles and time t= 3 minutes 121
Figure 6-68: Prediction for N= 100 particles and time t= 6 minutes 121
Figure 6-69: Prediction for N= 100 particles and time t= 12 minutes 122
Figure 6-70: Prediction for N= 100 particles and time t= 18 minutes 123
Figure 6-71: Prediction for N= 300 particles and time t= 3 minutes 123
Figure 6-72: Prediction for N= 300 particles and time t= 6 minutes 123
Figure 6-73: Prediction for N= 300 particles and time t= 12 minutes 124
Figure 6-74: Prediction for N= 300 particles and time t= 18 minutes 124
Figure 6-75: Prediction for N= 10 particles and time t= 3 minutes 125
Figure 6-76: Prediction for N= 10 particles and time t= 6 minutes 125
Figure 6-77: Prediction for N= 10 particles and time t= 12 minutes 126
Figure 6-78: Prediction for N= 10 particles and time t= 18 minutes 126
Figure 6-79: Prediction for N= 30 particles and time t= 3 minutes 127
Figure 6-80: Prediction for N= 30 particles and time t= 6 minutes 127
Figure 6-81: Prediction for N= 30 particles and time t= 12 minutes 127
Figure 6-82: Prediction for N= 30 particles and time t= 18 minutes 128
Figure 6-83: Prediction for N= 100 particles and time t= 3 minutes 128
Figure 6-84: Prediction for N= 100 particles and time t= 6 minutes 129
Figure 6-85: Prediction for N= 100 particles and time t= 12 minutes 129
Figure 6-86: Prediction for N= 100 particles and time t= 18 minutes 130
Figure 6-87: Prediction for N= 300 particles and time t= 3 minutes 130
Figure 6-88: Prediction for N= 300 particles and time t= 6 minutes 131
Figure 6-89: Prediction for N= 300 particles and time t= 12 minutes 131
Figure 6-90: Prediction for N= 300 particles and time t= 18 minutes 131
Figure 6-91: Prediction for N= 10 particles and time t= 3 minutes 132
Figure 6-92: Prediction for N= 10 particles and time t= 6 minutes 132
Figure 6-93: Prediction for N= 10 particles and time t= 12 minutes 133
Figure 6-94: Prediction for N= 10 particles and time t= 18 minutes 133
Figure 6-95: Prediction for N= 30 particles and time t= 3 minutes 133
Figure 6-96: Prediction for N= 30 particles and time t= 6 minutes 134
Figure 6-97: Prediction for N= 30 particles and time t= 12 minutes 134
Figure 6-98: Prediction for N= 30 particles and time t= 18 minutes 135
Figure 6-99: Prediction for N= 100 particles and time t= 3 minutes 135
Figure 6-100: Prediction for N= 100 particles and time t= 6 minutes 135
Figure 6-101: Prediction for N= 100 particles and time t= 12 minutes 136
Figure 6-102: Prediction for N= 100 particles and time t= 18 minutes 136
Figure 6-103: Prediction for N= 300 particles and time t= 3 minutes 136
Figure 6-104: Prediction for N= 300 particles and time t= 6 minutes 137
Figure 6-105: Prediction for N= 300 particles and time t= 12 minutes 137
Figure 6-106: Prediction for N= 300 particles and time t= 18 minutes 137

Figure 6-107: Prediction for N= 10 particles and time t= 3 minutes 138
Figure 6-108: Prediction for N= 10 particles and time t= 6 minutes 138
Figure 6-109: Prediction for N= 10 particles and time t= 12 minutes 139
Figure 6-110: Prediction for N= 10 particles and time t= 18 minutes 139
Figure 6-111: Prediction for N= 30 particles and time t= 3 minutes 139
Figure 6-112: Prediction for N= 30 particles and time t= 6 minutes 140
Figure 6-113: Prediction for N= 30 particles and time t= 12 minutes 140
Figure 6-114: Prediction for N= 30 particles and time t= 18 minutes 140
Figure 6-115: Prediction for N= 100 particles and time t= 3 minutes 141
Figure 6-116: Prediction for N= 100 particles and time t= 6 minutes 141
Figure 6-117: Prediction for N= 100 particles and time t= 12 minutes 142
Figure 6-118: Prediction for N= 100 particles and time t= 18 minutes 142
Figure 6-119: Prediction for N= 300 particles and time t= 3 minutes 143
Figure 6-120: Prediction for N= 300 particles and time t= 6 minutes 143
Figure 6-121: Prediction for N= 300 particles and time t= 12 minutes 143
Figure 6-122: Prediction for N= 300 particles and time t= 18 minutes 144
Figure 6-123: Prediction for N= 10 particles and time t= 3 minutes 144
Figure 6-124: Prediction for N= 10 particles and time t= 6 minutes 145
Figure 6-125: Prediction for N= 10 particles and time t= 12 minutes 145
Figure 6-126: Prediction for N= 10 particles and time t= 18 minutes 145
Figure 6-127: Prediction for N= 30 particles and time t= 3 minutes 146
Figure 6-128: Prediction for N= 30 particles and time t= 6 minutes 146
Figure 6-129: Prediction for N= 30 particles and time t= 12 minutes 147
Figure 6-130: Prediction for N= 30 particles and time t= 18 minutes 147
Figure 6-131: Prediction for N= 100 particles and time t= 3 minutes 147
Figure 6-132: Prediction for N= 100 particles and time t= 6 minutes 148
Figure 6-133: Prediction for N= 100 particles and time t= 12 minutes 148
Figure 6-134: Prediction for N= 100 particles and time t= 18 minutes 148
Figure 6-135: Prediction for N= 300 particles and time t= 3 minutes 149
Figure 6-136: Prediction for N= 300 particles and time t= 6 minutes 149
Figure 6-137: Prediction for N= 300 particles and time t= 12 minutes 150
Figure 6-138: Prediction for N= 300 particles and time t= 18 minutes 150

.

Chapter 1. Introduction

Insulated gate bipolar transistors (IGBTs) are the power semiconductor switch of choice for sources that operate at voltages above 200V [1]. Due to their low on-state losses and simple gate drive requirements, IGBTs are extensively used in medium and high power motor drives and power supplies. IGBTs have been reported to fail under excessive electrical and thermal stresses in variable speed drives [2], and are considered as reliability problems in wind turbines [3], inverters in hybrid electric vehicles [4] and railway traction motors [5]. There is a need to develop methods to detect anomalous behavior and predict the remaining useful life (RUL) of IGBTs to prevent system downtime and costly failures.

Prognostics is the process of predicting the future health of a product by assessing the extent of deviation or degradation from its expected normal operating conditions [6], and by extrapolating the behavior to failure thresholds using appropriate models and algorithms. These models and algorithms may need to incorporate not only features derived from monitored precursor signals, but also current and future environmental conditions and operational loads.

In this study, a framework for IGBT prognostics is proposed and implemented. The implementation of prognostics for IGBTs has potential benefits in terms of avoidance of unscheduled maintenance and improved safety.

Insulated Gate Bipolar Transistor (IGBT)

The insulated-gate bipolar transistor (IGBT) is a three-terminal power semiconductor device. This device is also called the insulated gate rectifier (IGR), conductivity-modulated field effect transistor (COMFET), gain-enhanced metal oxide semiconductor field effect transistor (GEMFET), bipolar field effect transistor (BiFET), and injector field effect transistor [7].

The IGBT was first experimentally demonstrated by Baliga in 1979 [8]. Plummer and Scharf in 1980 also experimentally demonstrated the IGBT and provided a quantitative analysis and models for the device [9] [10]. Becke and Wheatley filed what is considered the seminal patent on IGBTs in 1980 which was subsequently awarded in 1982 [11]. The first IGBT devices were commercially available from General Electric in 1983. Currently, IGBTs are widely used in medium frequency (20-200 KHz) and medium power (10KW-1MW) applications such as switch mode power supplies (SMPS), AC motor drives, uninterrupted power supply (UPS) and inductive heating. High voltage and high current IGBTs (6500V, 200-400A) are used in electric traction applications for locomotives and streetcars [12]. Companies that manufacture IGBTs include Toshiba, Infineon, Microsemi, ON semiconductor, International Rectifier, IXYS, Hitachi, Fuji Electric, Fairchild Semiconductor, Powerex and Siemens.

The IGBT is a functional integration of metal oxide semiconductor (MOS) and bipolar device technologies in monolithic form. IGBTs have switching characteristics similar to a metal oxide semiconductor field effect transistor

(MOSFET) and the high current and voltage capabilities of a bipolar junction transistor (BJT).

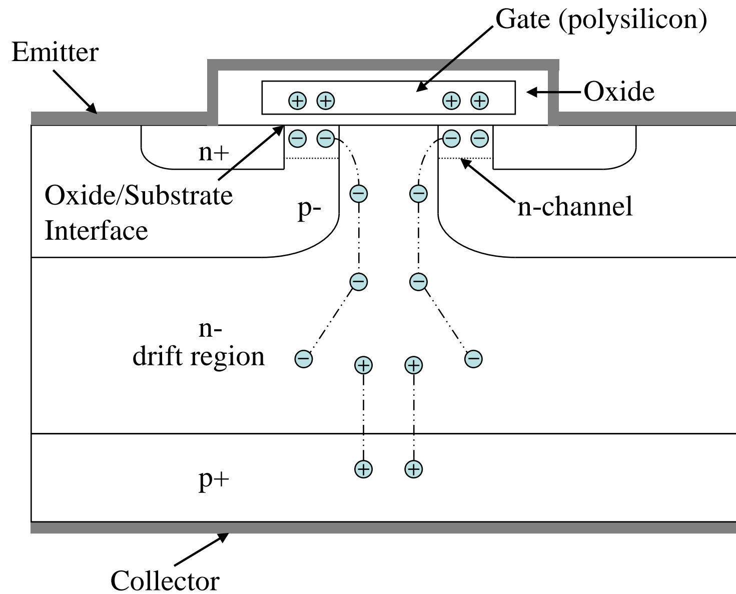

Figure 1-1: Schematic of n-channel IGBT operation

The structure of an IGBT is similar to that of a vertical diffusion power MOSFET, except for an additional p+ layer above the collector as seen in Figure 1-1. The main characteristic of the vertical configuration is that the collector (drain) forms the bottom of the device while the emitter (source) region remains the same as a traditional MOSFET. Figure 1-1 represents the schematic structure of the n-channel IGBT. The additional p+ layer in the IGBT acts as a source of holes that are injected into the drift region during operation. These injected holes enable quick turn-off by recombination with excess electrons that remain in the body of the IGBT after switch-off.

The current flow in this device is composed of both holes and electrons. Applying a positive voltage to the gate switches on the device when a conductive

channel also known as the inversion layer, is created. Electrons flow from the emitter through the conductive channel to the collector terminal. A positive voltage applied to the collector with the emitter at ground causes the injection of positive carriers from the p+ layer into the drift region which allows for conductivity modulation of the device, leading to a lower on-resistance compared to the power MOSFET [12]. Since an IGBT is switched on by voltage rather than current, it results in faster switching speeds in comparison to BJT. As the conductivity of the device is modulated by charge injection from the p+ layer, it allows for lower on-state resistance than the power MOSFET. A modification of this structure involves the addition of an additional n+ layer, called the buffer layer, above the p+ layer that contacts the collector terminal. The additional n+ layer leads to faster evacuation of stored charges resulting in increased switching speed of the IGBT.

IGBTs are classified based on the orientation of the gate as planar or trench. In planar structures, the gate is parallel to the collector. In trench IGBTs, the gate is vertical to the collector terminal. In the planar IGBT, electrons flow through a horizontal channel and then downwards to the collector. This current path leads to higher losses during conduction. The trench IGBT on the other hand, has a single direction for current flow, from the emitter, through the vertical channel down to the collector. This path lowers the conduction loss of the trench IGBT, and minimizes the use of silicon, allowing for reduced size of the trench IGBT for a given voltage rating in comparison to the planar IGBT.

IGBTs are further classified as punch-through (PT), non punch-through (NPT) and field stop (FS) as shown in Figure 1-2. The punch-through IGBT is manufactured

using an expensive epitaxial process. The electric field punches through and terminates in the p+ layer (buffer layer). The non punch-through IGBT is manufactured using a less expensive float zone silicon process. In this device, the electric field terminates in the drift region. For a given voltage rating, the size of the NPT IGBT is smaller than a PT IGBT. The field stop IGBT is manufactured using the inexpensive float zone process and has a buffer layer that is used to terminate the electric field. It has the smallest size for a given voltage rating among the three technologies.

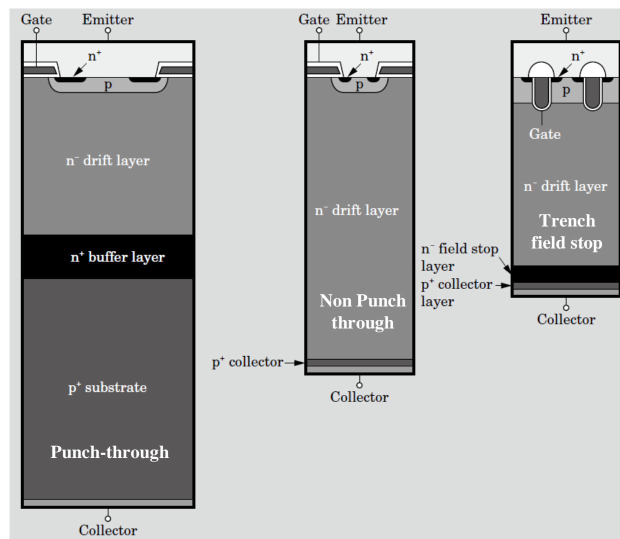

Figure 1-2: Overview of IGBT technologies

The conduction loss is a function of the on-state collector emitter voltage $V_{CE(ON)}$. The $V_{CE(ON)}$ is a function of the n- drift region thickness. From Figure 1-2, we see that the punch-through and field stop IGBTs have thinner drift regions in comparison to the non punch-though IGBT. Therefore, the punch-through and the field stop IGBTs have lower conduction loss in comparison to NPT. However, the

NPT IGBT can sustain large currents such as in short circuit events due to the thicker n- drift region.

The switch-off losses in IGBTs are based on the time required for the holes in the drift region to recombine with electrons and be swept out of the device through the collector. The punch-through IGBT uses heavy hole injection to reduce conductivity losses. These excessive holes lead to high switching losses for punch-through IGBTs in comparison to the NPT and field stop transistors.

Trench IGBTs, due to their vertical gate structure, have lower $V_{CE(on)}$. Hence, trench IGBTs have lower conduction losses in comparison to planar IGBTs. A modification of the trench IGBT to include a field stop buffer layer leads to a reduction in switching losses as well. The trench IGBT configuration in comparison with the planar structures is shown in Figure 1-2.

Prognostic Approaches

Prognostic approaches can be classified as model-based or data driven. The model-based approaches can be further classified into system model and physics of failure approaches [13]. The system model based approach to prognostics uses mathematical representations to incorporate a physical understanding of the system in order to implement diagnostics and prognostics [14]. Statistical estimation techniques based on residuals and parity relations are then used to detect, isolate and predict degradation. The physics of failure approach (PoF) to prognostics utilizes knowledge of a product's life cycle loading conditions, geometry, and material properties to identify potential failure mechanisms and estimate its remaining useful life [6].

Data-driven approaches involve learning statistical relationships and patterns from sensor data to provide valuable decision-making information. They are based on the assumption that the statistical characteristics of the system data remain relatively unchanged until a fault occurs in the system. In this approach, in-situ monitoring of environmental and operational loads and system parameters is performed. The data is then analyzed using a variety of techniques for anomaly detection followed by prediction of RUL. Anomaly detection techniques are used for diagnostics in order to detect changes in the system that may lead to system malfunction or failure. For prognostic purposes, trends in parameter values, features or changes in probabilities of the system state are then used to estimate the time to failure of the system using prediction algorithms.

There are several approaches that have been developed for electronic prognostics. A few examples of these prognostic approaches will be described. The current state of research on prognostics of IGBTs will be discussed in detail. The issues unaddressed in previous IGBT prognostics studies will form the basis for the motivation of the current study.

Gu et al. [15] demonstrated the Physics of Failure approach to prognostics of electronics under vibration loading by monitoring interconnect strain and assessing damage accumulation. Strain gauges were used to monitor the bending curvature of printed wiring boards as a response to loading in the form of vibration. The interconnect strain values were used in a vibration failure fatigue model for damage assessment. The Miner's rule was used to estimate the accumulated damage which was then used to estimate the RUL of the boards.

Saha et al. [16] used a system model approach to estimated the remaining useful life of lithium ion batteries. The battery was represented by a lumped parameter model. The parameters of the model were calculated using relevance vector machine (RVM) regression on experimental data. An extended Kalman filter and particle filter algorithms were used to determine the battery RUL.

Goodman et al. [17] described the use of prognostic cells to predict failure in integrated circuits. The prognostic cell is designed to fail prior to the circuit on the same chip for all realistic operating conditions. Prognostic monitors in the test cell see the exact environment that the actual circuit sees, but at an accelerated rate, thereby providing failure prediction. These cells were developed for 0.35, 0.25, and 0.18 micron complementary metal oxide semiconductor (CMOS) processes to predict failure as a result of time dependent dielectric breakdown (TDDB), hot carrier injection (HCI), and negative bias temperature instability (NBTI).

Vichare et al. described four main approaches to electronic prognostics which included: built-in-test (BIT); use of expendable devices, such as "canaries" and fuses that fail earlier than the host product to provide advance warning of failure; monitoring and reasoning of parameters that are precursors to impending failure, such as shifts in performance parameters; and modeling of stress and damage in electronic parts and structures utilizing exposure conditions (e.g., usage, temperature, vibration, radiation) to compute accumulated damage [18].

Kumar et al. [19] used the data-driven approach to detect anomalies of notebook computers by monitoring performance parameters and comparing them against the historical data using Mahalanobis distance.

IGBT Prognostics

Xiong et al. [20] proposed an online diagnostic and prognostic system to predict the potential failure of an automotive IGBT power module. In this study, power cycling tests were performed on Toshiba 600V/800A IGBT modules for approximately 10000 hours. The stressing was performed by the application of repeated cycles of a 400 A current pulse (1 second), followed by a 20A current pulse (0.5 seconds) and a dwell period (8.5 seconds). During the test, collector-emitter voltage at saturation ($V_{CE(sat)}$) was monitored continuously. Unlike previous studies on power cycling of power modules, a sudden drop of the $V_{CE(sat)}$ followed by a rise was observed as shown in Figure 1-3. The authors suspected an initial solder joint degradation before wire-bond failure eventually caused the failure of the power module.

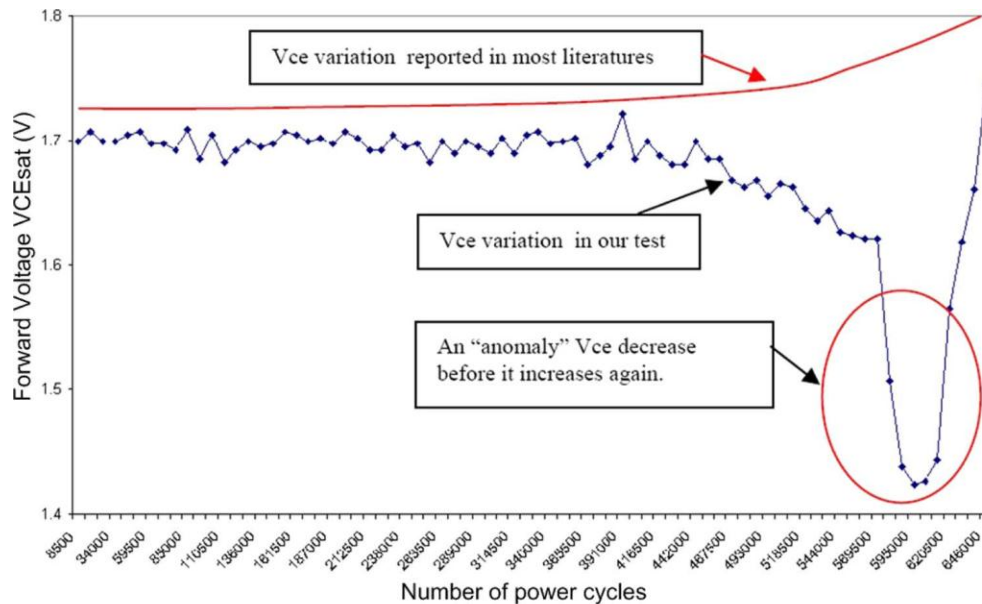

Figure 1-3: $V_{CE(sat)}$ variation observed with power cycling in IGBT module [20]

Based on the test results, the authors proposed a quasi real-time IGBT failure prognostic system. The prognostic approach of the authors consisted of a prognostic check-up routine that would be implemented at a preset frequency and current during vehicle turn-on and turn-off. During the check-up, $V_{CE(sat)}$ of the IGBT module would be compared with a look-up table of healthy data. Any variation of the $V_{CE(sat)}$ over 15% would signal an alarm. Although the authors reported this approach as a prognostic approach, the remaining useful life of IGBTs was not reported.

Ginart et al. [21] performed a study on IGBTs to develop an online ringing characterization technique to diagnose IGBT faults in power drives. The authors proposed the analysis of ringing characteristics of current and voltage transitions during switching as a feature for the evaluation of IGBT aging. In this study, IGBTs were aged by removing the heat sink from the transistor and switching it on and off until device latch-up occurred. The transistors were turned off for several minutes after latching. After the transistors recovered, they were aged again in a similar manner. The transistors latched after recovery but at a lower temperatures and shorter aging duration in comparison to previous aging. The transistors were evaluated using a custom ringing platform. It was observed that transistors that had latched multiple times had more damped voltage responses to an input gate pulse. The damped responses observed are shown in Figure 1-4.

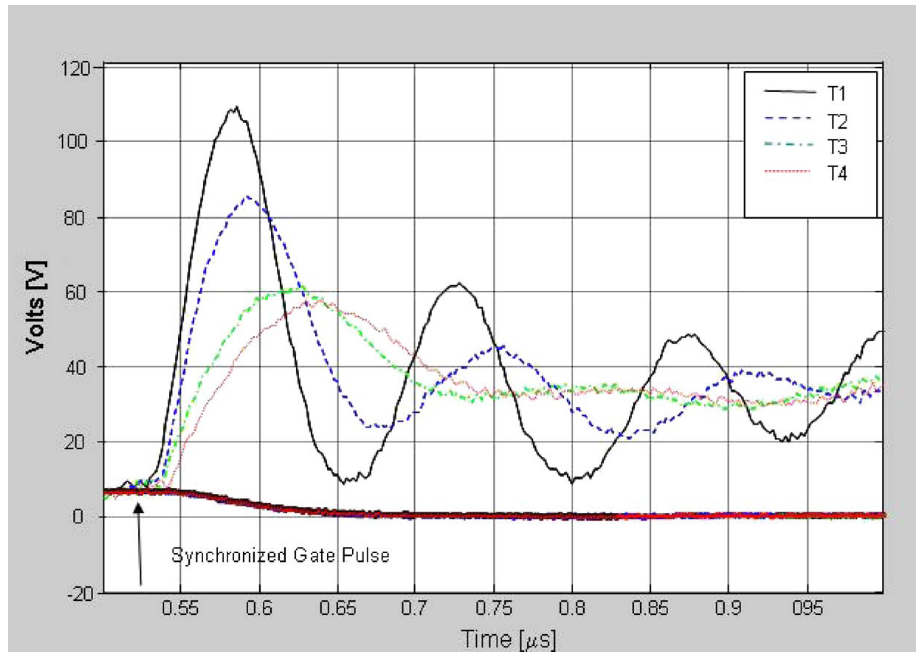

Figure 1-4: Changes in the ringing characteristic of the new (i.e., T1) and aged (T2, T3, and T4) IGBTs [21]

The authors speculated that the damped response was due to defects in the gate oxide which increased the channel resistance and hence the damping in the power drive system. Hot-carrier injection and time dependent dielectric breakdown were suggested as possible failure mechanisms in operation that could have resulted in the observed damped response.

Lu et al. [22] analyzed an IGBT power electronics module for railway applications. Based on a reliability analysis, the lifetime of the module was determined to be limited to the lifetime of the wirebond, bus bar, chip and substrate solder interconnects. The authors estimated the lifetime of the power module based on a strain based model for each of the solder interconnects. In this study, no comparison of the predicted lifetime was made with experimental results.

Oukaour et al. [23] developed an approach to determine defective IGBTs from healthy IGBTs. In this study, power cycling tests were performed on IGBT modules by subjecting them to cyclic DC collector-emitter current I_{CE} of 20A with 30 seconds power on and 20 seconds power off. Four parameters, the collector-to-emitter on-state voltage V_{CE}, the case temperature T_c, the junction temperature T_j and the junction-to-case thermal resistance $R_{th\text{-}jc}$ were monitored during the tests. Healthy IGBT state was established by applying small DC currents to the IGBT from 200mA to 16A by steps of 200 mA with 30 seconds power on and 1 second power off. The V_{CEsat} and T_j measurements were performed during this test. After determining the healthy IGBT state, the device was power cycled to failure. The V_{CEsat} and T_j were monitored during the aging tests. A neural network based classifier scheme was implemented to determine a boundary that can be used to identify defective IGBTs as shown in Figure 1-5.

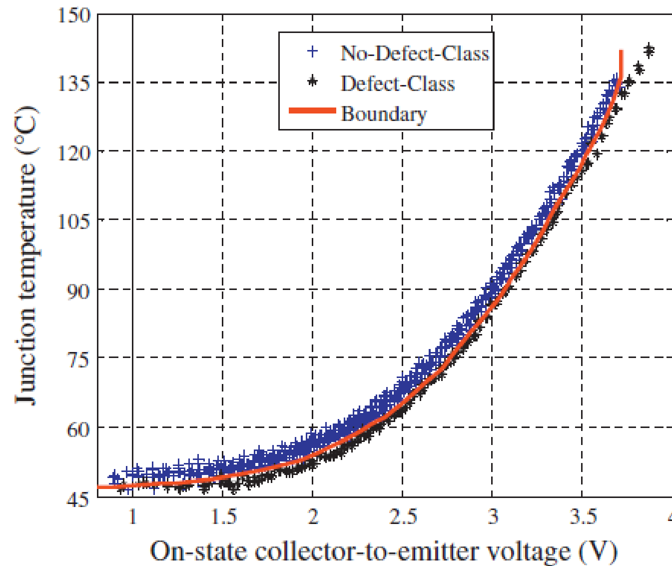

Figure 1-5: Boundary to identify defective IGBTs from healthy IGBTs [23]

Saha et al. [24] implemented the particle filter algorithm for the prediction of the remaining useful life of a punch through (PT) insulated gate bipolar transistor (IGBT). The algorithm was implemented on data obtained by performing high temperature power cycling aging test on a planar PT IGBT IRG4BC30KD manufactured by International Rectifier. The trend of the IGBT collector-emitter current (I_{CE}) at turn-off was fit with an exponential degradation model. A third degree polynomial was used for the regression fit as given by Equation (1.1).

$$I_{CE} = \exp(P_1 t^3 + P_2 t^2 + P_3 t + P_4) \qquad (1.1)$$

As the coefficients of the polynomial fit were highly correlated, only the trend of the first coefficient P1 with time was analyzed. This trend was then used in the particle filter framework for remaining useful life prediction. The particle filter framework proposed by Saha et al. is shown in Figure 1-6. The framework consists of extracting features from sensor data and using these features to estimate and track the system behavior. During the state estimation and tracking step, model parameters can also be learned from the feature data. The state estimation and tracking continues until a diagnostic trigger enables the state prediction and remaining useful life (RUL) estimation steps. In [24], the coefficient P1 was trended with time. For RUL prediction, the end of life threshold was set as a value of P1 crossing -2.5x10-5. A prediction of the RUL was performed at 51.875 minutes as shown in Figure 1-7.

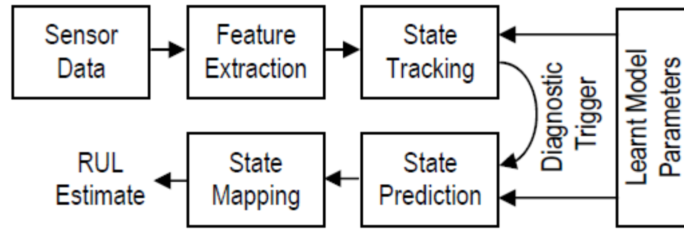

Figure 1-6: Particle filter framework [24]

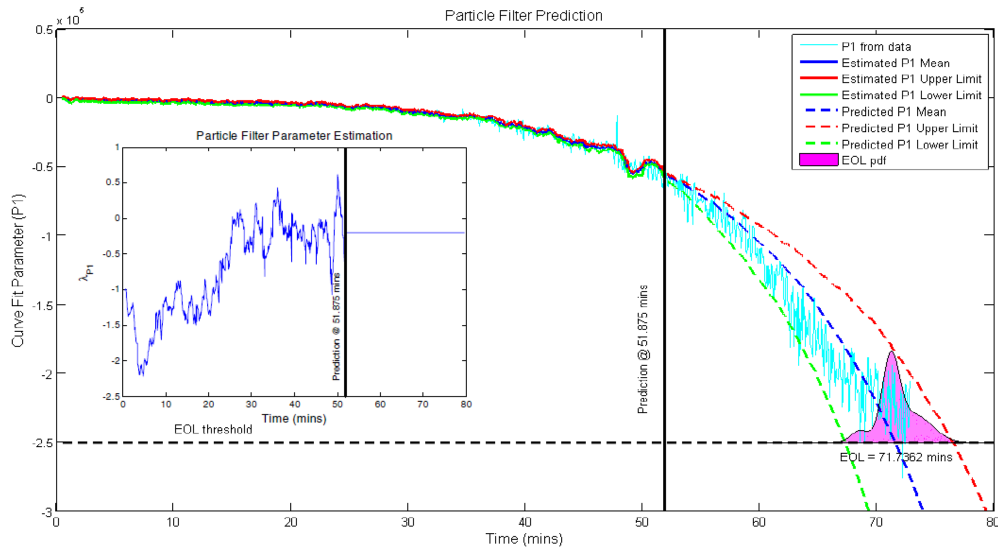

Figure 1-7: RUL prediction for PT IGBT [24]

Motivation

IGBT prognostics is a relatively new field with limited studies reported in literature. The majority of the studies are on development of diagnostic techniques to detect anomalies in applications such as automotive, motor drive and railway traction systems. Although remaining useful life estimates are reported by Saha et. al. for PT IGBTs, there are several concerns about the approach. First, a coefficient of the fit to the I_{CE} cannot be directly related to degradation in the device. For example, the fit does not take into account the effects of changes in operating temperature. Second, the failure threshold used was a lower limit on the fit parameter which was a fixed number. This failure threshold cannot be generalized to other IGBTs as the lower

limit of the fit parameter is going to change for every IGBT. Third, the diagnostic trigger was chosen arbitrarily. A diagnostic trigger is necessary to initiate the particle filter for RUL prediction. As the PF is a computationally intensive process, it needs to be used only when required. Hence, a diagnostic routine needs to be incorporated into the PF framework.

From this review, it is concluded that a comprehensive approach to the development of a prognostics framework for IGBTs is required. This will involve identifying the precursor parameters to IGBT failure, monitoring of these parameters during aging, mapping parameter shifts to physical degradation in the device, identifying and implementing algorithms for anomaly detection and prediction of remaining useful life of IGBTs.

Dissertation Scope and Outline

In this study, a prognostic framework for IGBTs is proposed and implemented. This framework involves the use of the Mahalanobis distance to detect anomalies in the IGBT and the particle filter algorithm for predicting RUL. Non punch through (NPT) IGBTs were aged by power cycling and several device and load parameters were monitored. Features from the monitored data were extracted to compute the Mahalanobis distance (MD). The MD was transformed and used with an appropriate threshold to detect anomalous behavior. Upon anomaly detection, the particle filter algorithm was implemented to predict the remaining useful life.

In chapter 2, the experimental set-up used in this study is described. This includes the details of the hardware and software developed to age the IGBTs. In chapter 3, the power cycling test conditions used to age the IGBTs are described. The

results of the data analysis of the monitored parameters are presented. Electrical characterization and X-ray analysis was performed before and after aging to determine the degradation in the IGBTs due to power cycling. The trends observed in the monitored parameters were mapped to degradation observed in the devices.

In chapter 4, the MD approach used for anomaly detection is described. The performance of the MD approach in providing advanced warning of failure is evaluated. In chapter 5, the particle filter algorithm is discussed. The remaining useful life estimates obtained by implementation of the algorithm are reported. In chapter 6, the contributions of this study are summarized and avenues for future research are discussed.

Chapter 2. Power Semiconductor Aging System

The main goal for the development of the power semiconductor aging system was to identify precursor parameters for device failure. Precursor parameters are parameters of the device that change with time wherein the change can be mapped to degradation in the device. Once the precursor parameters are identified, suitable diagnostic and prognostic algorithms can be implemented using these parameters to provide early warning of failure and predict remaining useful life.

Implementation of the aging system involved developing the hardware and software to perform power cycling of power semiconductor devices. The experimental test bed for this project was developed by Sonnenfeld et al. [25]. The aging system can operate gate controlled power transistors such as MOSFETs and IGBTs with current ratings ranging between 1 and 50A. The socket on the aging board accommodates three pin power transistors in a TO-220 package. The system design allows for flexibility in defining aging conditions such as gate (V_G) voltage, collector-emitter voltage (V_{CE}), switching frequency and case and package temperature hence providing the capability to simulate various operating conditions.

The device parameters that are monitored include the gate-emitter voltage (V_{GE}), collector-emitter current (I_{CE}), collector-emitter voltage (V_{CE}) and case and package temperatures. The data is stored in a structure array that is compatible with MATLAB. This allows for easy interface with diagnostic and prognostic algorithms that are developed using MATLAB. The aging system is autonomous. The user only

initiates the test sequence. When the device under test fails, the system shutdown is initiated automatically.

Hardware

IGBT aging was performed under a resistive load. A schematic of the IGBT resistive load circuit is shown in Figure 2-1. The relationship between the I_{CE} and V_{CE} is given by Equation (2.1). It is observed that there is an inverse relationship between the two parameters under this aging condition.

$$V_{CE} = V_s - I_{CE} R_{Load} \tag{2.1}$$

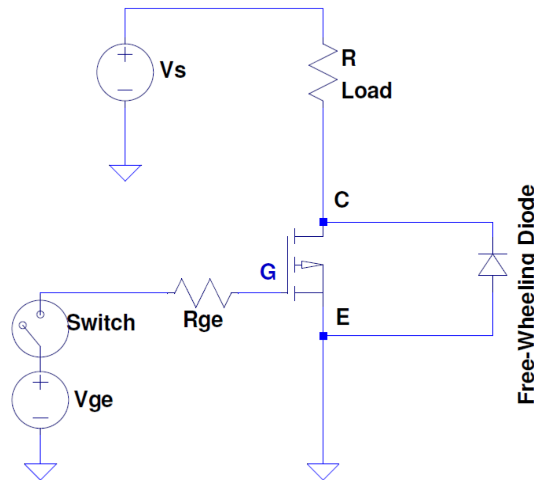

Figure 2-1: IGBT under a resistive load

Figure 2-2 shows the schematic of the IGBT Aging System. The hardware consists of a 300MHz Agilent DSO5034A oscilloscope with 1ns sample time and 1MB memory, a 20 MHz Agilent 33220A function generator for generating gate signals, a National Instruments PCI-6229 data acquisition and source card, a input/output connector block containing SCC-TC02 thermocouple measurement

modules, a Agilent 6652A 25A/20V DC programmable power supply and a PC with LabVIEW.

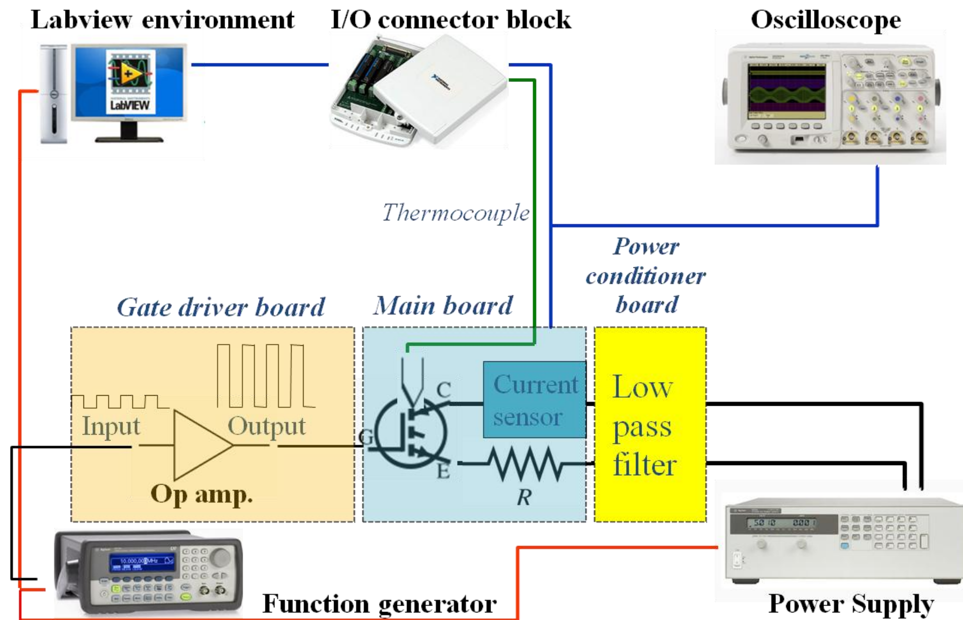

Figure 2-2: IGBT Aging System

The function generator provides the input signal to the gate driver. This signal is amplified by the gate driver board and is used to turn on the IGBT. The main function of the IGBT gate driver board is to amplify the signal voltage from the function generator to the IGBT gate. It has four channels that can be used to drive four discrete devices, however just one channel was used to run the experiment. The gate driver board houses a LM7171 non-inverting operational amplifier as shown in Figure 2-3. The board accepts a signal input range from 0.2 to 1.8V, the linear amplifier amplifies the signal with an adjustable gain ranging from 2 to 18V. Its gain is approximated by: Gain=1+ R2/R1. R1 is a potentiometer and its resistance is variable, however the default value is set to 50 ohms. Resistor R2 is 511 ohms.

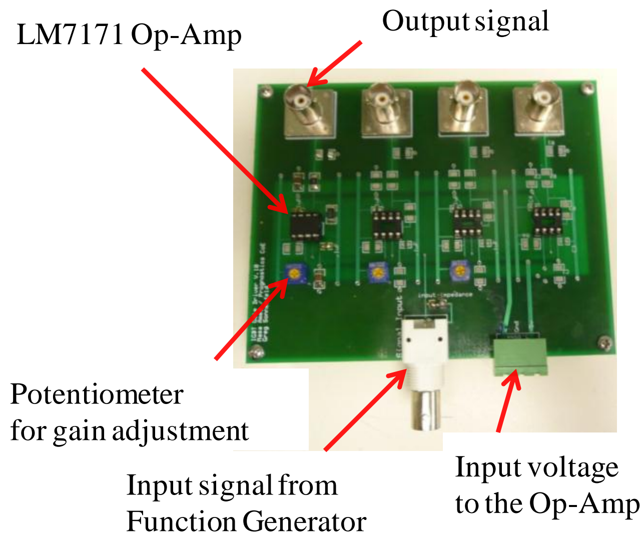

Figure 2-3. Gate Driver Board

The main board as shown in Figure 2-4 houses the terminal block for the IGBT device and BNC output ports. The BNC output ports are used to transfer the gate-emitter voltage (V_{GE}), collector-emitter voltage (V_{CE}) and collector-emitter current (I_{CE}) signals to the Oscilloscope. The main board also houses a 200 KHz Hall-effect current sensor with a 100A maximum current rating, an infrared temperature sensor port, and a bank of 30Hz low-pass filtered output ports connected to the National Instruments PCI-6229 data acquisition card. A Tenma 0-30V DC power supply (not shown in Figure 2-2) is used to provide power to the Hall-effect current sensor and to the gate driver board.

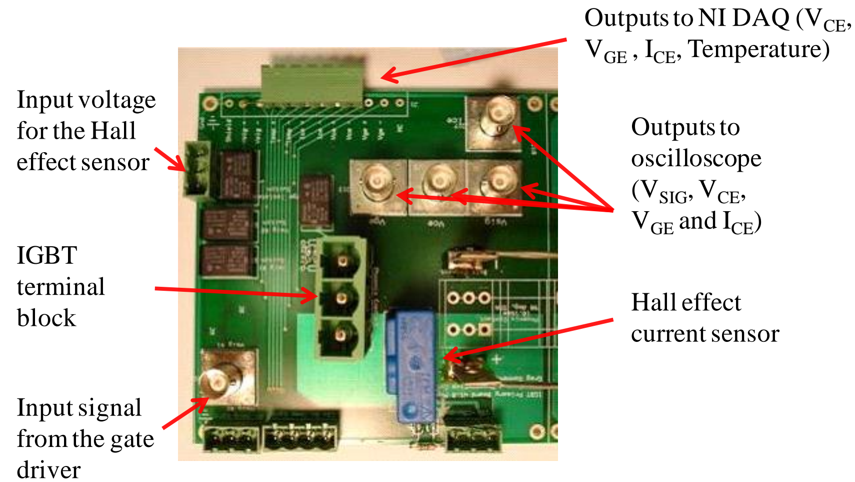

Figure 2-4: Main board

Temperature monitoring is performed using an Infrared sensor focused on the front surface of the package or by thermocouples attached to the case of the IGBT. Thermocouples are connected to the thermocouple module which converts the temperature to a voltage which is then recorded by the data acquisition system (DAQ). The power conditioner board is designed to remove power supply interference and line inductance from the test system. This acts as an ideal power source providing a known voltage source. The conditioned power is supplied to the collector-emitter terminals of the IGBT.

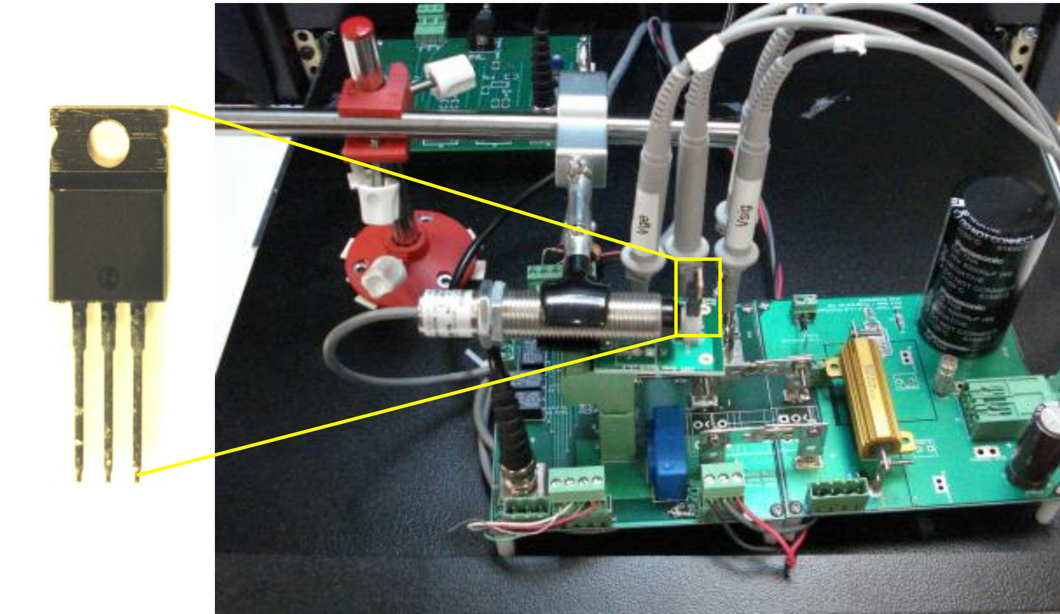

Figure 2-5: Assembled test board

The board assembly which is shown in Figure 2-5 consists of the main board and the power conditioner board which are assembled into a single unit. The load resistor is located on the power conditioner board.

Software

The aging software consists of programs to control the aging process, initiate and record measurements, and shut the system down upon device failure. The aging software was developed in LabVIEW. LabVIEW, an abbreviation for Laboratory Virtual Instrument Engineering Workbench, is a programming environment in which programs are created using a graphical interface. It differs from traditional programming language like C, C++, or Java, in which you program with text. Execution is determined by the structure of a graphical block diagram on which the programmer connects different function nodes by drawing wires.

The schematic of the aging process used to age the IGBTs in this study is shown in Figure 2-6. The IGBTs were power cycled under a resistive load with a predefined frequency, duty cycle, gate voltage and collector-emitter voltage. The device switching was controlled by temperature limits. The device under test (DUT) was switched on and off using a function generator. The device temperature increased with switching as a result of conduction and switching losses. When the temperature rose beyond a pre-set level T_{max}, device switching was stopped. Switching was resumed again when the temperature fell below a pre-set value of T_{min}. No external heat-sink was attached to the device and no external cooling was provided.

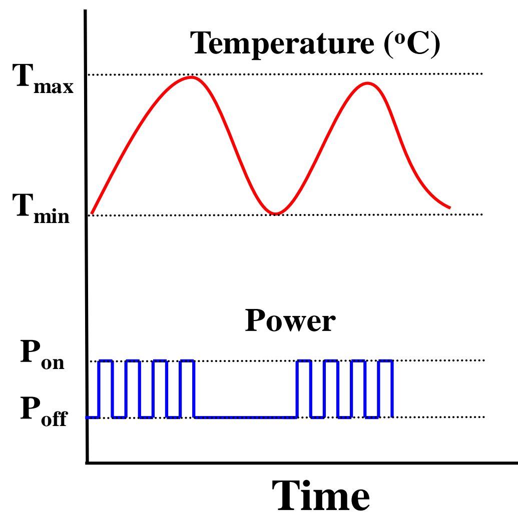

Figure 2-6: Schematic of the aging process

LabVIEW programs/subroutines are called virtual instruments (VIs). Two LabVIEW virtual instruments (VI's) were developed. The first VI, called the aging VI was used to control the function generator based on temperature measurements. The second VI called the data storage VI was used to acquire and store voltage, current and temperature data.

The aging VI turns the function generator on when the package or case temperature falls below a minimum set temperature T_{min}. The aging VI also stores the collector-emitter current (I_{CE}) every 400ms. While the aging VI is running, the data storage VI stores data into a MATLAB structured array file. The function generator is turned off when the temperature goes beyond T_{max}. If the device latches up, the I_{CE} increases rapidly. A maximum current threshold is set for the I_{CE}. When the current exceeds this threshold, the function generator and the power supply providing voltage to the collector-emitter terminals of the IGBT is turned off.

The primary task of the data storage VI is to acquire and store waveforms of the V_{GE}, V_{CE} and I_{CE} using the oscilloscope along with the discrete values of temperature and time into a measurement file. An example of a snapshot of the waveforms acquired by the oscilloscope is shown in Figure 2-7. The frequency of waveform data storage for the experiments performed in this study was varied. For short duration aging experiments (~ 1 hour), waveform data was stored every 400 ms with a resolution of 0.2μs. For long duration experiments (~ 1 day), waveform data was stored every second with a resolution of 1μs.

Figure 2-7: Example of waveforms acquired by the oscilloscope

The MATLAB structure array is shown in Figure 2-8. The benefit of a structure array is the ability to store information of different data types within a given array. As is shown in the diagrams above, the “measurement” variable is a cluster of arrays (in this case it is a 1x29897 one dimensional array) .Within each cell of the array, discrete values of the time and temperature are stored along with three waveform arrays (V_{GE}, V_{CE} and I_{CE}). These waveforms are used in the data analysis which is described in the next chapter.

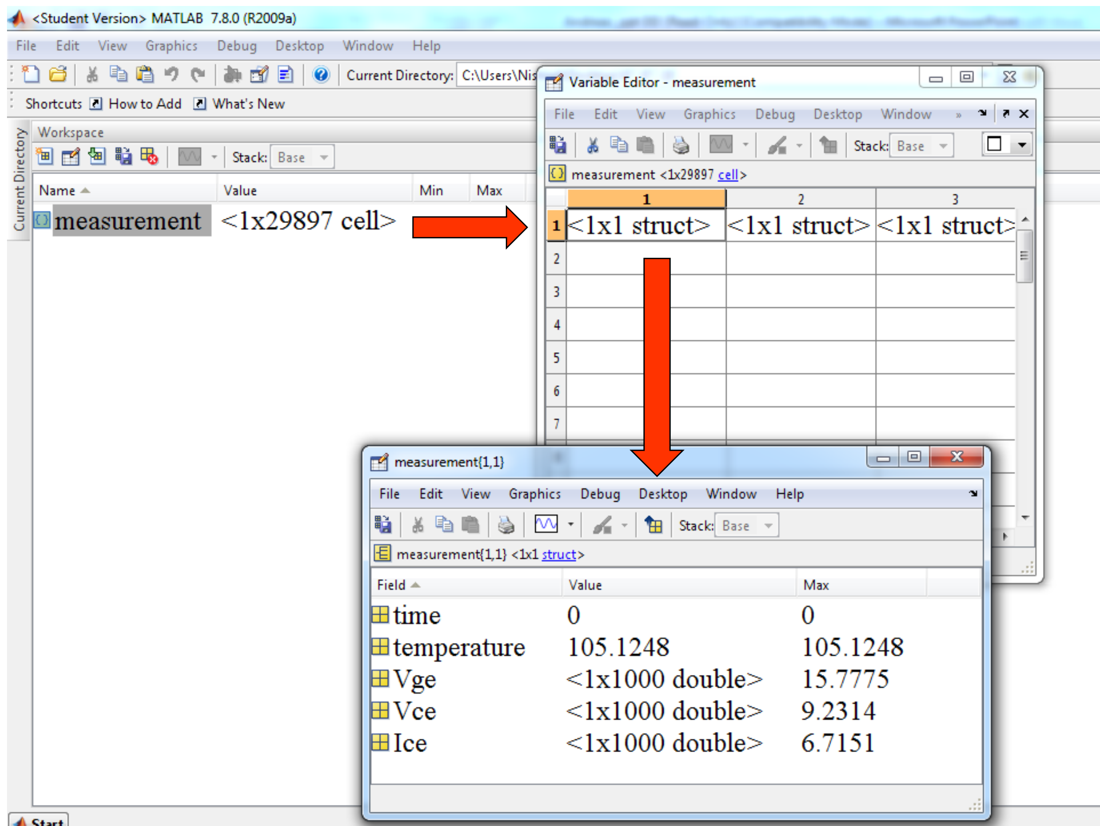

Figure 2-8. MATLAB structure array

Chapter 3. Aging Tests and Degradation Analysis

Power cycling simulates the thermal and current pulsing stresses that devices encounter in actual circuit applications and this test is frequently used for IGBT reliability assessment. The failures caused by power cycling are attributed to thermal cycling induced by the repeated switching of the transistors. The main failure mechanism in operation during power cycling is thermo-mechanical fatigue of wire bonds and solders [26]. The failure modes observed include opens and thermal runaway. Emitter bond wire lifting is commonly observed [27] [28] [29]. Wire lift is attributed to high tensile stresses developed due to the induced temperature cycles and fabrication issues such as poor binding pressure and contamination.

Cova and Fantini [26] performed power cycling tests on 10A-600V IGBT power modules by current stressing. The junction temperature T_j (90°C, 100°C, 120°C) and ΔT (50°C, 60°C, 65°C, 70°C) was varied in these tests by varying the duty cycle. All the IGBTs tested failed due to an open between the collector and emitter. The emitter wire bonds were found to be damaged or broken. An exponential decrease in lifetime was found with increase in ΔT. No significant correlation between lifetime and T_j was observed in this test.

Die attach solder degradation is also frequently observed in power cycling tests [31]. High cyclic shear stresses are induced in the solder as a result of temperature gradients and CTE mismatch. These stresses lead to the solder fatigue and voiding that increases the thermal resistance. The increased thermal resistance

causes device temperatures to rise resulting in catastrophic burn-out failures or secondary breakdown [30].

Morozumi et al. [32] reported the failure sites to be different based on the magnitude of temperature swings and solder composition. In this study, it was reported that IGBTs that use lead based solders failed due to wire lift-off when $\Delta T_j > 100$, and due to solder fatigue when $\Delta T_j < 80$. The cracks occur at the edge of the solder/die interface. However, with lead-free solders, no wire lift-off was observed. However, die solder fatigue occurred at $\Delta T_j > 110$, with solder degradation predominantly in the solder area below the die center .

In this study, powers cycling aging tests were performed on discrete non punch through (NPT) IGBTs (IRGB15B60KD) manufactured by International Rectifier. The IGBT devices were packaged in a TO-220A package along with a soft recovery diode. The devices were rated for a collector-emitter voltage of 600V and gate-emitter voltage of 20V. The maximum junction temperature rating was 150°C.

Aging Procedure

The IGBTs were repeatedly switched under a resistive load with a predefined frequency, duty cycle, gate voltage and collector-emitter voltage. The device switching was controlled by temperature limits. The device under test (DUT) was switched on and off using a function generator. The device temperature increased with switching as a result of conduction and switching losses. When the temperature rose beyond a pre-set level T_{max}, device switching was stopped. Switching was resumed again when the temperature fell below a set value of T_{min}. No external heat-

sink was attached to the device and no external cooling was provided. The schematic of the aging profile is shown in Figure 3-1.

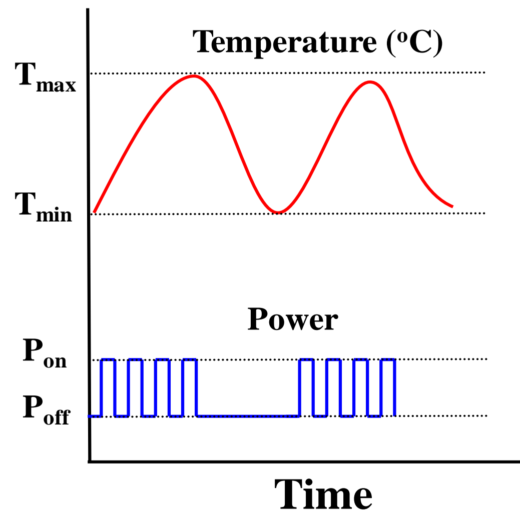

Figure 3-1: Aging Schematic

Test Condition 1

In the first test condition, the aging of IGBTs was performed with a gate voltage of 15V, 50% duty cycle, and a collector-emitter voltage of 5V. The switching circuit consisted of a load resistance of 0.2Ω. Temperature monitoring was performed using an infrared sensor focused on the front surface of the TO-220A package. T_{mean} in the experiments was set to 300°C and the minimum and maximum temperatures were set to a range of ±15°C from the mean temperature. In this aging condition, failures observed were either due to latch-up (loss of gate control leading to increase in collector emitter current) or failure to turn-on. The failure mode and failure times for the devices tested are given in Table 3-1.

Table 3-1: Failure time and failure mode for NPT IGBTs under test condition 1

Device ID	**Failure Time (Minutes)**	**Failure Mode**
N1	47.1	Latch-up
N2	55.8	Failure to turn-on
N3	48.7	Latch-up
N4	60.0	Failure to turn-on
N5	39.4	Latch-up
N6	56.2	Failure to turn-on
N7	42.6	Latch-up
N8	41.0	Latch-up
N9	54.8	Latch-up
N10	34.8	Latch-up

In-situ measurement of the gate-emitter voltage, collector-emitter voltage, collector-emitter current and package temperature was performed until failure of the IGBT under test and recorded using a National Instruments data acquisition system (NI-DAQ). The monitoring of the collector-emitter current was performed every 400ms which allowed for detection of latch-up. Latch-up failure mode observed for NPT IGBT "N3" is shown in Figure 3-2. The collector-emitter current is observed to be in the range of 4 to 8A before latch-up. The current peaks represent the current as the IGBT heats up from T_{min} to T_{max}. The current reduces to zero as the IGBT cools down to T_{min} before the aging cycle begins again. At latch-up the current exceeds 12A upon which the collector-emitter voltage supply was cut-off to prevent device burn-out.

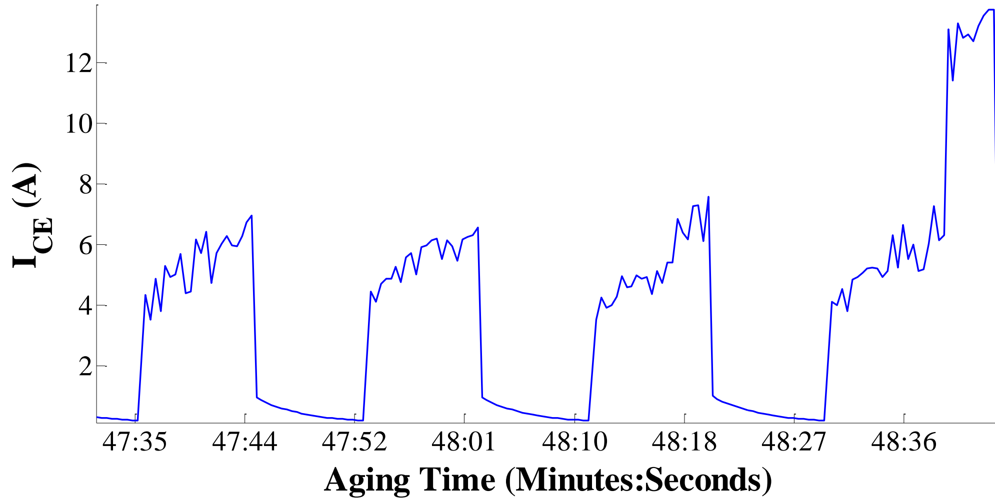

Figure 3-2: Latch-up of NPT IGBT “N3” aged under test condition 1

Periodically during the aging process, a square gate pulse of magnitude 1.5 times greater than the aging pulse with a 1ms duration and 50% duty cycle was applied to the gate. The collector-emitter current and collector-emitter voltage response to this gate pulse was recorded using an oscilloscope as shown in Figure 3-3 and Figure 3-4.

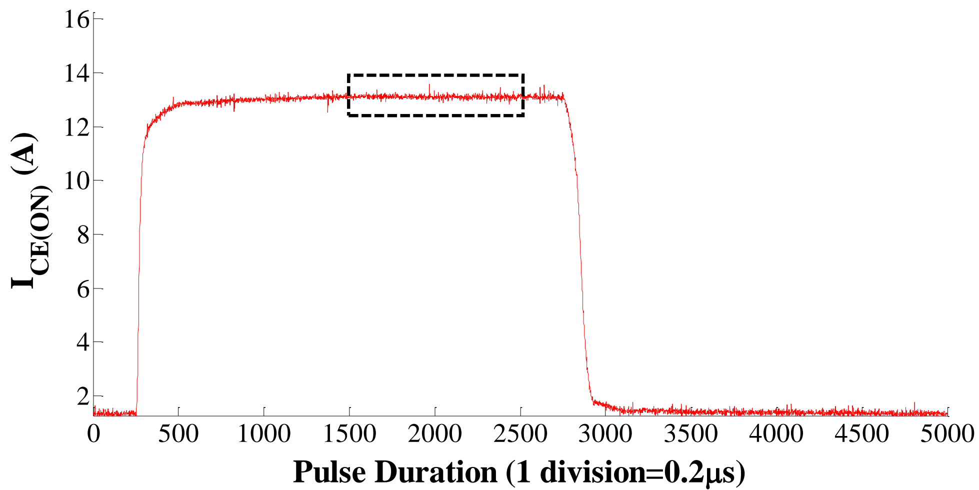

Figure 3-3: Collector-emitter current response to input gate pulse

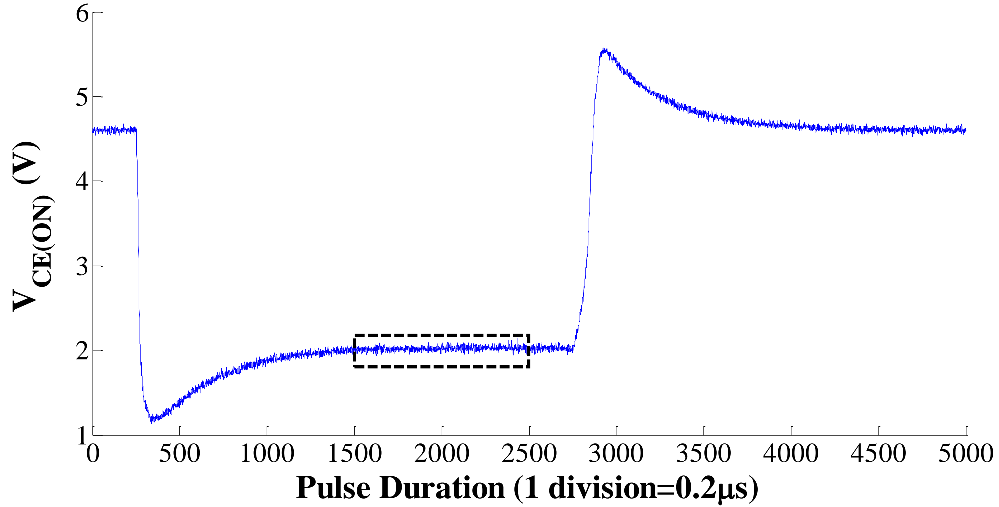

Figure 3-4: Collector-emitter voltage response to input gate pulse

Data Analysis for Test Condition 1

To determine the effects of aging without the influence of temperature changes, the collector-emitter voltages and currents at the mean aging temperature of 300°C were extracted for this study. For every collector-emitter current and voltage waveform obtained at the mean aging temperature, a portion of the waveform was sampled in the transistor on-state. A total number of 1000 points were sampled as depicted by the window shown in Figure 3-3 and Figure 3-4. The mean of these 1000 points was then plotted against aging time as shown in Figure 3-5 for NPT IGBT N3.

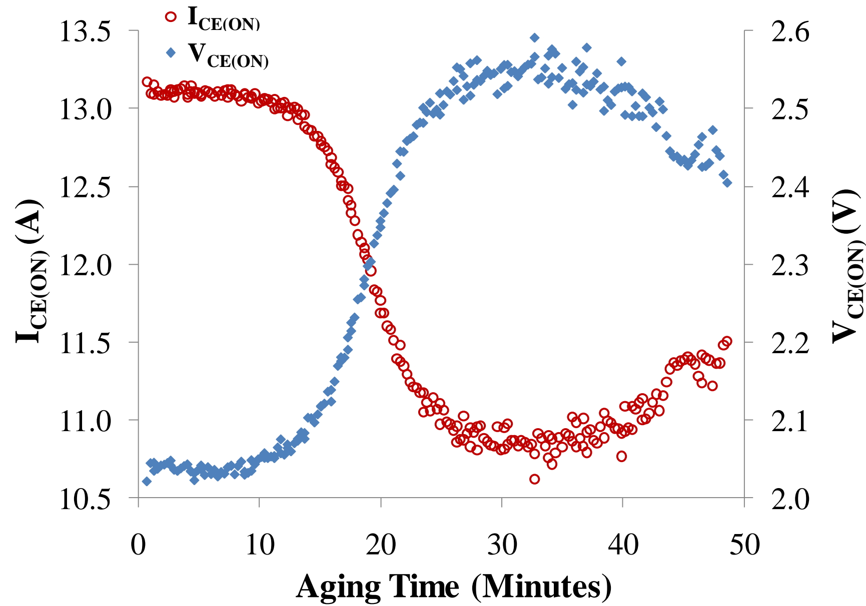

Figure 3-5: $I_{CE(ON)}$ and $V_{CE(ON)}$ vs. aging time for NPT IGBT "N3" aged by test condition 1

The on-state collector-emitter current ($I_{CE(ON)}$) was observed to reduce with aging and the on-state collector-emitter voltage ($V_{CE(ON)}$) increased. Finally, failure occurred by two modes. The first failure mode was loss of gate control due to latch-up as a result of the activation of the parasitic thyristor inherent in the device structure. The second failure mode was an increase in device resistance to an extent wherein the device failed to turn-on.

Electrical Characterization for Test Condition 1

I-V characteristics were measured at gate voltages ranging from 8 to 9.5 V at room temperature using the Tektronix 371A curve tracer before and after aging of the IGBTs. The I-V characteristic for an aged NPT IGBT that latched-up is shown in Figure 3-6. This I-V characteristic shows an internal short in the IGBT due to electrical overstress as a result of latch-up. The I-V characteristic for an aged NPT

IGBT that failed to turn-on is shown in Figure 3-7. The I-V characteristics show increased resistance of the device with aging.

Threshold voltage measurements were performed before and after aging. For the devices that did not have a gate short, the threshold voltage was found to have increased by 200-300 mV indicating gate oxide degradation had occurred during the tests.

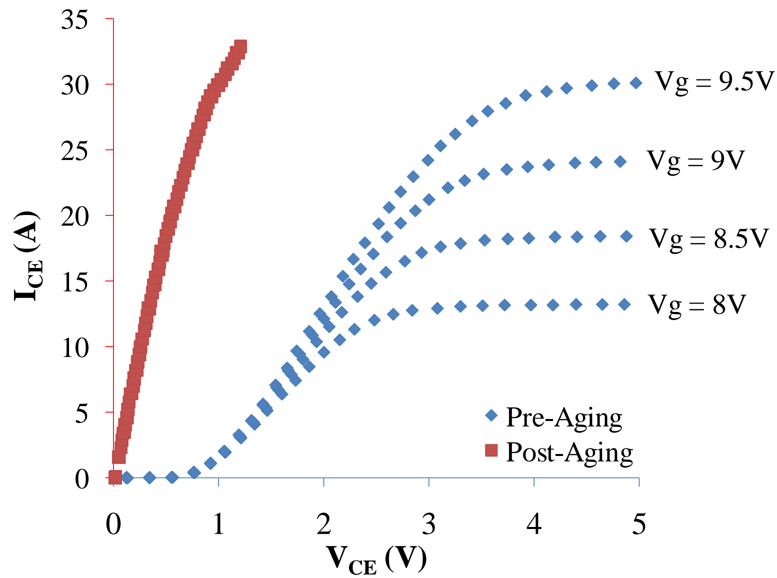

Figure 3-6: I-V characteristics (room temperature) for IGBT N3 aged by test condition 1

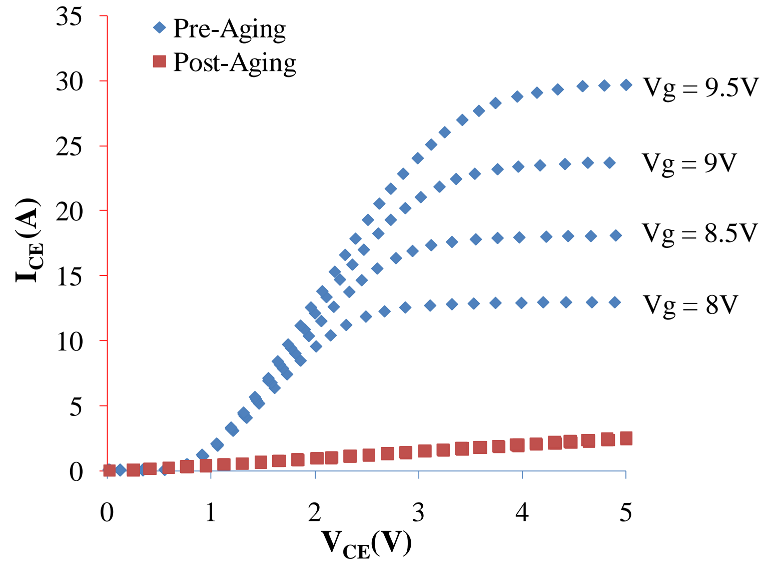

Figure 3-7: I-V characteristics (room temperature) for IGBT N2 aged by test condition 1

X-ray Analysis for Test Condition 1

X-ray analysis of the IGBTs was performed before and after aging to determine degradation in the die attach. The X-ray images of one aged NPT IGBT is shown in Figure 3-8. In the X-ray images, the larger die attach corresponds to the IGBT, and the smaller die attach to the free-wheeling diode. Test condition 1 was observed to cause die attach degradation in all the IGBTs tested.

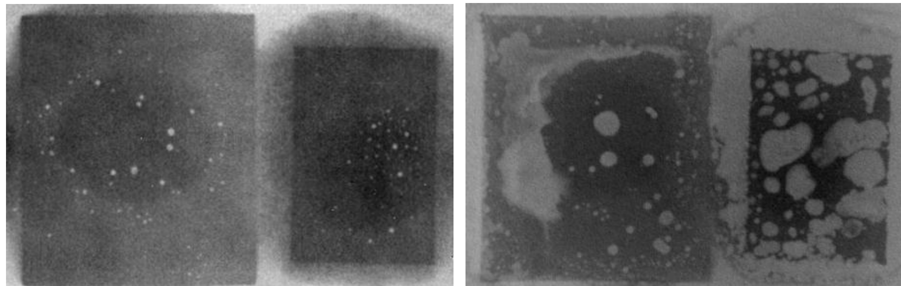

Figure 3-8: Before (left) and after (right) X-ray images of NPT IGBT aged by test condition 1

Test Condition 2

In the second test condition, the aging of IGBTs was performed with a gate voltage of 15V, 50% duty cycle, and a collector-emitter voltage of 9V. The switching circuit consisted of a load resistance of 0.5Ω. Temperature monitoring was performed using a T-type thermocouple attached to the heat-sink of the TO-220A package. Tmean in the experiments was set to 150°C and the minimum and maximum temperatures were set to a range of ±50°C from the mean temperature. In this aging condition, failures observed were the same as in test condition 1.

Table 3-2: Failure time and failure mode for test condition 2

Device ID	**Failure Time (Hours)**	**Failure Mode**
NPT1	19.2	Latch-up
NPT2	31.6	Failure to turn-on
NPT3	27.0	Latch-up
NPT4	24.2	Failure to turn-on
NPT5	12.3	Latch-up

The failure times and failure modes are given in Table 3-2. The failures occurred due to latch-up (loss of gate control leading to increase in collector emitter current) as shown in Figure 3-9 or failure to turn-on as shown in Figure 3-10.

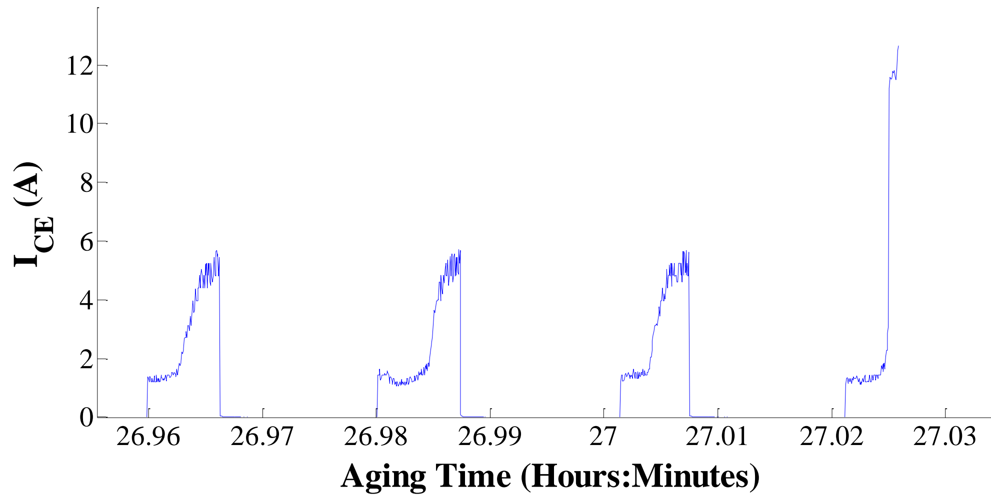

Figure 3-9: Latch-up of NPT IGBT “NPT2” aged by test condition 2

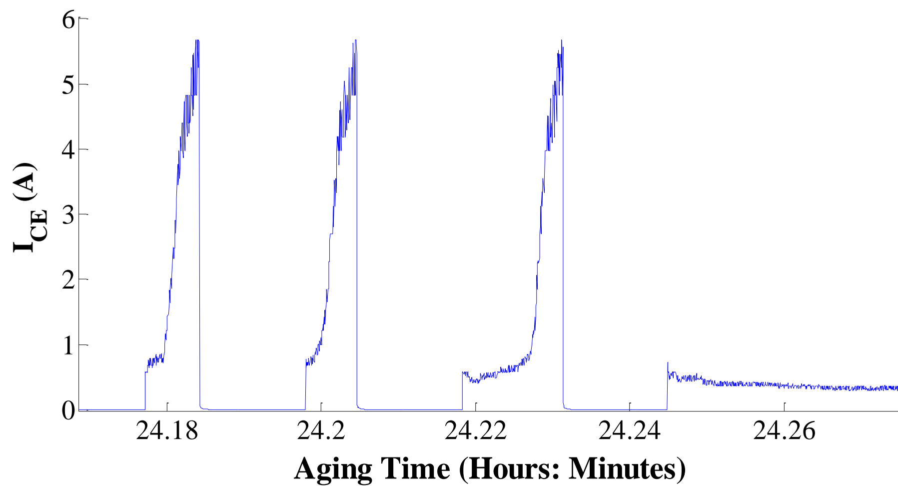

Figure 3-10: NPT IGBT “NPT3” aged by test condition 2 failed to turn-on

Data Analysis for Test Condition 2

Similar to test condition 1, the on-state collector-emitter current ($I_{CE(ON)}$) was observed to reduce with aging and the on-state collector-emitter voltage ($V_{CE(ON)}$) increased in test condition 2 as observed in Figure 3-11.

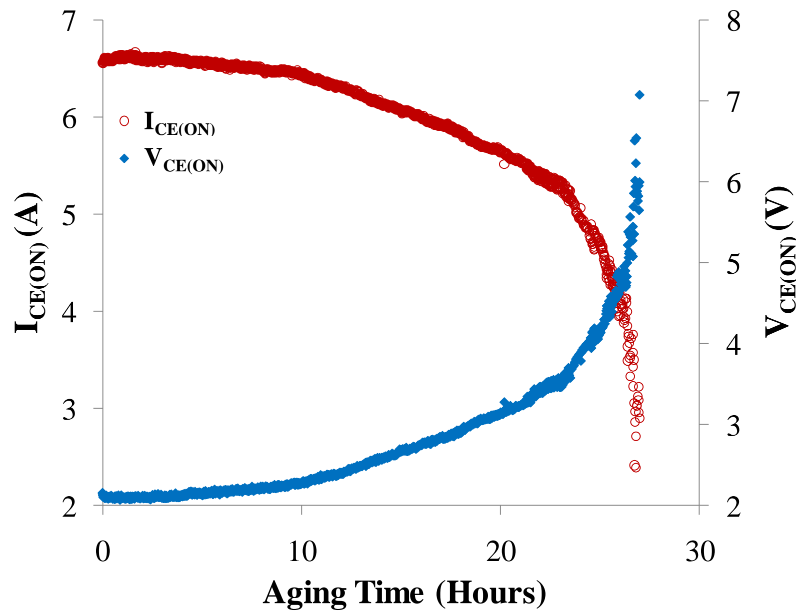

Figure 3-11: $I_{CE(ON)}$ and $V_{CE(ON)}$ vs. aging time for NPT IGBT "NPT3"

I-V characterization of an IGBT aged by test condition 2 is shown in Figure 3-12. This device failed to turn-on. The I-V characteristics are similar to those obtained in test condition 1. The threshold voltage was measured before and after aging. For the parts that did not exhibit a gate short, the aging was found to result in an increase in the threshold voltage by 100-300 mV indicating gate oxide degradation during the test.

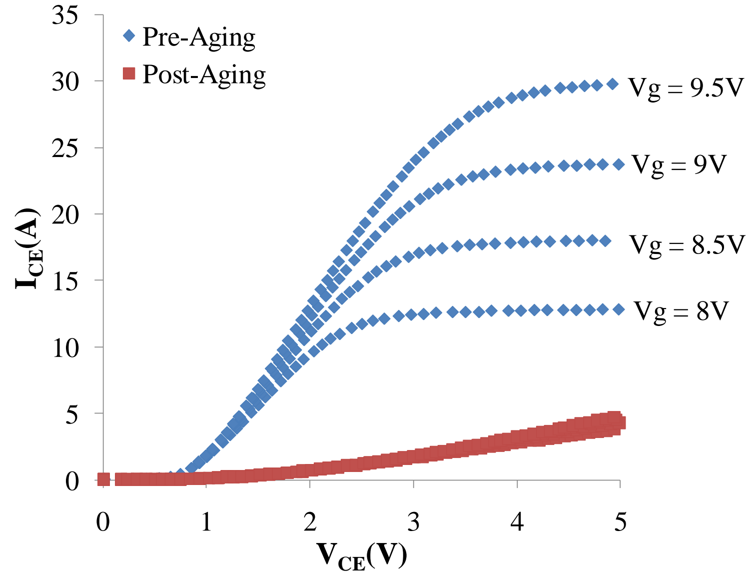

Figure 3-12: I-V characteristics (room temperature) for IGBT NPT2 aged by test condition 2

X-ray Analysis for Test Condition 2

The X-ray images of the NPT IGBT aged by test condition 2 are shown in Figure 3-13. Similar to test condition 1, test condition 2 also results in degradation of the die attach.

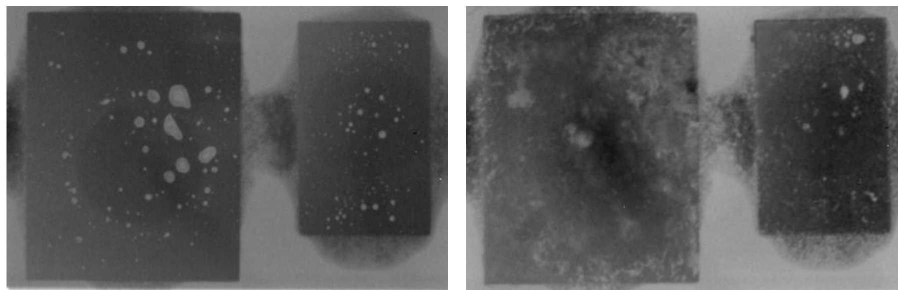

Figure 3-13: Before (left) and after (right) X-ray images of NPT IGBT aged by test condition 2

Failure Mechanisms and Acceleration Factor

The main failure mechanism in operation during the power cycling aging tests was the thermo-mechanical fatigue of the lead free solder die attach. The mean aging

temperature of test condition 1 was 300°C with a ΔT of 30°C. For test condition 2, the mean aging temperature was 150°C with a ΔT of 100°C . The mean time to failure for test condition 1 was 48.04 minutes. The mean time to failure for test condition 2 was 1375.2 minutes. The acceleration factor obtained by using the ratio of the failure times is given by Equation (3.1)

$$AF = \frac{t_{150°C}}{t_{300°C}} = \frac{1357.2}{48.04} = 28.6 \qquad (3.1)$$

The acceleration factor obtained by this method may provide inaccurate predictions of IGBT lifetime at a different temperature as the aging tests were performed for only two test conditions. The die attach in the IGBTs tested is a lead free J alloy. A previous study on J-alloy degradation [33] in power devices reports the acceleration factor by using the Coffin-Manson equation as given by Equation (3.2)

$$AF = \left(\frac{\Delta T_A}{\Delta T_U}\right)^q \qquad (3.2)$$

where ΔT_A is the temperature swing at the high stress condition, ΔT_U is the temperature swing at the low stress condition and q is the fit parameter for the fatigue failure mechanism. The power device lifetime is a function of the thermal resistance of the die attach. It has been reported that the degradation of the thermal resistance of the J-alloy die attach is a function of the structure and composition of the die attach layer, the size of the die as well as the attachment process [33]. To obtain a better estimate of the acceleration factor, thermal cycling tests will have to be performed under several different ΔT conditions to obtain the *q* fit parameter.

From the $V_{CE(ON)}$ and $I_{CE(ON)}$ data, it is not possible to predict the two failure modes which are “latch-up” and “failure to turn-on”. For both the failure modes, an

increase in the $V_{CE(ON)}$ was observed with a reduction in the $I_{CE(ON)}$ as shown in Figure 6-1 and Figure 6-2. For test condition 2 as well, it is not possible to distinguish the two failure modes as shown in Figure 6-10 and Figure 6-11 .

Latch up in IGBTs occurs by the activation of the parasitic thyristor inherent in the device. The latch up current required for activation of the parasitic thyristor reduces with an increase in temperature. For example, in one study on NPT IGBTs, it was reported that the current required to activate the parasitic thyristor reduced from 60 A at room temperature to 10 A at 200°C [34]. The latching current is given by the expression [7].

$$I_{CE(Latch)} \propto \frac{V_{bi}}{\alpha_{pnp}\rho_{sp}L_E} \tag{3.3}$$

where $I_{CE(latch)}$ is the current required to activate the parasitic thyristor, V_{bi} is the built in potential of the N^+-P emitter base junction, α_{pnp} is the gain of the PNP bipolar transistor, ρ_{sp} is the sheet resistance of the p-base and L_E is the length of the emitter. With an increase in the temperature, the gain of the bipolar transistor and the sheet resistance of the p-base increases leading to a reduction in the collector current required for IGBT latch-up [35].

The power cycling of the IGBTs in this study resulted in die attach degradation. The die attach degradation led to an increase in the temperature within the device due to the increased thermal impedance. With rise in temperature, the current required for latch up reduced. In some of the IGBTs that were aged, the increase in temperature was high enough to cause latch up of the IGBT. In the devices that did not latch-up, failure eventually occurred as a result of increased device

resistance that prevented the IGBT from turning on. This hypothesis is supported by observing the failure times for test condition 1 as given in Table 3-1. For test condition 1, it was observed that latch-up failures occurred earlier than the failure to turn on. For test condition 2 (Table 3-2) also, it is observed that failure by latch up occurred earlier than the failure to turn on for all but one device. One possible method to predict latch up of the IGBT is by monitoring the junction temperature. By monitoring the junction temperature, one may be able to determine a threshold temperature beyond which latch up failure can be predicted.

Measurement of Junction Temperature

The junction temperature of the IGBT can be determined from the collector-emitter voltage (V_{CE}) measurements as the V_{CE} is a temperature sensitive parameter. The V_{CE} is also dependent on the collector-emitter current (I_{CE}) and gate-emitter voltage (V_{GE}). To estimate the junction temperature from the V_{CE}, the IGBT needs to be calibrated. Calibration is performed by placing the IGBT device or IGBT module in a thermal chamber. The temperature is then varied in steps. At each temperature step, the device or module is allowed to attain thermal equilibrium before V_{CE} measurement. The V_{CE} is measured using a short duration low amplitude I_{CE} (typically 100mA) at a constant V_{GE}. The short duration and low amplitude I_{CE} reduces the effects of self- heating. The result of the calibration process is a calibration characteristic curve for the IGBT as shown in Figure 3-14. As observed from Figure 3-14, the V_{CE} has a negative temperature coefficient of temperature. This occurs due to the fact that the V_{CE} is measured at I_{CE} of 100mA. At these low current magnitudes, the main contributor to the V_{CE} is the pn junction at the collector

terminal which has a negative coefficient of temperature [34]. With an increase in the I_{CE}, the V_{CE} attains a positive temperature coefficient [36].

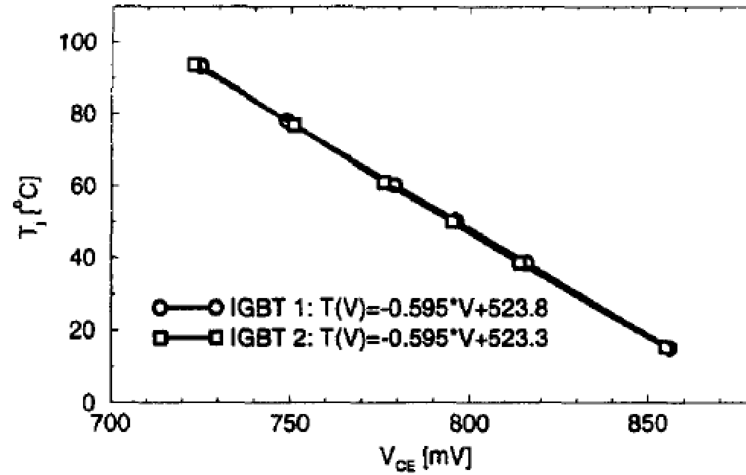

Figure 3-14: Calibration curve (T_j versus V_{CE} at I_{CE} = 100mA) [26]

To determine the junction temperature during aging, the V_{CE} is measured at an I_{CE} of the same magnitude as that used in the calibration process as shown in Figure 3-15 . The measured V_{CE} is then input to the regression equation obtained by calibration to determine the junction temperature. The knowledge of the junction temperature is useful for diagnostics and prognostics as it is allows for monitoring solder degradation in the IGBT package or module. Solder degradation causes variation of thermal resistance which affects the junction temperature. An accurate estimation of the junction temperature improves the assessment of the health of the IGBT.

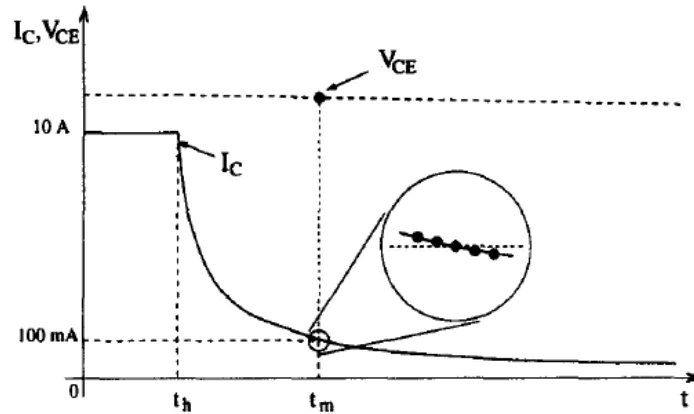

Figure 3-15: V_{CE} measurement during aging process at I_{CE} = 100mA [26]

Summary

Power cycling induced thermal cycling of IGBTs under a resistive load led to failures by latch-up or failure to turn-on in both test condition 1 and test condition 2. The in-situ monitored on-state collector-emitter current showed a decreasing trend while the on-state collector-emitter voltage showed an increase with aging. For the parts that did not exhibit a gate short, an increase in the threshold voltage was observed. This indicates that the aging led to degradation in the gate oxide. X-ray analysis revealed degradation in the die attach for all the IGBTs tested. I-V characterization tests revealed a short in the IGBTs that latched-up.

The die attach is an integral part of the heat dissipation path and its degradation leads to increased thermal impedance. The increased thermal impedance leads to higher device temperatures. Latch-up occurs by the activation of the parasitic thyristor inherent in the IGBT. The susceptibility to latch-up is higher at elevated temperatures as the trigger current for latch-up reduces with increasing temperature

[35] [39]. The die attach degradation can thus be hypothesized to have contributed to the latch-up observed in some of the NPT IGBTs.

The NPT IGBTs exhibited a positive co-efficient of resistance with aging. With increased aging, the resistance of the NPT IGBTs increased. The IGBTs that did not latch-up eventually failed as a result of increased resistance which prevented them from turning on. One additional point to be noted is that latch-up failure is not a hard failure. If the voltage supply is cut-off immediately after latch up thereby preserving the device, it can be operated again. However, the failure to turn on is a hard failure.

The $I_{CE(ON)}$ and $V_{CE(ON)}$ parameters were identified as precursors for NPT IGBTs. These parameters were found to be independent of the two aging conditions, i.e., the parameters exhibited a consistent trend irrespective of the aging condition. These parameters were used for anomaly detection and remaining life estimates as described in the following chapters.

Chapter 4. Anomaly Detection

Anomaly detection refers to the problem of finding patterns in data that do not conform to expected behavior [37]. The importance of anomaly detection techniques is that anomalies in data could be due to changes in the system that lead to malfunction or failure. Therefore, anomaly detection techniques can be used to perform diagnostics. Several anomaly detection approaches have been reported in literature for identifying faults in IGBT power inverters which involve monitoring system level currents and voltages, collector-emitter voltage, gate emitter voltage and collector emitter current for fault diagnosis. These methods have been implemented to identify system level faults and the location of the faulty IGBTs and not to detect faults in the IGBTs themselves [2] [38].

A diagnostic approach was reported for IGBTs in power modules in automotive applications [20]. This approach involved measurement of the IGBT collector-emitter saturation voltage at vehicle start-up and comparison of the measured value to a look-up table that contained healthy values of $V_{CE(sat)}$. A fixed percentage change for $V_{CE(sat)}$ was used as a threshold for signaling of an alarm.

Approaches to implementing anomaly detection depend on the type of data available from the system under consideration. When healthy data from a system is available, anomaly detection can be implemented by determining a detection threshold based on the healthy data in order to identify outliers. Threshold detection therefore is an important step in diagnostics in order to have advanced warning of failure. Threshold values are typically defined based on expert knowledge of known

fault conditions and economic factors such as the need to reduce the number of false alarms. These diagnostic approaches may not be able to detect anomalies when *a priori* knowledge of faults is not available. It is therefore useful to implement a generalized probabilistic approach to determine thresholds for anomaly detection [40].

Mahalanobis Distance

Mahalanobis distance (MD) is a distance measure that is used in applications such as anomaly detection, pattern recognition and process control [41]. In electronics, MD has been used for detecting anomalies in notebook computers [40] and multilayer ceramic capacitors [42]. Kumar et al. [40] developed a probabilistic technique for determination detection thresholds using MD followed by a power transformation of the MD values which are always positive so that they follow the normal distribution. Statistical thresholds were then developed based on the mean and standard deviation of the transformed data.

Anomaly Detection Approach

The MD approach to anomaly detection involves distinguishing between healthy and anomalous data using the distance measure (MD) thus reducing multivariate data to univariate data. MD is sensitive to changes between various parameters monitored as it takes the correlation between the different parameters into account. Additionally, MD is not sensitive to the differing scales of the parameters monitored, as MD values are calculated using normalized parameters.

Monitored data that is known to be healthy is used to calculate the mean and standard deviation for normalization. Further, this healthy data is used to compute the correlation matrix. With the mean, standard deviation and correlation matrix obtained from the healthy data, the MD is calculated for every test data point. The MD values calculated from the healthy data are transformed using the Box-Cox power transformation into the normal distribution. A detection threshold is then calculated based on the mean and standard deviation of the transformed healthy MD data. The calculations are then repeated for every test data using the mean, standard deviation, correlation matrix and Box-Cox transformation parameter learnt from the healthy data. Using this approach anomalies are detected when the transformed MD for a test data point crosses the detection threshold.

In this work, this approach to anomaly detection of discrete IGBTs was investigated. MD was calculated using $V_{CE(ON)}$ and $I_{CE(ON)}$ parameters and a threshold was defined to detect anomalies. To implement the MD approach, $V_{CE(ON)}$ and $I_{CE(ON)}$ data at the mean aging temperature were partitioned into healthy data and test data. The initial observations (approximately the initial five minutes of the test) were classified as healthy data. The entire set of observations was used as test data. The parameters that form the input for MD computation are denoted by i, where $i = 1, 2, \ldots, p$. In our study $V_{CE(on)}$ and $I_{CE(on)}$ were used as input parameters, hence $p = 2$. The number of observations recorded for each parameter is denoted by j, where $j=1,2,\ldots.n$. X_{ij} denotes the value of parameter i at time instance j. Each individual observation of a given parameter in the data vector was normalized using the mean and standard deviation for the parameter as given by Equation (4.1). The mean and

standard deviation for the input parameters was computed by using Equation (4.2) from the healthy data.

$$Z_{ij} = \frac{\left(X_{ij} - \bar{X}_i\right)}{S_i} \tag{4.1}$$

$$\bar{X}_i = \frac{1}{n}\sum_{j=1}^{n} X_{ij}\ ,\ \ S_i = \sqrt{\frac{\sum_{j=1}^{n}\left(X_{ij} - \bar{X}_i\right)^2}{\left(n-1\right)}} \tag{4.2}$$

The healthy MD values were computed by using Equation (4.3) with the normalized parameters obtained from Equation (4.1), where Z_j was the normalized $I_{CE(ON)}$ and $V_{CE(ON)}$ at time j

$$MD_j = \frac{1}{p}\mathbf{Z}_j^T C^{-1}\mathbf{Z}_j \tag{4.3}$$

where C is the correlation matrix. Equation (4.4) was used to calculate the correlation matrix from the healthy data.

$$C = \frac{1}{(n-1)}\sum_{j=1}^{n} Z_j Z_j^T \tag{4.4}$$

To compute the test MD values, the mean and standard deviation obtained from the healthy MD computation was used to normalize the test $I_{CE(ON)}$ and $V_{CE(ON)}$. These normalized test parameters were then used to compute the test MD by Equation (4.3) where the correlation matrix was obtained from the healthy data.

The healthy MD values obtained were found to not follow a normal distribution. The Box-Cox power transformation was used to transform the healthy MD values into a normal distribution. Transforming the healthy MD data into a normal distribution allows for the use of statistical process control rules to determine

if the test data from the device is healthy or unhealthy. This approach has been demonstrated to be effective in threshold estimation for anomaly detection of electronic products [40]. The Box-Cox transformation is defined by the following equations [43].

$$x(\lambda)=\frac{\left(x^{\lambda}-1\right)}{\lambda} \qquad \lambda \neq 0$$
$$x(\lambda)=\ln(x) \qquad \lambda = 0 \tag{4.5}$$

where $x(\lambda)$ is the transformed vector, x is the original vector and λ is the transform parameter.

The Box-Cox transform method attempts to normalize the data by determining the appropriate transform parameter λ. The λ parameter is varied across a range; say -10 to 10 in small increments and the logarithm of the likelihood function (representing the likelihood that the data is distributed according to the normal distribution) is computed as given in Equation (4.6) for each increment of λ. Hence, the parameter with the maximum likelihood is used to transform the data of interest as this parameter is most likely to yield a normal distribution.

$$f(x,\lambda)=-\frac{n}{2}\ln\left[\sum_{i=1}^{n}\frac{\left(x_i(\lambda)-\bar{x}(\lambda)\right)^2}{n}\right]+(\lambda-1)\sum_{i=1}^{n}\ln(x_i) \tag{4.6}$$

$$\bar{x}(\lambda)=\frac{1}{n}\sum_{i=1}^{n}x_i(\lambda) \tag{4.7}$$

The mean (μ) and standard deviation (σ) of the transformed healthy MD values were used to obtain 3σ bounds about the mean using the healthy data. The upper bound (μ+3σ) was used as the detection threshold for anomaly detection as increasing MD values indicate degradation in the IGBT. The test MD values were transformed using Equation (4.5) based on the Box-Cox transform parameter λ

learned from the healthy data. When the transformed test MD values crossed the threshold, an anomaly was said to have occurred.

Anomaly Detection for Test Condition 1

The $I_{CE(ON)}$ and $V_{CE(ON)}$ data obtained from the IGBTs aged in test condition 1 were partitioned into healthy data and test data. The first 50 observations (corresponding to the initial 5-8 minutes of the test) of $I_{CE(ON)}$ and $V_{CE(ON)}$ obtained at the mean aging temperature of 300°C were used as healthy data and the entire dataset was used as test data. For each IGBT, the healthy data was normalized by computation of the mean and standard deviation of each parameter using Equation (4.2).

The histogram of the healthy MD data obtained from IGBT "N3" is shown in Figure 4-1. The mean and standard deviation were found to be 13.1A, 0.027 and 2.03V, 0.007 respectively for I_{CE} and V_{CE} from the healthy data. From the histogram, we observe that 90% of the healthy MD values have a value less than 2.

This normal probability plot in Figure 4-2 shows the healthy MD data plotted against a theoretical normal distribution. The normal probability plot is a graphical technique to assess the normality of a given distribution. The healthy MD values do not exhibit a normal distribution as seen in Figure 4-2. To transform the healthy MD distribution to a normal distribution, a Box-Cox transformation was used.

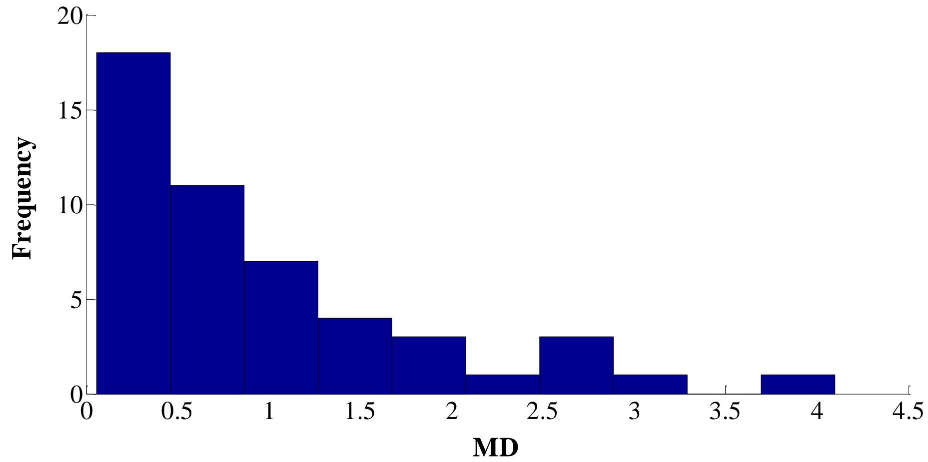

Figure 4-1: Histogram of the healthy MD values for IGBT "N3"

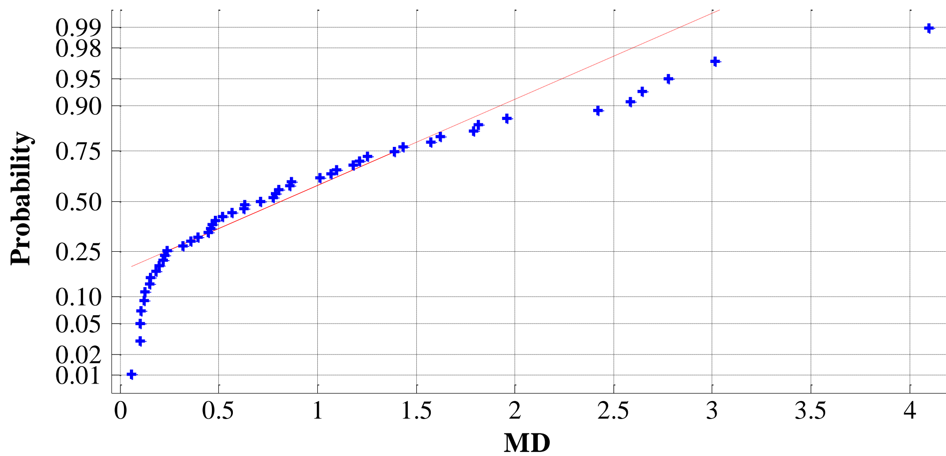

Figure 4-2: Normal probability plot of the healthy MD data for IGBT N3

The λ parameter was varied from a range of -10 to +10 in increments of 0.1. The logarithm of the likelihood function given in Equation (4.6) was computed for each λ value. For IGBT N3, the maximum likelihood was obtained at a value of λ = 0.1. This parameter was used to transform the healthy MD data. The healthy data after the Box-Cox transformation is shown in Figure 4-3. From Figure 4-4, we observe that the transformed MD data is approximately normally distributed.

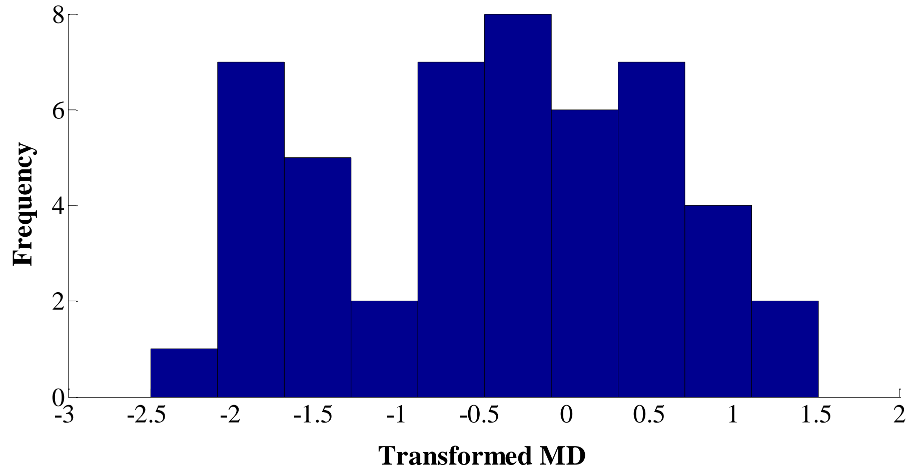

Figure 4-3: Transformed healthy MD data for IGBT N3

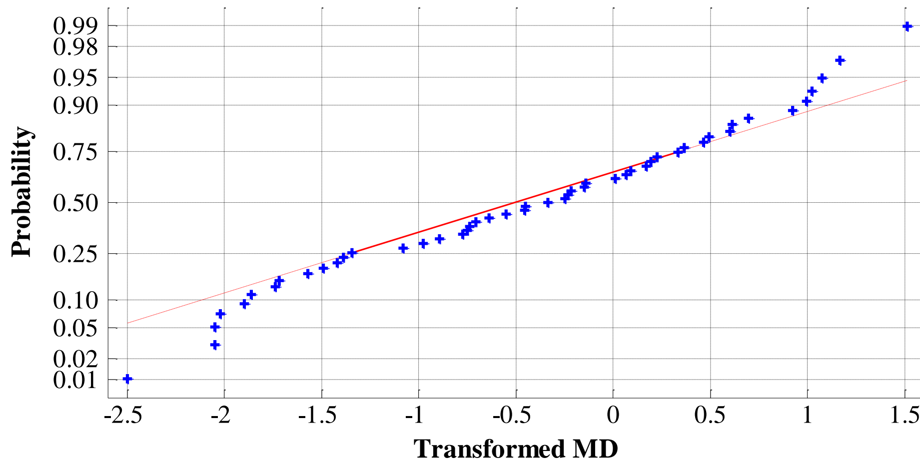

Figure 4-4: Normal probability plot of the transformed healthy MD data for IGBT N3

The mean and standard deviation of the transformed healthy data was computed. The threshold for anomaly detection was defined as $\mu+3\sigma$. The detection threshold for N3 was found to be 2.6. The upper bound was considered as an increase in MD values indicates degradation of the device. The test MD data was computed using Equation (4.3), wherein the mean, standard deviation and the inverse correlation matrix was obtained from the healthy MD data. The test MD data was

then transformed using the Box-Cox transform. The time when the transformed test MD data crossed the threshold was considered as the time when the anomaly was first detected.

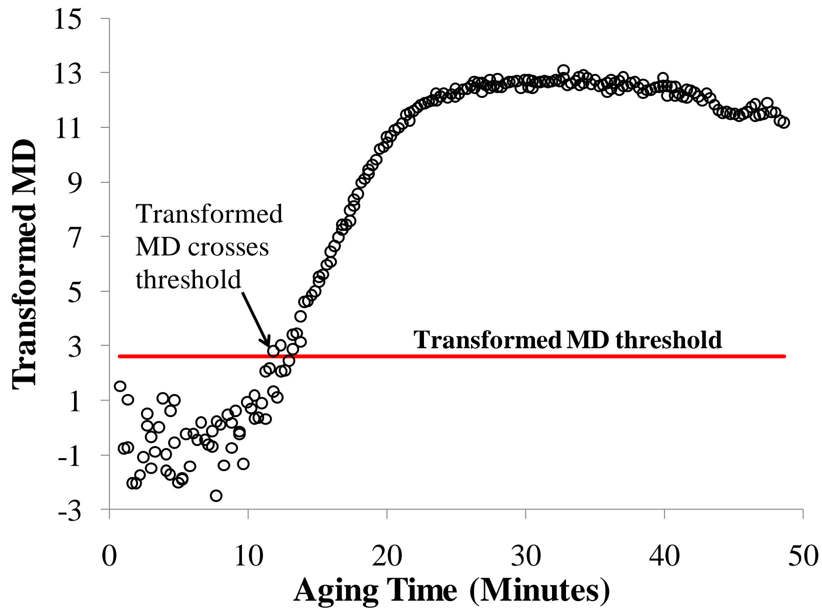

Figure 4-5: Transformed MD data vs.ing time for IGBT "N3"

The anomaly in the N3 IGBT was detected at 11.8 minutes as shown in Figure 4-5. Similar analysis was performed for all the IGBTs aged under test condition 1. In power cycling tests performed on IGBTs, a percentage change in V_{CE} is typically used as failure criteria [44] [45]. The magnitude of the percentage change used as the failure criteria is dependent on application [45]. In this study, a 20% increase in $V_{CE(ON)}$ was chosen as a parametric failure criteria [49][50].

Two metrics are computed for quantifying the anomaly detection time obtained from the MD analysis. The first metric is defined as the % time to parametric failure after anomaly detection. This is the ratio of the difference between

the anomaly detection time and time to 20% increase in $V_{CE(ON)}$, and the time to 20% increase in $V_{CE(ON)}$.

The second metric is defined as % time to functional failure after anomaly detection. This is the ratio of the difference between the anomaly detection time and time to functional failure, and the time to functional failure. Functional failure refers to the time when the IGBT latched-up or failed to turn-on. This failure time corresponds to the failure times reported in Chapter 3, Table 3-1. The anomaly detection times obtained for the IGBTs in test condition 1 is provided in Table 4.1 along with the two metrics.

Table 4-1: Anomaly detection times obtained for test condition 1

Device ID	**Detection time using transformed MD (Minutes)**	**Time for 20% increase in $V_{CE(ON)}$ (Minutes)**	**Failure time (Minutes)**	**% Time to parametric failure after detection using transformed MD**	**% Time to functional failure after detection using transformed MD**
N1	13.8	24.3	47.1	43.2	70.8
N2	12.8	22.8	55.8	43.8	77.1
N3	11.8	21.4	48.7	44.8	75.8
N4	18.7	23.6	60.0	20.7	68.9
N5	11.4	23.1	39.4	50.7	71.0
N6	12.0	21.5	56.2	44.2	78.7
N7	16.2	22.4	42.6	27.7	62.0
N8	17.2	24.6	41.0	30.1	58.0
N9	14.6	24.8	54.8	41.1	73.3
N10	15.0	25.2	34.8	40.5	57.0

Anomaly Detection for Test Condition 2

Similar to the analysis for test condition 1, the initial $I_{CE(ON)}$ and $V_{CE(ON)}$ data at the mean aging temperature of $150^{o}C$ were used to compute healthy MD values.

The first 100 measurements corresponding approximately to 1 hour of aging time was used as healthy data.

The histogram of the healthy MD data for IGBT part "NPT3" is shown in Figure 4-6. The mean and standard deviation were found to be 6.6A, 0.018 and 2.1V, 0.014 respectively for I_{CE} and V_{CE} from the healthy data. From the figure, it is observed that 70% of the healthy MD values are < 1.

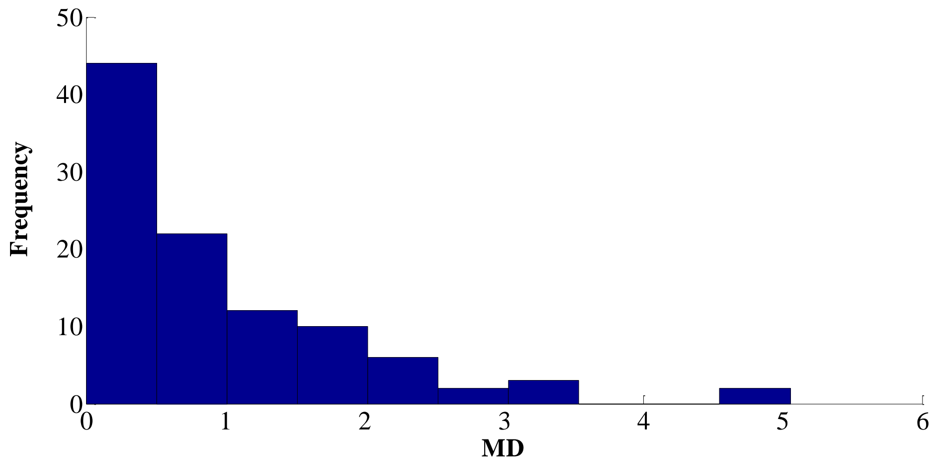

Figure 4-6: Histogram of the healthy MD values for IGBT "NPT3"

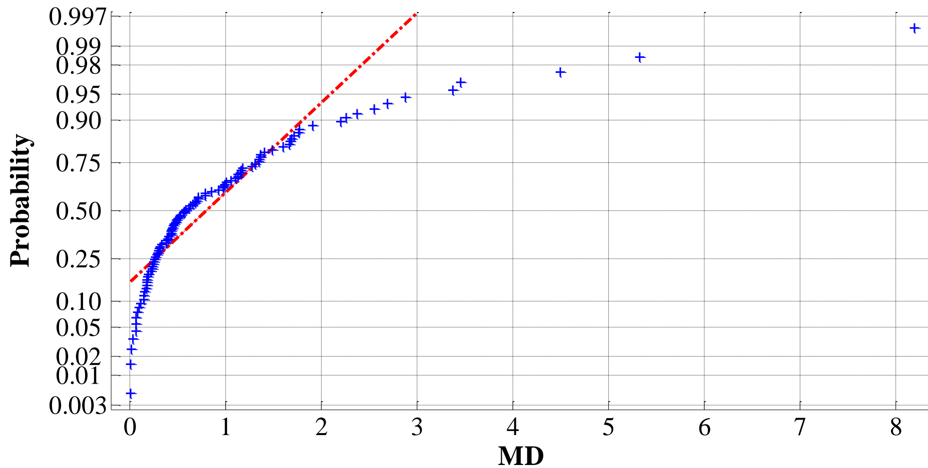

Figure 4-7: Normal probability plot of the healthy MD data for IGBT NPT3

After the Box-Cox transform, the transformed healthy MD data is observed to be approximately normally distributed as shown in the histogram in Figure 4-8 and the normal probability plot in Figure 4-9.

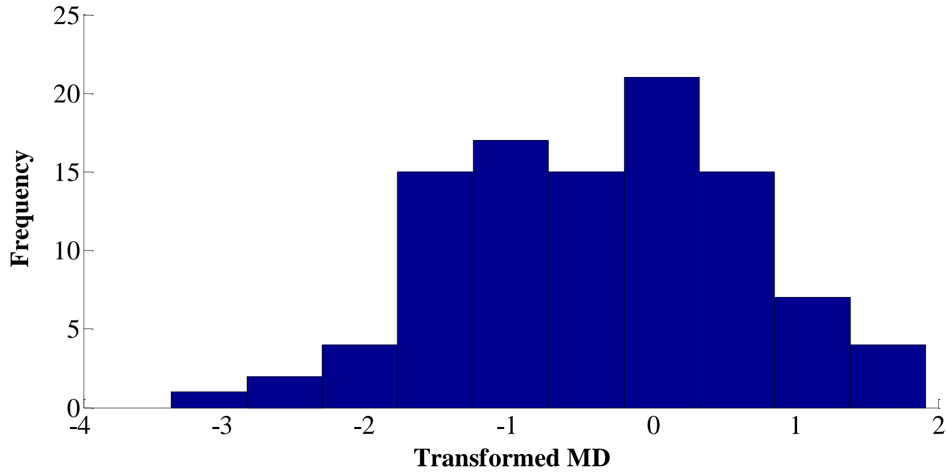

Figure 4-8: Transformed healthy MD data for IGBT NPT3

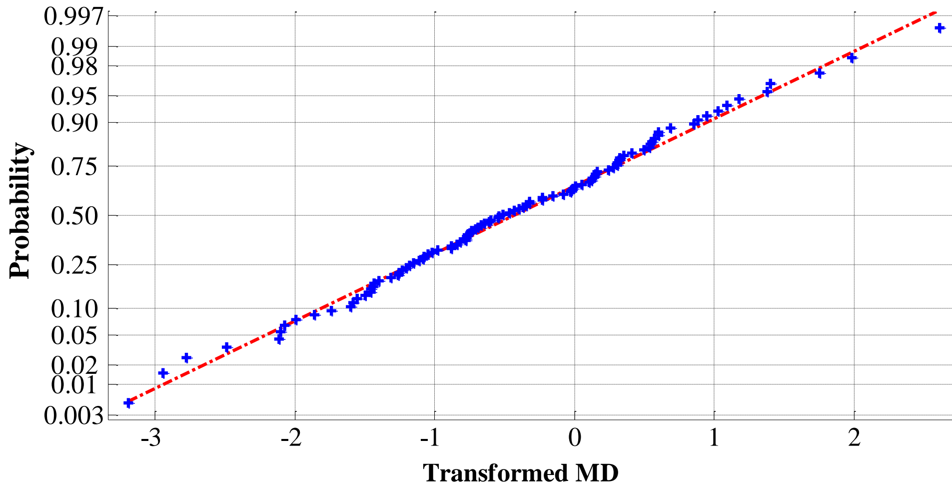

Figure 4-9: Normal probability plot of the transformed healthy MD data for IGBT NPT3

For IGBT part "NPT3" shown in Figure 4-10, the threshold was 2.7, the anomaly was detected at 4.4 hours, the time for parametric failure was 13.7 hours, and the functional failure was at 27 hours.

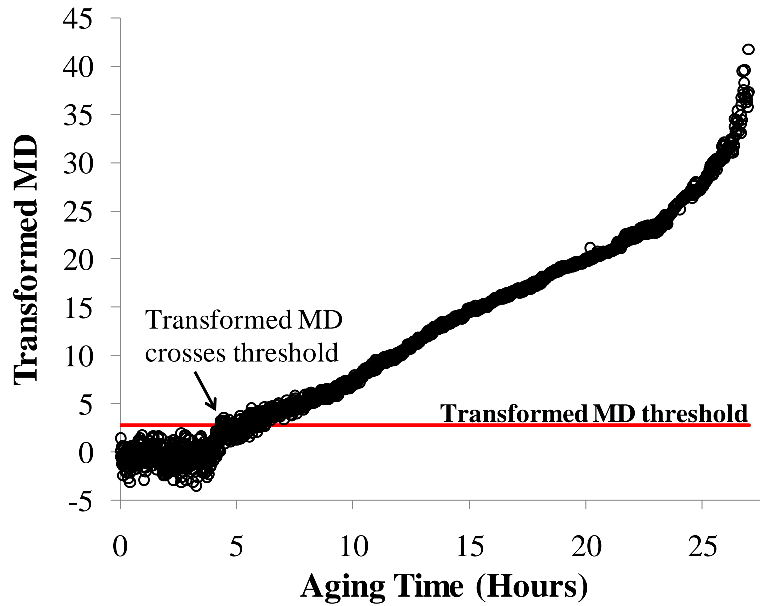

Figure 4-10: Transformed MD data vs. aging time for IGBT "NPT3"

The results of the MD anomaly detection approach for test condition 2 is summarized in Table 4-2. The anomalies were detected well in advance for all the parts both in terms of functional and parametric failure criteria.

Table 4-2: Anomaly detection times obtained for test condition 2

Device ID	**Detection time using transformed MD (Hours)**	**Time for 20% increase in $V_{CE(ON)}$ (Hours)**	**Failure time (Hours)**	**% Time to parametric failure after detection using transformed MD**	**% Time to functional failure after detection using transformed MD**
NPT1	3.6	9.0	19.2	60.3	81.5
NPT2	9.7	17.4	31.6	43.9	69.2
NPT3	4.4	13.5	27.0	67.8	83.9
NPT4	4.4	11.9	24.5	62.0	81.9
NPT5	5.6	8.8	12.3	36.5	54.5

Comparison of the MD Approach with a Fixed $V_{CE(ON)}$ Threshold for Anomaly Detection

A 5% change in $V_{CE(ON)}$ was used as a threshold for anomaly detection and compared with the MD approach. The transformed MD test and $V_{CE(ON)}$ data along with their respective thresholds for IGBT "N3" (test condition 1) are shown in Figure 4-11. The part failed due to latch-up at 49 minutes and anomalies in the device was detected at 12 minutes using the MD approach and 17 minutes using the $V_{CE(ON)}$ threshold.

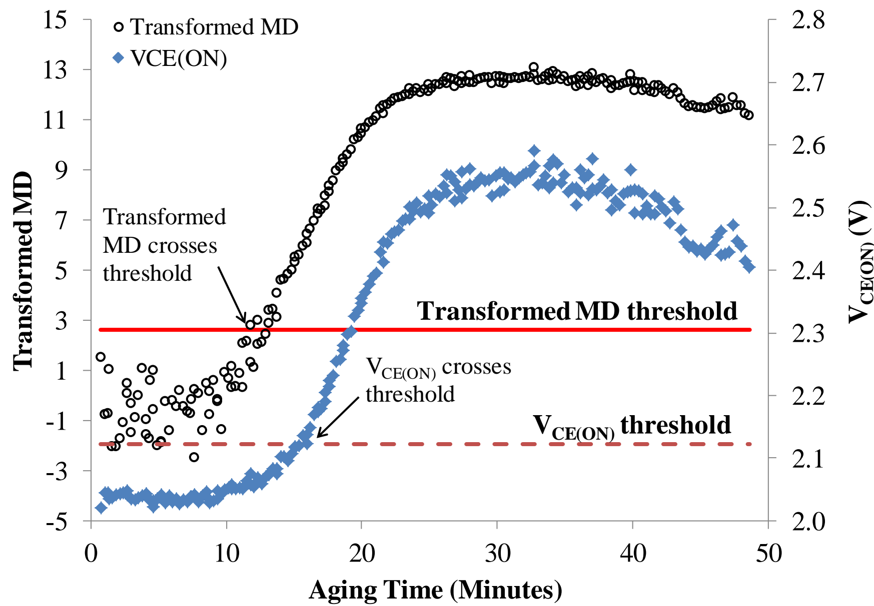

Figure 4-11: Comparison of transformed MD and fixed 5% $V_{CE(ON)}$ threshold for IGBT "N3"

In Table 4-3 and Table 4-4, the anomaly detection times obtained for test conditions 1 and 2 using the MD approach and fixed voltage threshold are compared. For test condition 1, the MD based approach was observed to provide earlier anomaly detection times in comparison to the 5% change in $V_{CE(ON)}$ threshold for seven of the

ten devices, two devices had the same detection time while for one device the 5% change in $V_{CE(ON)}$ threshold yielded an earlier detection time. For test condition 2, the MD approach provides an earlier detection time in comparison to the fixed threshold for all the devices evaluated.

Table 4-3: Detection time comparison for test condition 1

Device ID	Detection time using transformed MD (Minutes)	Time for 5% increase in $V_{ce(on)}$ (Minutes)	Failure time (Minutes)	% Time to failure after detection using transformed MD	% Time to failure after 5% increase in $V_{ce(on)}$
N1	13.8	17.8	47.1	70.8	62.3
N2	12.8	16.7	55.8	77.1	70.1
N3	11.8	16.5	48.7	75.8	66.2
N4	18.7	18.7	60.0	68.9	68.9
N5	11.4	17.1	39.4	71.0	56.5
N6	12.0	16.7	56.2	78.7	70.3
N7	16.2	17.4	42.6	62.0	59.2
N8	17.2	17.2	41.0	58.0	58.0
N9	14.6	8.0	54.8	73.3	85.3
N10	15.0	18.0	34.8	57.0	48.4

Table 4-4: Detection time comparison for test condition 2

Device ID	Detection time using transformed MD (Hours)	Time for 5% increase in $V_{CE(ON)}$ (Hours)	Failure time (Hours)	% Time to failure after detection using transformed MD	% Time to failure after 5% increase in $V_{ce(on)}$
NPT1	3.6	5.6	19.2	81.5	70.9
NPT2	9.7	11.9	31.6	69.2	62.3
NPT3	4.4	8.8	27.0	83.9	67.5
NPT4	4.4	6.0	24.5	81.9	75.5
NPT5	5.6	7.2	12.3	54.5	41.8

The anomaly detection times observed show that the MD approach that incorporates the degradation in $I_{CE(ON)}$ in addition to $V_{CE(ON)}$ is a better approach for anomaly detection compared to using a fixed percentage change of 5% in $V_{CE(ON)}$. It

is to be noted than using a percentage lower than 5% for the fixed threshold on the voltage may lead to equivalent or earlier detection times compared to the MD approach. However, determining the fixed threshold to be selected is typically based on the application conditions and expert judgment. The advantage of the MD approach is that the threshold is based on the healthy behavior of the device. Further, MD uses multivariate data for anomaly detection. The use of a multivariate data is known to provide better assessment of the health of the data when compared to the use of a single parameter. For example, there are situations in which measurements from a system may be within the thresholds of the individual parameters but are not part of the healthy space. In such situations, the MD approach detects the anomaly while the single parameter threshold is not able to do so.

Summary

NPT IGBTs were aged by power cycling under a resistive load until failure. The initial $I_{CE(ON)}$ and $V_{CE(ON)}$ parameters extracted at the mean aging temperature were used to compute the healthy MD distance. This health MD distance was transformed and the mean and standard deviation of the transformed MD data was obtained. The $\mu+3\sigma$ upper bound obtained from the transformed healthy MD was then used as a threshold for anomaly detection.

The MD based anomaly detection approach was able to detect anomalies before failure for all the devices evaluated for both test conditions. The anomaly detection times obtained in this analysis are used for initiating the particle filter algorithm to predict the remaining useful life of the devices as discussed in the next chapter.

Chapter 5. Prognostics

One of the most important goals of a prognostics and health management system is the prediction of remaining useful life (RUL). A particle filter based approach is one of the techniques that has been used to predict RUL. A particle filter based approach was used for the prognostics of a planetary gear plate [46]. In this approach, the system model was based on an empirical model for crack growth. The model constants were obtained by finite element analysis and data obtained from seeded fault tests. A sampling importance resampling (SIR) particle filter and an expectation-based long-term prediction generation approach were used for remaining useful life (RUL) estimation. Another particle filter approach has been used for battery prognostics [16]. A lumped parameter model was used to represent the batteries. The parameters of the model were extracted from sensor data collected from experiments using relevance vector machine regression. The system description model was then fed to the SIR particle filter for state estimation and RUL prediction.

Particle Filter: General Description

The particle filter (PF) is a sequential Monte Carlo method that has been used extensively in robotics, automation and artificial intelligence applications. It is a non-parametric approach to implementing the Bayes filter for state estimation. Estimation of dynamic states using system models and measurements are based on probabilistic laws that exercise the use of conditional independence and Markov property. The key idea of particle filters is that they represent distributions by a set of samples drawn

from the distribution, hence making the method non-parametric. This means that the representations are not limited to Gaussian distributions and can be used to represent more complex distributions such as multi-modal distributions. Another advantage provided by the particle filter's sample based representation is that it can model non-linear evolutions of system state in addition to linear state models.

The PF approach is a solution to the non-linear Bayesian tracking problem. The objective of tracking is to estimate the evolution of the system state x_k which is the state at time k based on control inputs $u_{1:k}$, and measurements $z_{1:k}$ which are the set of inputs and measurements obtained from time 1 to k respectively. In order to analyze the system, a model describing the evolution of the system state with time (and control inputs, if present) and a model relating the measurements to the system state known as the system model and the measurement model respectively are required in a probabilistic state-space formulation. The system state at time k is given by Equation (5.1) where f_k is the system model which is a function of the previous state, time and any control inputs as well as ω_k which is the system noise.

$$x_k = f_k(x_{k-1}, \omega_{k-1}) \tag{5.1}$$

The measurement at time k is related to the system state using the measurement equation as shown in Equation (5.2) where h_k is the measurement model and v_k is the measurement noise.

$$z_k = h_k(x_k, \nu_k) \tag{5.2}$$

The PF implementation consists of two recursive steps, prediction and update [48]. The prediction stage uses the knowledge of the previous state estimate and the system model to predict the current state estimate which is known as the prior probability density function (pdf) denoted as $p(x_k/x_{k-1})$. This is based on the Markov property that conditioned on the current system state, the future state is independent of the past states of the system. The update step uses the latest measurement to modify the prior pdf using the measurement model to obtain the updated system state known as the posterior pdf $p(x_k/z_k)$. This is achieved using Bayes theorem. In the PF approach, the system state pdf is approximated by a set of particles representing sampled values from the prior or posterior distributions, and a set of associated weights denoting discrete probability masses. The particles are generated based on an initial assumption of the system state pdf (at time $k=0$) and recursively estimated using the system model, measurement model and a set of available measurements [47].

Prognostics using particle filters is implemented by predicting future particle states without any additional measurement information. This is done by employing the prediction step repeatedly without the update step and using each predicted state as the posterior from which to derive the state at the next instant in time. The prediction step is repeated until the predicted value of the parameter under consideration crosses the failure threshold.

In this study, we implement a particle filter approach for prognostics of non punch through (NPT) IGBTs. As the PF requires models developed from known

system behavior (empirical models) as well as system measurements for state estimation, these were developed from the NPT IGBT test data.

To implement the particle filter the initial state of the system is represented by a set of particles x_0^i where $i=1,2,\ldots,n$ is the particle index, and n is the number of particles. The particles are then independently propagated using the system model as given by Equation (5.3), which provides the samples that represent the prior pdf.

$$x_k^i = f_k(x_{k-1}^i, \omega_{k-1}) \leftrightarrow p(x_k^i / x_{k-1}^i) \tag{5.3}$$

The posterior pdf of each particle is then calculated by first updating the associated particle weights using the measurement model which is the likelihood of measurement for each particle as shown in Equation (5.4) and Equation (5.5).

$$z_k^i = h_k(x_k^i, \nu_k) \leftrightarrow p(z_k / x_k^i) \tag{5.4}$$

$$w_k^i = w_{k-1}^i p(z_k \mid x_k^i) \tag{5.5}$$

After the weights are computed, they are normalized by Equation (5.6)

$$w_k^i = w_k^i / \sum_{i=1}^{n} w_k^i \tag{5.6}$$

The posterior pdf is then given by Equation (5.7)

$$p(x_k \mid z_{1:k}) \approx \sum_{i=1}^{n} w_k^i K\left(\frac{x_k - x_k^i}{h}\right) \tag{5.7}$$

where K is the kernel function and h is the bandwidth of the kernel function. One of the issues with the particle filter is particle degeneracy where after a few iterations most of the particles will have negligible weights. To avoid the effects of particle degeneracy, resampling is performed periodically. Particle degeneracy is evaluated by Equation (5.8).

$$\hat{n}_{eff} = 1 / \sum_{i=1}^{n} (w_k^i)^2 \tag{5.8}$$

If the number of effective particles calculated in Equation (5.8) is less than a threshold value, resampling is performed. The resampling process involves sampling with replacement wherein particles with low weights are replaced with a new set of particles drawn from the posterior pdf. The new set of particles is assigned uniform weights at the end of the resampling step as shown in Equation (5.9).

$$\{x_k^i, w_k^i\} \Leftrightarrow \{x_k^{i*}, 1/n\} \tag{5.9}$$

RUL Estimation for IGBTs

A system model was developed for the IGBTs based on the on-state collector-emitter voltage $V_{CE(ON)}$. A 2nd order least squares regression of the $V_{CE(ON)}$ degradation curve for two NPT IGBTs N1 and N2 for test condition 1 was obtained from the aging experiments. The system model obtained from the regression is given by Equation (5.10).

$$V_{CE(ON)k} = V_{CE(ON)k-1} + 2at_k(t_k - t_{k-1}) + b(t_k - t_{k-1}) + \omega_{k-1} \tag{5.10}$$

where *a* and *b* were model parameters from the least squares regression model. The parameters obtained for test condition 1 were *a=0.0015* and *b= -0.019*. The measurement model was the actual measured voltage given by

$$z_k = V_{CE(ON)k} + \nu_k \tag{5.11}$$

The system model obtained from the aging data was then used for RUL estimation of the remaining IGBT devices. The number of particles used was 30, the initial state was assumed to be Gaussian as the initial voltage values were found to be approximately normal based on the normal probability plot of the voltage values, and a threshold for resampling was set to 10. To estimate the process noise, the system model was used to estimate the $V_{CE(ON)}$ for IGBTs N1 and N2 for test condition 1. For each of the estimates, the residuals were obtained by calculating the difference between the estimates from the system model and the actual data from the aging experiments. The standard deviation of the residuals was then used as the standard deviation of the process noise which was assumed to be Gaussian. For test condition 1, the standard deviation of the process noise was found to be 0.025. The measurement noise was assumed to be Gaussian with a standard deviation of 0.05. The standard deviation of the measurement noise was obtained based on the noise of the voltage measurements performed by the oscilloscope.

For the purpose of RUL estimation, the system model was used with a 20% increase in the $V_{CE(ON)}$ as the failure threshold. In order to calculate the RUL from time of anomaly detection *k*, the prediction step of the particle filter was implemented without the weight update step. The predictions were calculated until the value of the

predicted $V_{CE(ON)}$ increased above the failure threshold. The remaining useful life estimate for the IGBT N3 evaluated at the detection time of 11.8 minutes was found to be 20.8 minutes while the actual failure occurred at 21.4 minutes resulting in a prediction error of 2.6%. The state estimation and prediction for IGBT "N3" is shown in Figure 5-1. It is observed that the mean of the state estimates, denoted by particle mean in Figure 5-1, tracks the measurements through the aging cycle of the IGBT until the detection of an anomaly by the MD approach. The RUL pdf is represented using a mixture of Gaussians of the particle distribution at the predicted failure time.

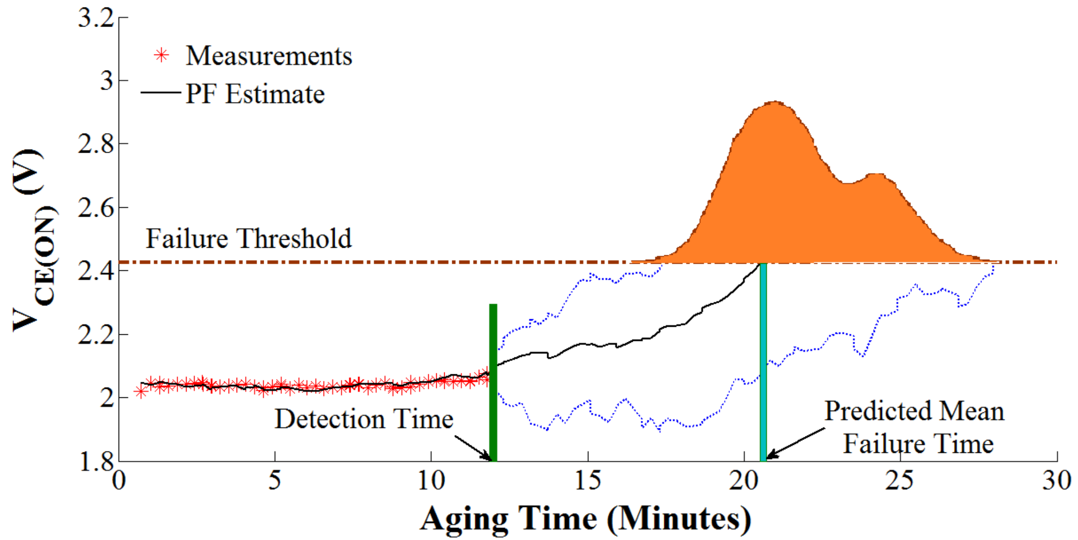

Figure 5-1: State estimation and RUL prediction of IGBT "N3"

The RUL estimates from the implementation of the particle filter for the eight IGBTs aged under test condition 1 are summarized in Table 5-1. From the results, it is observed that the prediction error is < 10% for seven of the eight IGBTs analyzed.

Table 5-1: RUL prediction for IGBTs in test condition 1

Device ID	Anomaly Detection time using transformed MD (Minutes)	Predicted Time for 20% increase in $V_{CE(ON)}$ (Minutes)	Time for 20% increase in $V_{CE(ON)}$ (Minutes)	% Prediction Error
N3	11.8	20.8	21.4	2.6
N4	18.7	24.4	23.6	-3.3
N5	11.4	22.6	23.1	2.2
N6	12.0	22.4	21.5	-4.2
N7	16.2	23.9	22.4	-6.8
N8	17.2	23.5	24.6	4.6
N9	14.6	20.7	24.8	16.3
N10	15.0	24.3	25.2	3.5

A similar analysis was performed for IGBTs aged under test condition 2. The model parameters obtained from the least squares regression for IGBTs NPT 1 and NPT 2 were found to be $a=0.005$ and $b=-0.027$. The system tracking performance and RUL estimate of the particle filter for IGBT NPT 3 is shown in Figure 5-2 . The RUL predictions for IGBTs aged under test condition 2 are summarized in Table 5-2.

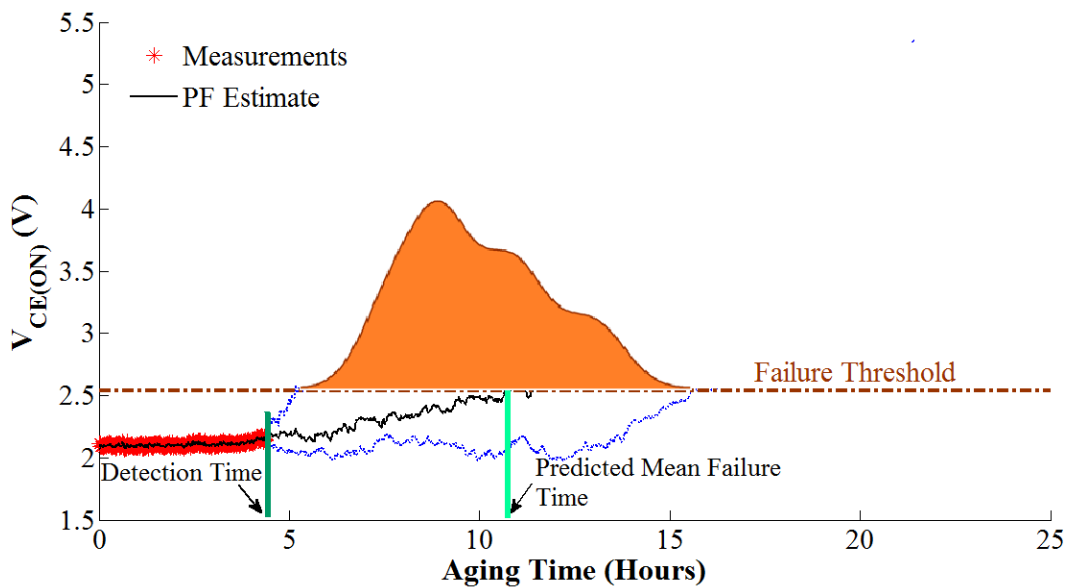

Figure 5-2: State estimation and RUL prediction of IGBT “NPT3”

Table 5-2: RUL prediction for IGBTs in test condition 2

Device ID	Anomaly Detection time using transformed MD (Hours)	Predicted Time for 20% increase in $V_{CE(ON)}$ (Hours)	Time for 20% increase in $V_{CE(ON)}$ (Hours)	% Prediction Error
NPT3	4.4	10.6	13.5	21.5
NPT4	4.4	10.0	11.9	15.7
NPT5	5.6	8.9	8.8	-1.1

Computational Complexity

The particle filter algorithm involves filtering (prediction and weight update steps) followed by resampling whenever particle degeneracy is encountered. The prediction step involves calculating the state x_k of each particle at time k based on the system model $p(x_k/x_{k-1})$. The weight update for each particle is based on calculating the probability of measurement z_k at time k given the predicted state of the particle $p(z_k/x_k)$. In this implementation, the state x_k is a scalar quantity ($V_{CE(ON)}$). These steps are performed N (where N is the number of particles) times to get the predicted particles and their respective weights. The computational complexity for the prediction and weight update steps is $O(N+1)$ (one additional step is required to terminate the FOR loop). The resampling step involves generating N independent samples from the uniform distribution $U(0,1)$, sorting them in ascending order and comparing them with the cumulative sum of the weights. In this step, the computational complexity is determined by the sorting algorithm which is of the order of $O(N \log N)$. Hence the driving "n" for the computational complexity of the

particle filter algorithm is *O(N log N)*. With an increase in the number of particles used, the computational complexity increases as shown in Figure 5-3.

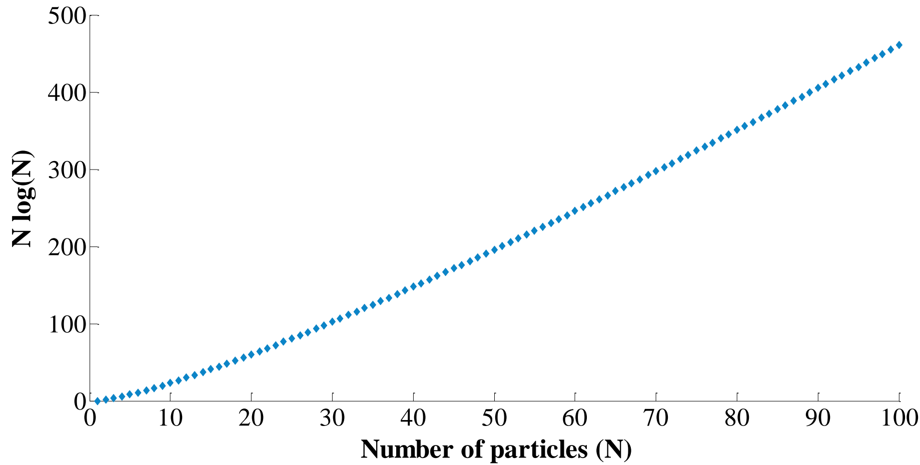

Figure 5-3: Computational complexity of the particle filter as a function of the number of particles

<u>*Effect of Number of Particles on Failure Prediction*</u>

To illustrate the effect of increasing the number of particles on the particle filter prediction, the number of particles was increased from 10, 30, 100 to 300. The predictions were performed at four different times: 3, 6, 12 and 18 minutes. The analysis was performed on IGBTs N3 to N10. The results for N3 are presented from Figure 5-4 to Figure 5-19. The results for all the other parts are listed in the Appendix C.

In each figure, the "green" line represents the time at which the particle filter prediction is performed, the "cyan" line is the predicted mean time to failure obtained by the particle filter and the "red" line is the actual failure time determined from the test.

Predictions for N=10, 30,100 and 300 at 3 minutes

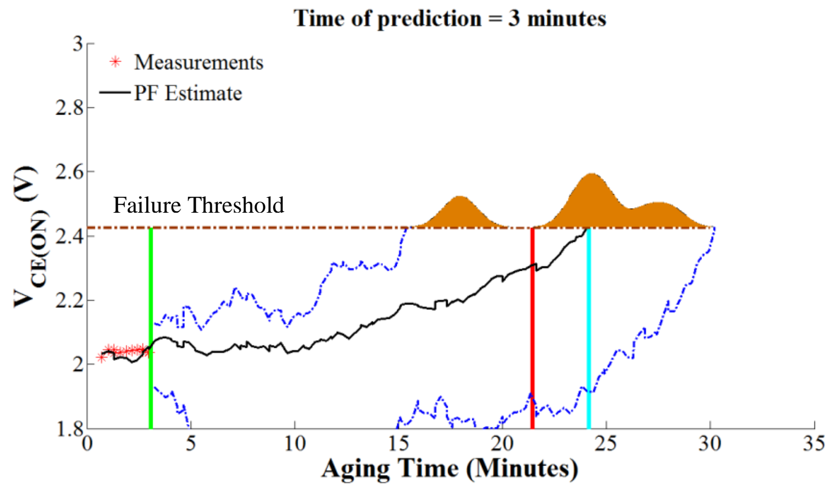

Figure 5-4: Prediction for N= 10 particles and time t= 3minutes

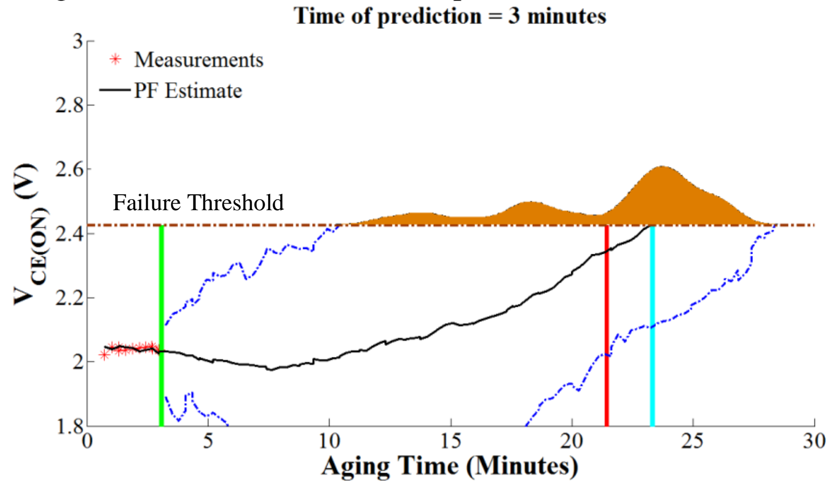

Figure 5-5: Prediction for N= 30 particles and time t= 3 minutes

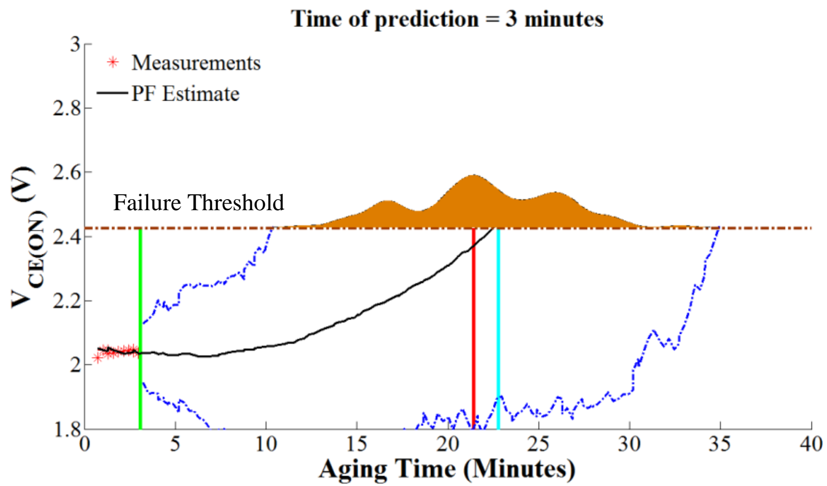

Figure 5-6: Prediction for N= 100 particles and time t= 3 minutes

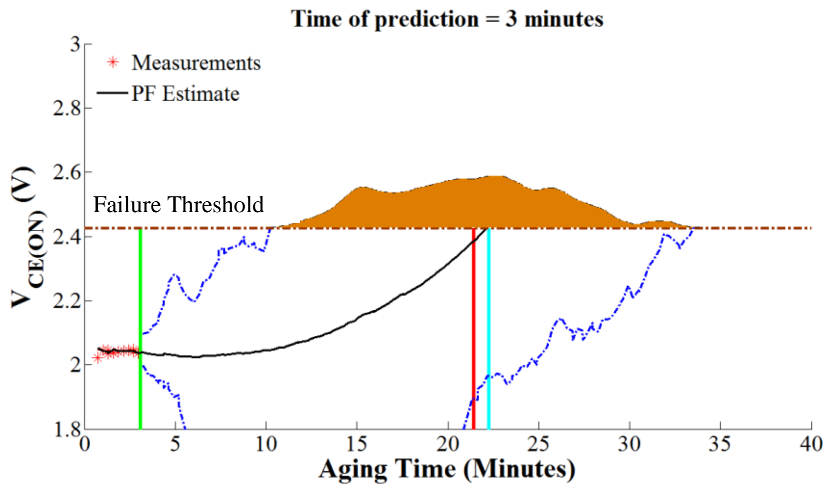

Figure 5-7: Prediction for N= 300 particles and time t= 3 minutes

Predictions for N=10, 30,100 and 300 at 6 minutes

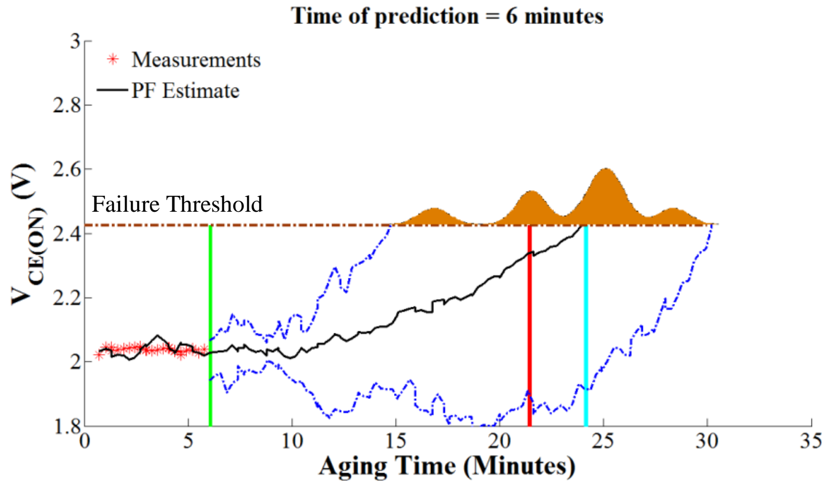

Figure 5-8: Prediction for N= 10 particles and time t= 6 minutes

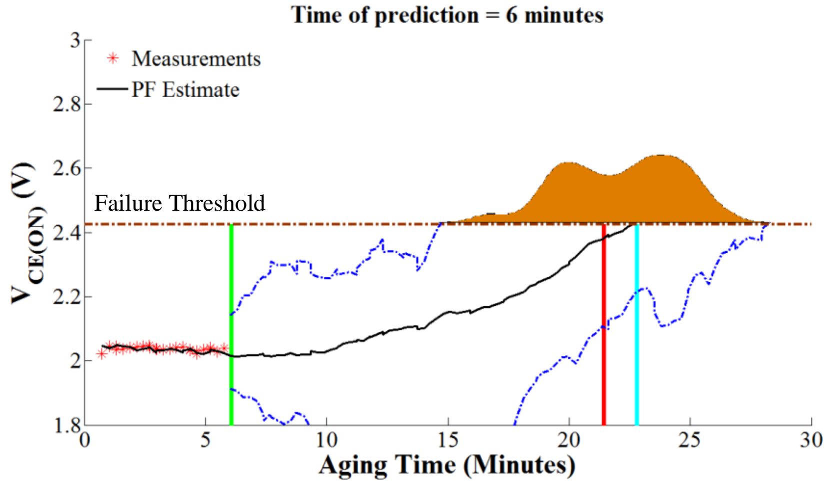

Figure 5-9: Prediction for N= 30 particles and time t= 6 minutes

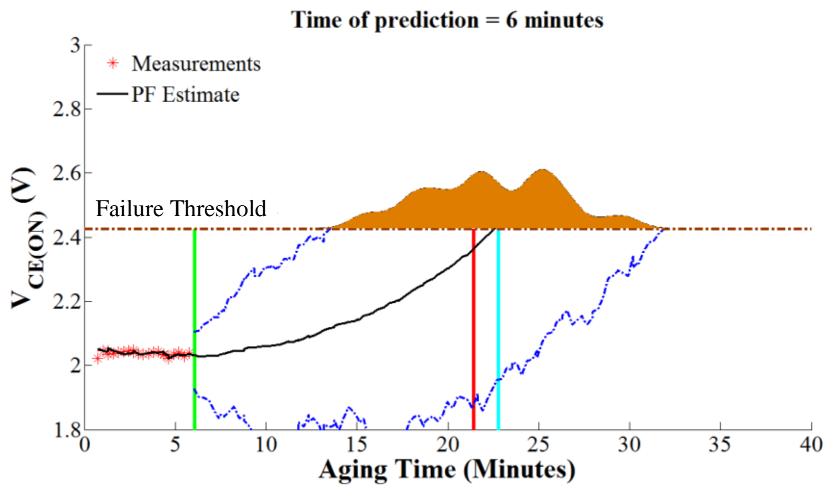

Figure 5-10: Prediction for N= 100 particles and time t= 6 minutes

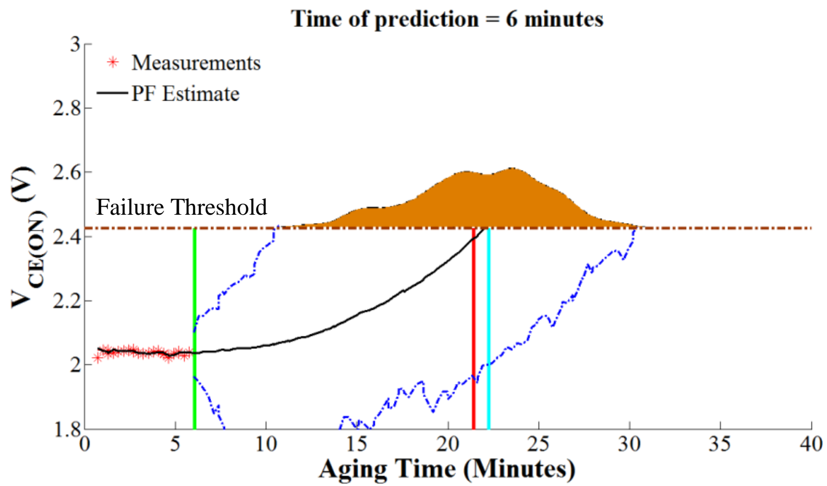

Figure 5-11: Prediction for N= 300 particles and time t= 6 minutes

Predictions for N=10, 30,100 and 300 at 12 minutes

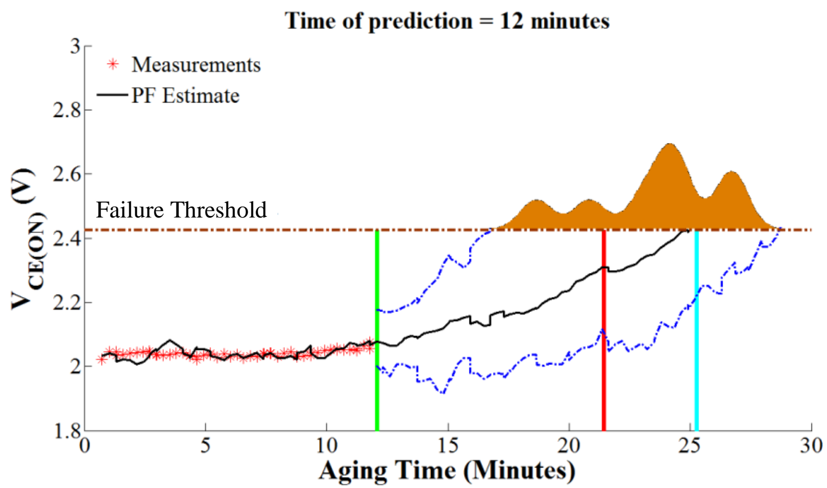

Figure 5-12: Prediction for N= 10 particles and time t= 12 minutes

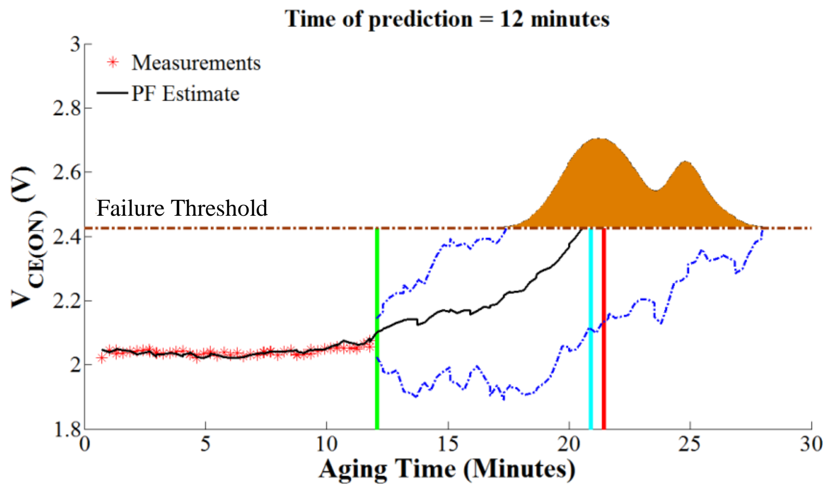

Figure 5-13: Prediction for N= 30 particles and time t= 12 minutes

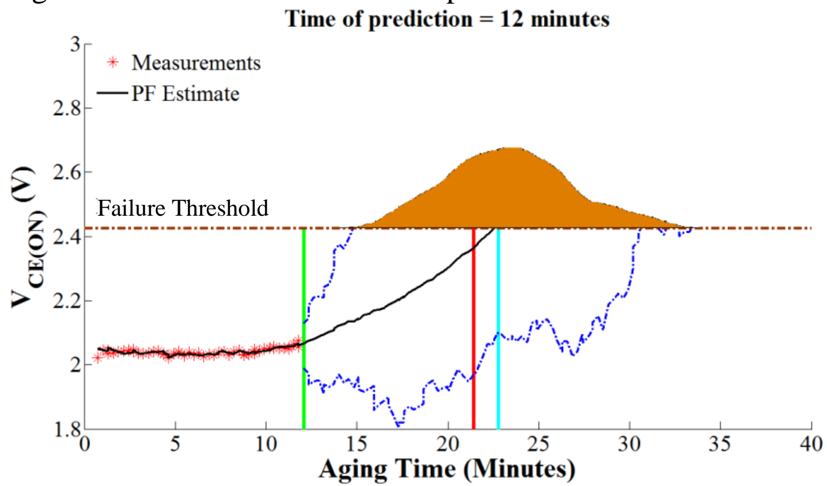

Figure 5-14: Prediction for N= 100 particles and time t= 12 minutes

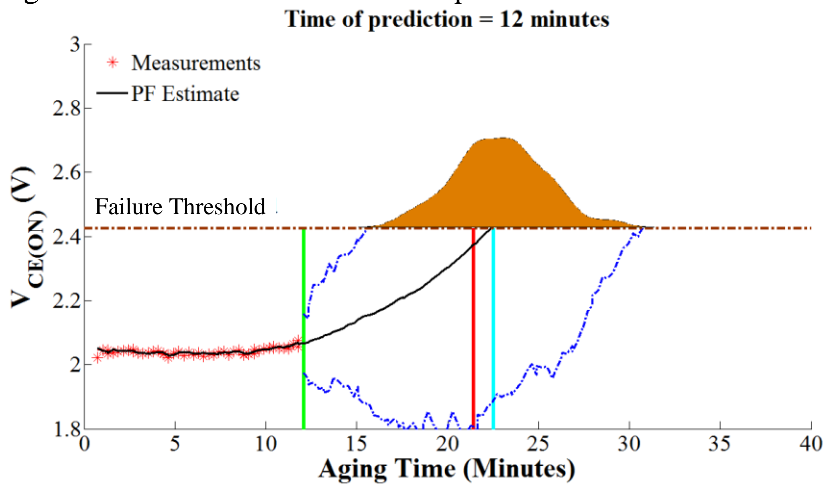

Figure 5-15: Prediction for N= 300 particles and time t= 12 minutes

Predictions for N=10, 30,100 and 300 at 18 minutes

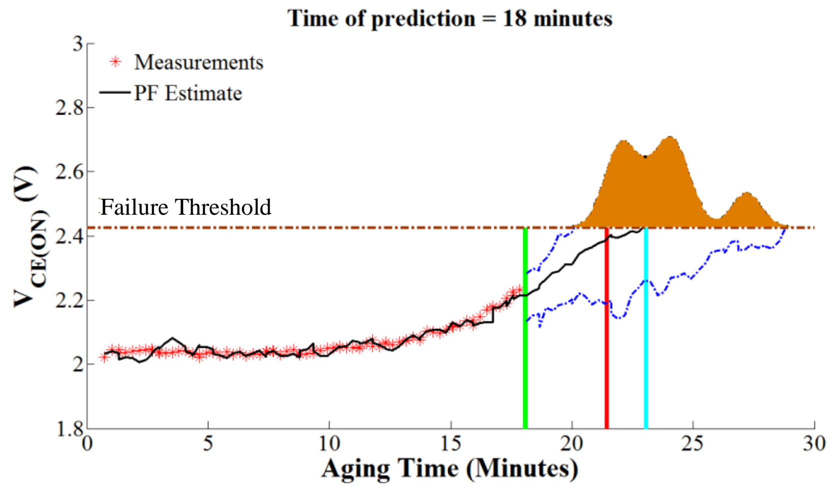

Figure 5-16: Prediction for N= 10 particles and time t= 18 minutes

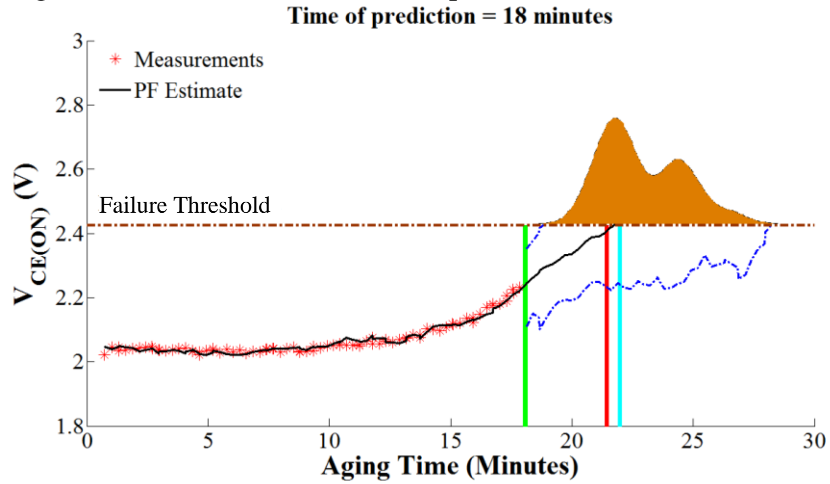

Figure 5-17: Prediction for N= 30 particles and time t= 18 minutes

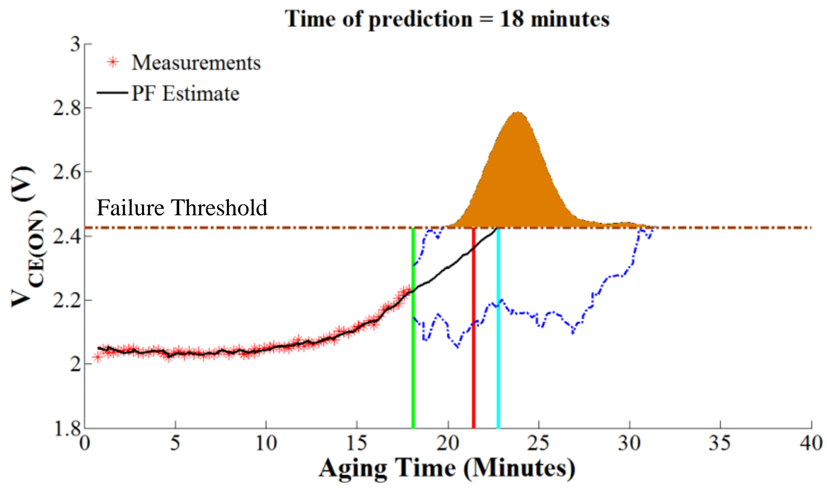

Figure 5-18: Prediction for N= 100 particles and time t= 18 minutes

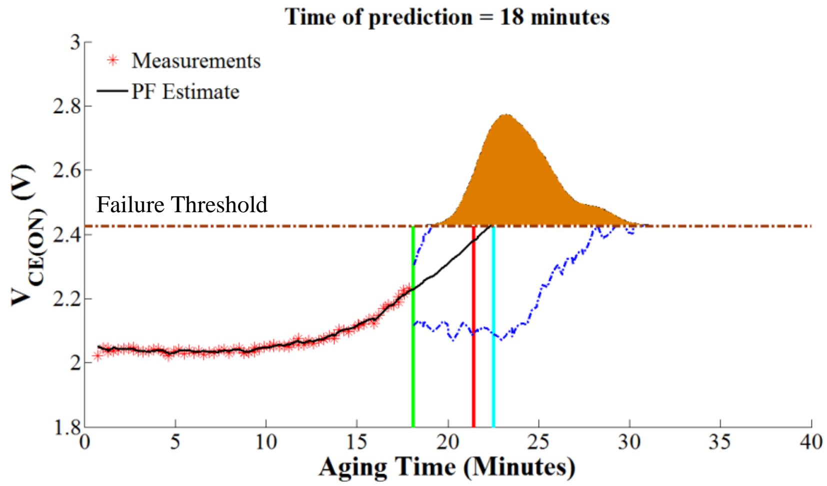

Figure 5-19: Prediction for N= 300 particles and time t= 18 minutes

Table 5-3: Effect of particle size on failure prediction time for IGBT N3 (Actual Failure=21.4 minutes)

Time of Prediction	**No of particles**	**Predicted Failure Time**		
		T_{lower}(minutes)	**T_{mean}(minutes)**	**T_{upper}(minutes)**
3 Minutes	10	15.7	24.1	30.2
	30	10.4	23.3	28.5
	100	10.4	22.7	35.0
	300	10.4	22.2	33.6
6 Minutes	10	14.8	24.1	30.2
	30	14.8	22.7	28.3
	100	13.7	22.7	35.0
	300	10.7	22.2	30.5
12 Minutes	10	16.7	25.2	28.8
	30	17.6	20.8	28.0
	100	14.8	22.7	33.6
	300	15.7	22.4	32.7
18 Minutes	10	20.3	23.0	28.8
	30	18.9	21.9	28.3
	100	19.7	22.7	31.3
	300	19.2	22.4	32.2

From this analysis, it is clearly observed that 10 particles are not sufficient to adequately represent the system state, especially when the prediction is performed at 3 minutes and 6 minutes. However, due to the smaller number of particles, the predicted failure PDF has a lower variance. As shown in Figure 5-4 to Figure 5-7 and Table 5-3, when the particle filter is used for prediction after an aging time of 3 minutes, an increase in the number of particles causes a wider distribution for the failure PDF. The lower bound for the failure PDF for 100 and 300 particles provides a more conservative estimate of the failure time.

When the predictions are performed after 6 minutes of aging (Figure 5-8 to Figure 5-11 and Table 5-3), the mean predicted failure times with 30, 100 and 300 particles have negligible differences. However, the lower bound of the failure

prediction continues to provide a conservative estimate of the failure. This is especially true for 300 particles. After 12 minutes of aging (Figure 5-12 to Figure 5-15 and Table 5-3), the failure PDFs are narrower providing more confidence in the failure prediction. The predictions performed with 30 particles are the most accurate.

From Table 5-3 and the results for the other parts documented in the Appendix C, we observe that with 30, 100 or 300 particles, there is no significant change in the mean predicted failure time. With an increase in the number of particles, the peak of the failure distribution PDF is observed to shift to the actual failure time. However, the lower bound of the failure prediction is very conservative for predictions performed at 3 minutes and 6 minutes. This illustrates the case that initiating the particle filter for prediction too early results in larger distribution for the failure PDF. With 30 particles, one can obtain a reasonable representation of the system state without loss of accuracy in term of failure prediction time.

From the analysis presented in Figure 5-4 to Figure 5-19, it is observed that the failure probability distribution narrows with time. At the particle filter prediction step, say t_p, the developed system model is used to predict future states at times t_{p+1}, t_{p+2} and so on until the predicted voltage crosses the failure threshold. After each prediction, the system noise adds up. Hence a prediction performed in the initial stages for a given particle size will have a wide distribution. For the prediction using 100 particles at 3 minutes and 18 minutes (by comparing Figure 5-6 and Figure 5-18), we observe that PDF distribution narrows from 25 minutes to 12 minutes.

Effect of Increased Number of Parts in Development of System Model

The number of parts used to develop the system model was increased to 3, 4 and 5 from the 2 parts used in the initial analysis. This analysis was performed for test condition 1. The system model consists of two coefficients "a" and "b" and the standard deviation system noise parameter σ_{ω}. In Table 5-4, the coefficients obtained using 2(N1, N2), 3 (N1, N2, N3), 4 (N1, N2, N3, N4) and 5 (N1, N2, N3, N4, N5) parts is shown. The system model was used in a particle filter algorithm to determine the mean predicted time to failure for the IGBTs "N6 to N10" at the time of anomaly detection by the MD approach. The results of the analysis are given in Table 5-5. The prediction times do not change significantly with an increase in the number of parts. From this analysis, we can conclude that using more than two parts for the system model for test condition 1 does not provide improvements in the failure prediction time. However, the time to failure PDFs change with the inclusion of more parts in the system model as shown in Figure 5-20, Figure 5-21 and Figure 5-22.

Table 5-4: System model parameters

No of Parts	**A**	**b**	σ_{ω}
2	0.00149	-0.01867	0.0254
3	0.00159	-0.02044	0.0221
4	0.00158	-0.02120	0.0254
5	0.00157	-0.02099	0.0234

Table 5-5: Mean time to failure prediction using particle filters for the four system models

Device ID	Predicted mean time to failure (2 parts) (Minutes)	Predicted mean time to failure (3 parts) (Minutes)	Predicted mean time to failure (4 parts) (Minutes)	Predicted mean time to failure (5 parts) (Minutes)	Failure Time (Minutes)
N6	22.4	22.7	22.7	22.7	21.5
N7	23.9	23.3	23.3	23.9	22.4
N8	23.5	23.7	24.9	24.0	24.6
N9	20.7	21.0	21.9	20.7	24.8
N10	24.3	24.0	24.3	23.7	25.2

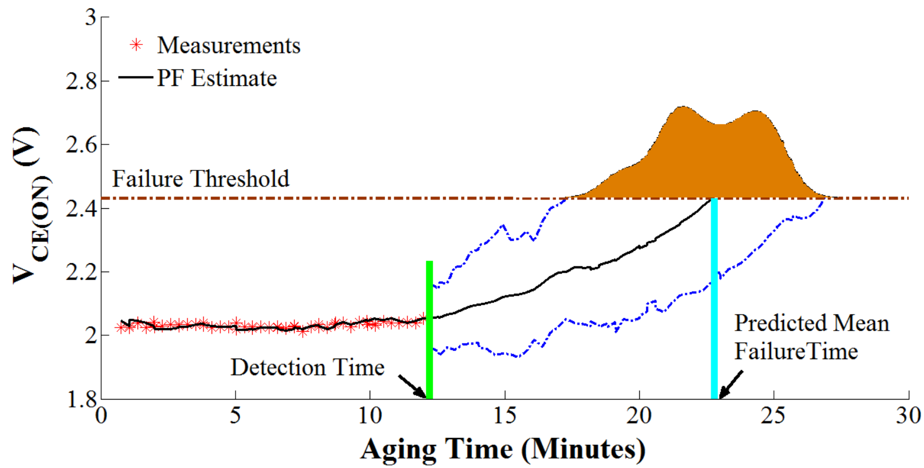

Figure 5-20: Failure prediction for part N6 using three part system model

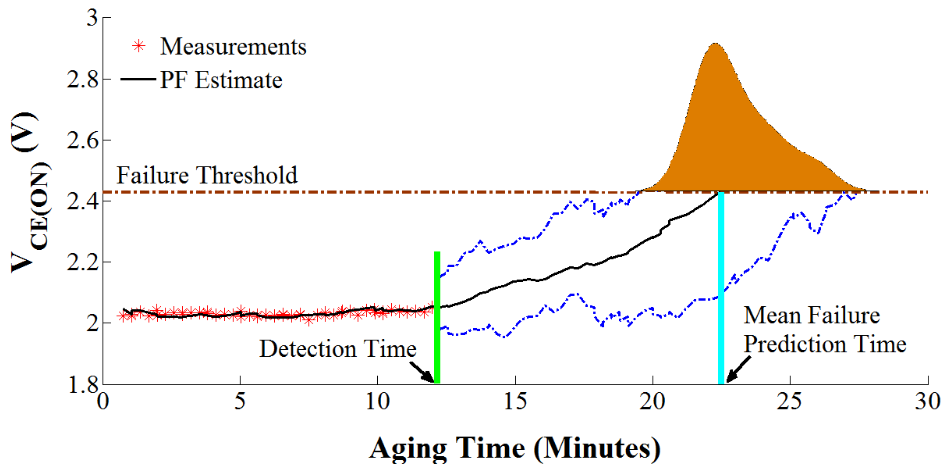

Figure 5-21: Failure prediction for part N6 using four part system model

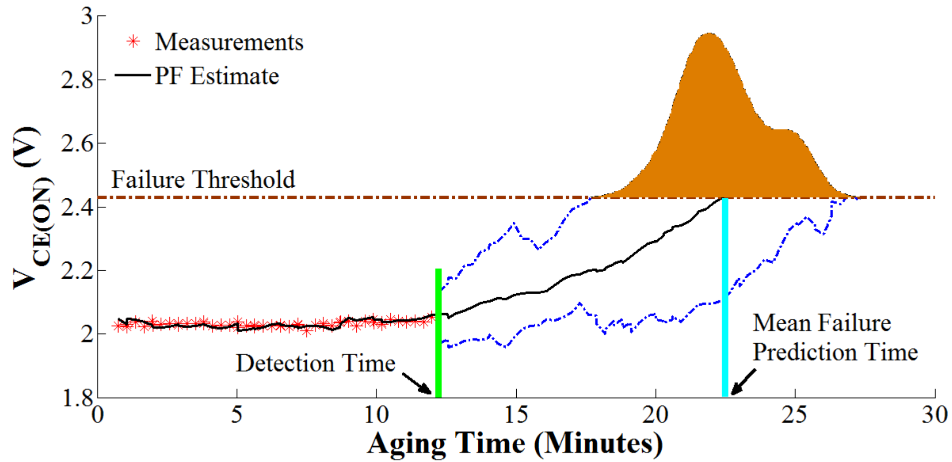

Figure 5-22: Failure prediction for part N6 using five part system model

Effect of Number of Particles on the Confidence of the Failure Prediction Distribution

To determine the effect of increasing number of particles on the confidence of the prediction PDF, the upper, mean and lower prediction times for parts N3 to N10 are given in Table 5-6 for N=10, 30,100 and 300 particles at time t=12 minutes. With an increase in the number of particles used for prediction, the variance associated with the prediction increases. As illustrated by Table 5-6, the failure distribution widens with increase in the number of particles.

Table 5-6: Effect of particle size on predicted failure distribution (time of prediction = 12 minutes)

Device	**No of particles**	**Predicted Failure Time**			**T_{upper} - T_{lower} (minutes)**
		T_{lower}(minutes)	**T_{mean}(minutes)**	**T_{upper}(minutes)**	
N3	10	16.7	25.2	28.8	12.1
	30	17.6	20.8	28.0	10.4
	100	14.8	22.7	33.6	18.8
	300	15.7	22.4	32.7	17.1
N4	10	18.9	23.6	28.5	9.5
	30	16.5	21.9	30.4	14.0
	100	17.0	22.5	29.9	12.9
	300	16.2	23.0	32.4	16.2
N5	10	17.4	26.1	28.9	11.5
	30	18.8	22.6	27.5	8.6
	100	14.8	23.7	34.2	19.4
	300	15.1	23.1	32.8	17.6
N6	10	18.8	26.6	30.3	11.5
	30	16.4	22.4	27.6	11.2
	100	15.2	23.6	33.1	17.9
	300	15.8	23.0	31.6	15.8
N7	10	17.7	24.2	31.6	13.9
	30	18.0	23.0	26.9	8.9
	100	16.2	22.7	32.5	16.3
	300	17.1	22.7	32.2	15.1
N8	10	20.9	26.0	29.2	8.3
	30	15.8	22.0	26.9	11.1
	100	14.6	22.3	33.6	18.9
	300	15.2	22.0	31.7	16.5
N9	10	20.2	24.5	28.4	8.2
	30	14.6	21.3	27.2	12.5
	100	14.3	22.4	32.6	18.2
	300	13.7	21.6	32.3	18.5
N10	10	22.8	24.3	31.9	9.1
	30	17.4	24.0	28.5	11.1
	100	17.7	24.0	32.2	14.5
	300	16.7	23.7	31.9	15.1

Implementation of the Particle Filter using $I_{CE(ON)}$

The particle filter algorithm was implemented using the $I_{CE(ON)}$ measurements for test condition 1. The system model was developed by using a least squares regression of the $I_{CE(ON)}$ data for IGBTs N1 and N2. The coefficients obtained by the regression were a = -0.0067 and b = 0.085. The standard deviation of the system noise was 0.1. The failure time was the time required for the $V_{CE(ON)}$ to increase by 20%. The predicted mean time to failure using the $I_{CE(ON)}$ was computed for N3 as shown in Figure 5-23. The $I_{CE(ON)}$ parameter gives equivalent prediction results to the $V_{CE(ON)}$ and as such either parameter can be used for the particle filter prediction. However, as the failure criteria are typically defined based on the change in $V_{CE(ON)}$, the $V_{CE(ON)}$ parameter was selected for prediction by particle filters in this study.

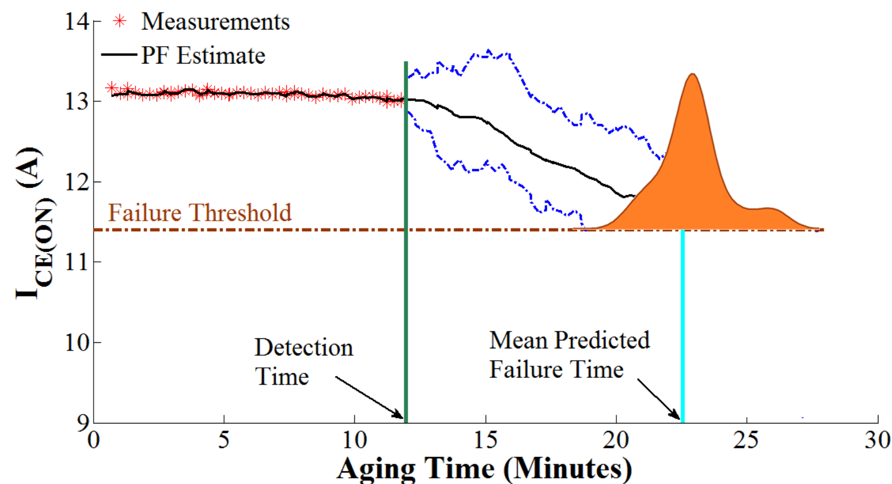

Figure 5-23: Particle filter prediction using $I_{CE(ON)}$ for part "N3"

Summary

In this study, a particle filter approach was used for the prognostics of IGBTs. A system model was developed using the degradation trend of the on-state collector-

emitter voltage $V_{CE(ON)}$ parameter. This was obtained by a least squares regression of the IGBT degradation curve. The tracking and prediction performance of the model with the particle filter was demonstrated. The prediction error ranged from 1 to 20% when prediction was performed at the anomaly detection time provided by the MD approach.

This study demonstrates that the use of the Mahalanobis distance (MD) for anomaly detection and the particle filter approach using either the $V_{CE(ON)}$ or $I_{CE(ON)}$ parameters provides accurate estimation of the remaining useful life of NPT IGBTs. The prognostics approach proposed is not specific to the non-punch through (NPT) IGBT investigated in this dissertation. It is also applicable to the other two main IGBT technologies: field stop (FS) and punch-through (PT). This is due to the fact that the degradation of the die attach with power cycling stresses will result in changes in the $V_{CE(ON)}$ as well as $I_{CE(ON)}$ for all IGBT technologies. However, the patterns of degradation are going to be different depending on the technology. For example, the degradation of the die attach will result in an increase in the $V_{CE(ON)}$ for the field stop IGBT, but the increase will not be of the same magnitude as it is for the NPT IGBT because the field stop layer reduces the $V_{CE(ON)}$ by conductivity modulation. For a given IGBT technology, the degradation trends are also going to change with changes in the part family.

For implementing this approach on a different IGBT, aging tests will need to be performed to develop the system model for the $V_{CE(ON)}$ degradation curve. Other costs involved will include sensors and data acquisition systems to perform in-situ monitoring of the required device parameters. Some efforts will also be required to

obtain the optimum size of the healthy data for anomaly detection by MD as well as tuning the particle filter model.

To implement the particle filter approach in fielded systems, IGBTs will need to be tested under suitable life cycle conditions to determine the degradation trend in the $V_{CE(ON)}$ in order to develop the system model. Improvements in RUL estimation can be achieved by the accurate estimation of the system and measurement noise, optimization of the number of particles and the resampling threshold.

Chapter 6. Contributions and Future Work

The main contribution of this study is the development and implementation of a prognostics framework for IGBTs that uses the Mahalanobis distance approach for anomaly detection and particle filters for failure prediction. The particle filter approach developed using the system model based on the $V_{CE(ON)}$ was demonstrated to provides estimates of IGBT remaining useful life with an error of $< 20\%$ at the time of anomaly detection .

The MD based probabilistic threshold approach implemented in this work was successfully able to detect anomalies in the IGBTs before either parametric failure or functional failure for both the test conditions evaluated.

The $V_{CE(ON)}$ and $I_{CE(ON)}$ parameters were identified as precursors to IGBT failure. The degradation in these parameters was mapped to degradation in the devices by electrical characterization tests and X-ray analysis. It was determined that die attach degradation as well as degradation in the gate oxide contributed to the changes observed in the precursor parameters with aging.

The implementation of the developed prognostics framework can help provide advance warning of failures thereby preventing costly IGBT failures and system downtime.

Future Work

Further research is needed to implement the developed prognostics approach in a real world application. The degradation trend of the $V_{CE(ON)}$ is technology

dependent, i.e., it varies for punch through, non-punch through and field stop IGBTs. Additionally, the trends will be different for different classes of IGBTs within the same technology. Hence, to develop the system model, one would need to perform accelerated aging tests for each new class of IGBT. One possible solution to this problem would be to update the system model parameters for each new class of IGBT as more information from the new IGBT is obtained. The model parameters could be updated by reducing the error obtained by the difference between the voltage predicted by the system model and the actual measured voltage of the new IGBT.

Since the system model is developed for a fixed temperature, the $V_{CE(ON)}$ will need to be measured in application at the temperature used to obtain the system model. One method of resolving this issue would be to determine a temperature dependent correction parameter for the $V_{CE(ON)}$ system model to account for changes in temperature.

Appendix A

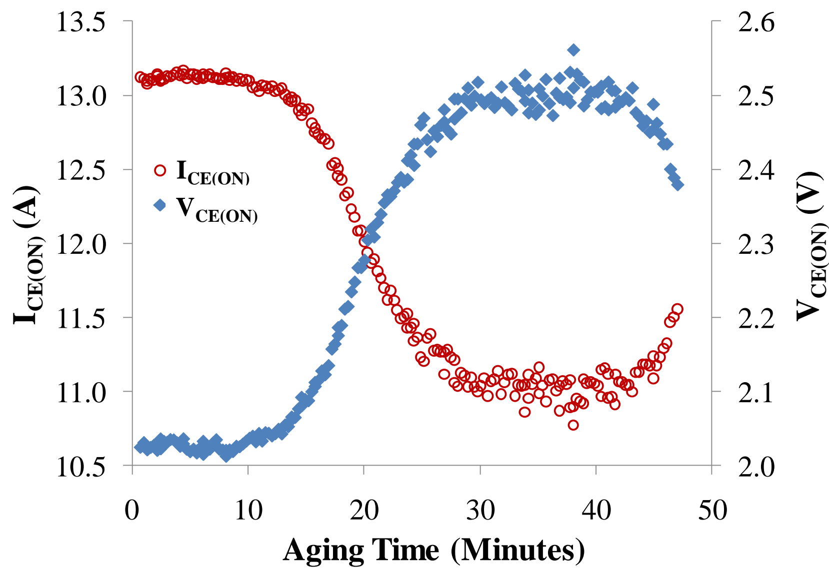

Figure 6-1: $I_{CE(ON)}$ and $V_{CE(ON)}$ vs. aging time for "N1" aged by test condition 1

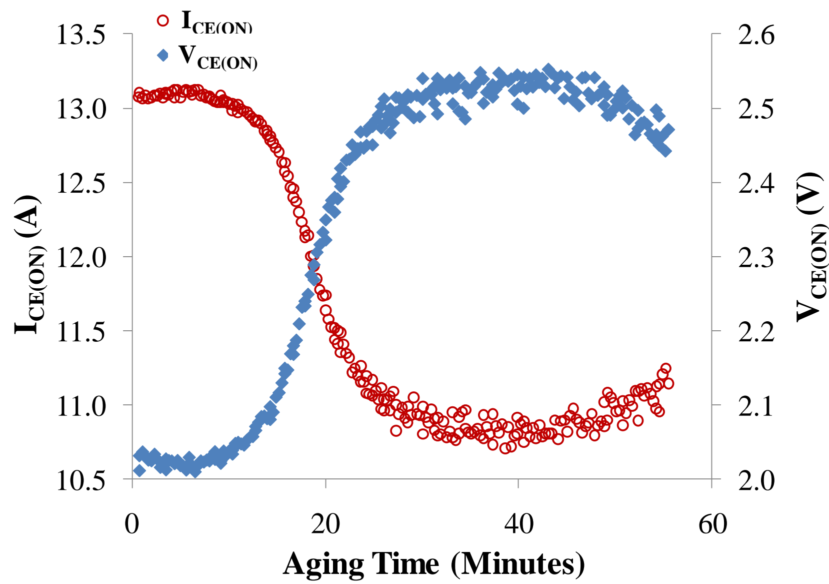

Figure 6-2: $I_{CE(ON)}$ and $V_{CE(ON)}$ vs. aging time for "N2" aged by test condition 1

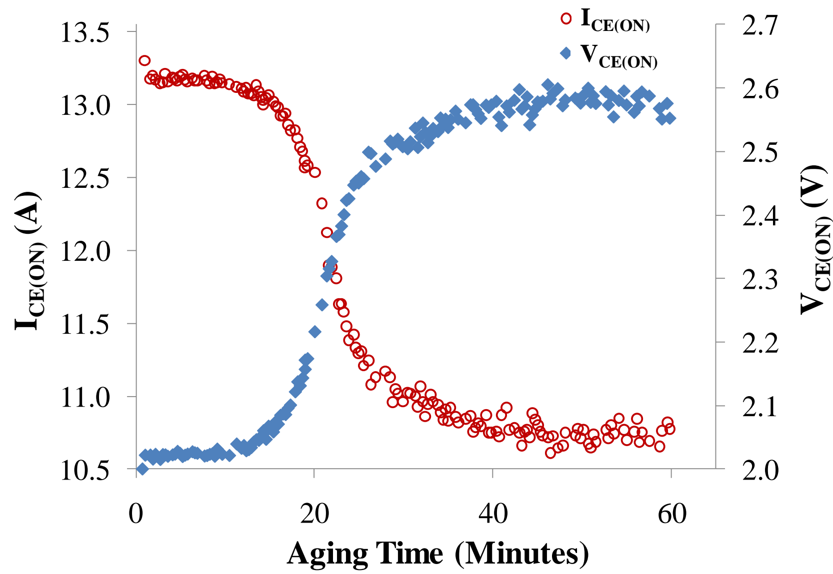

Figure 6-3: $I_{CE(ON)}$ and $V_{CE(ON)}$ vs. aging time for “N4” aged by test condition 1

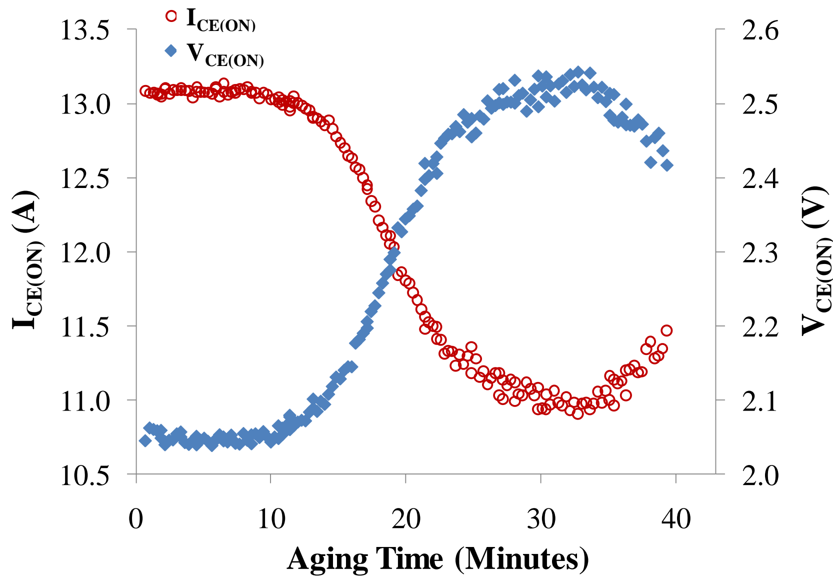

Figure 6-4: $I_{CE(ON)}$ and $V_{CE(ON)}$ vs. aging time for “N5” aged by test condition 1

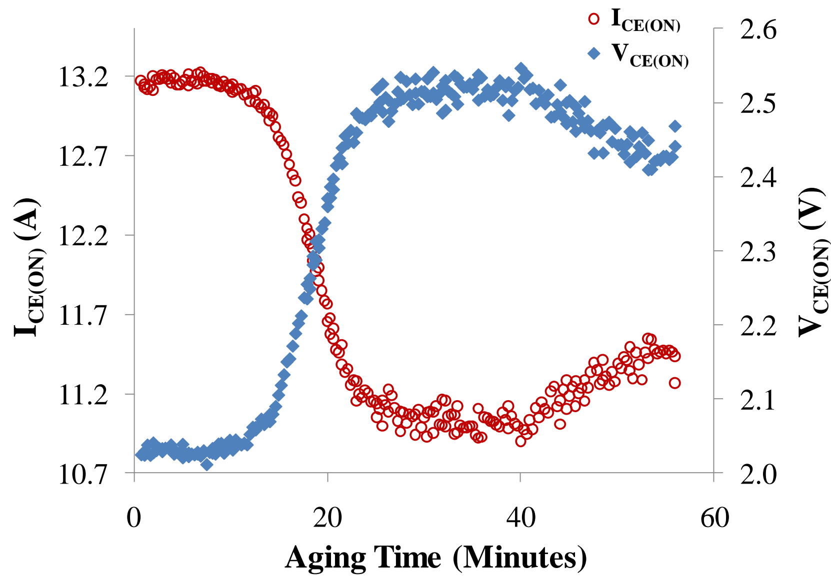

Figure 6-5: $I_{CE(ON)}$ and $V_{CE(ON)}$ vs. aging time for “N6” aged by test condition 1

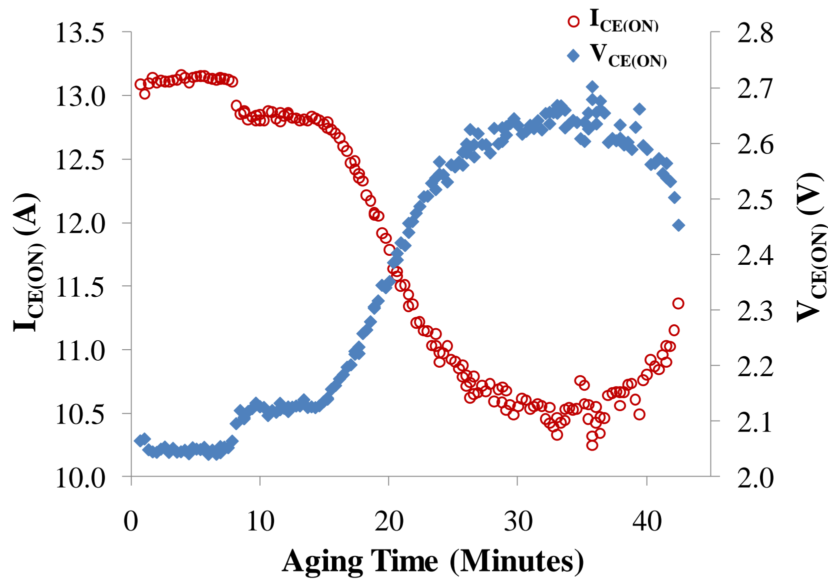

Figure 6-6: $I_{CE(ON)}$ and $V_{CE(ON)}$ vs. aging time for “N7” aged by test condition 1

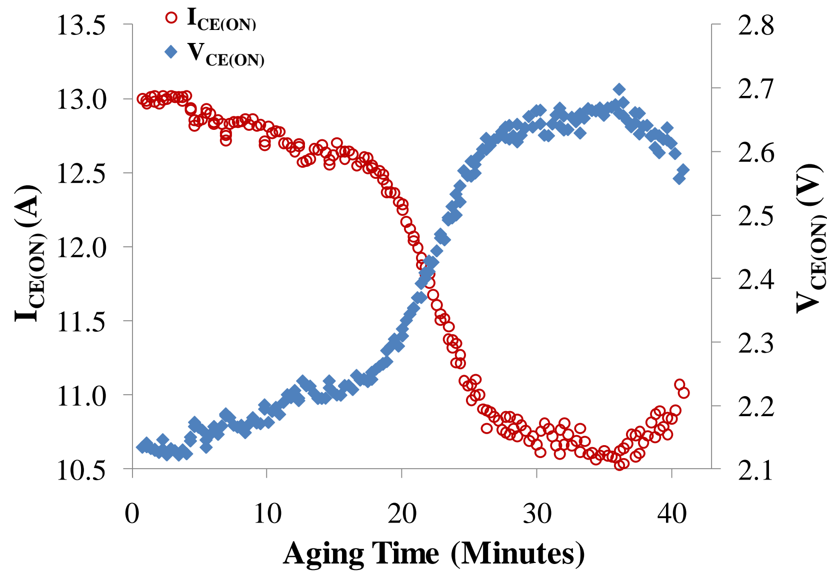

Figure 6-7: $I_{CE(ON)}$ and $V_{CE(ON)}$ vs. aging time for "N8" aged by test condition 1

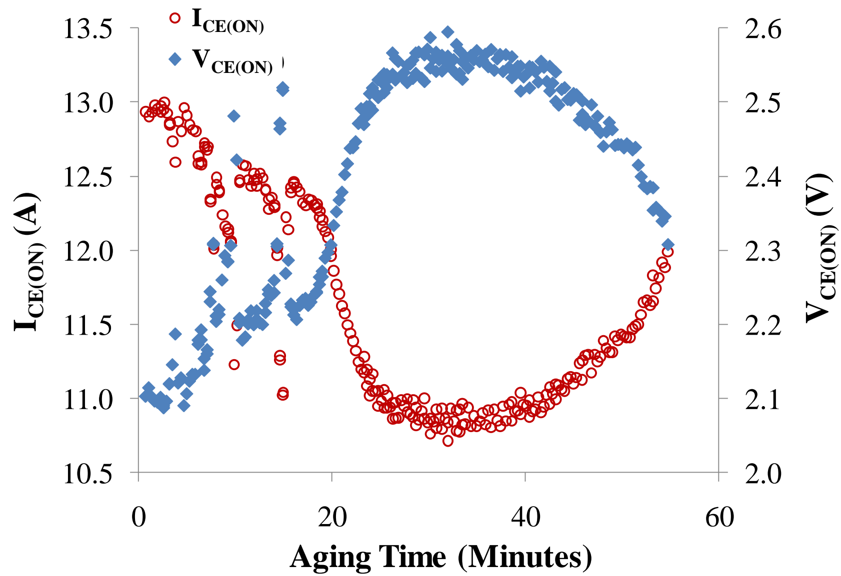

Figure 6-8: $I_{CE(ON)}$ and $V_{CE(ON)}$ vs. aging time for "N9" aged by test condition 1

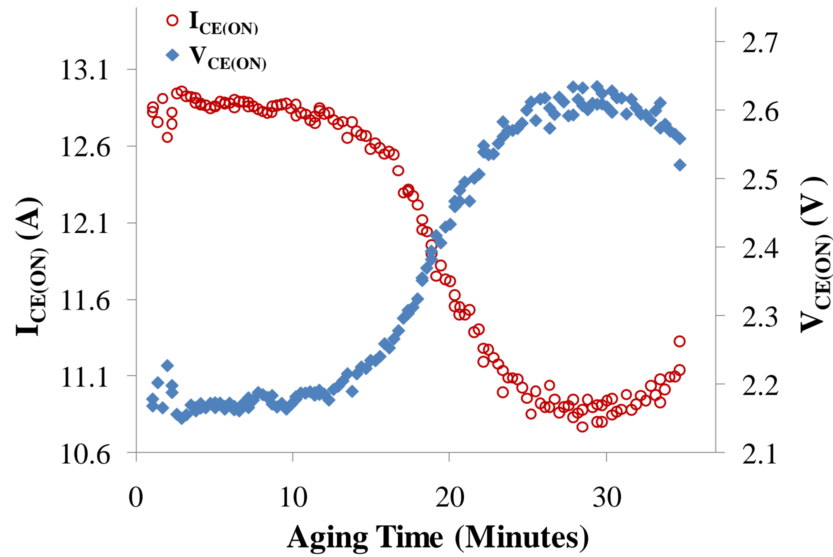

Figure 6-9: $I_{CE(ON)}$ and $V_{CE(ON)}$ vs. aging time for “N10” aged by test condition 1

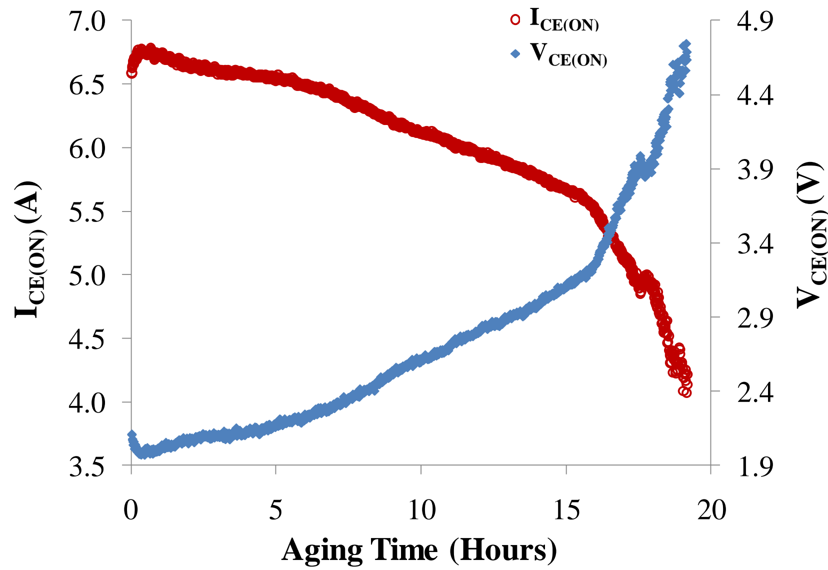

Figure 6-10: $I_{CE(ON)}$ and $V_{CE(ON)}$ vs. aging time for “NPT1” aged by test condition 2

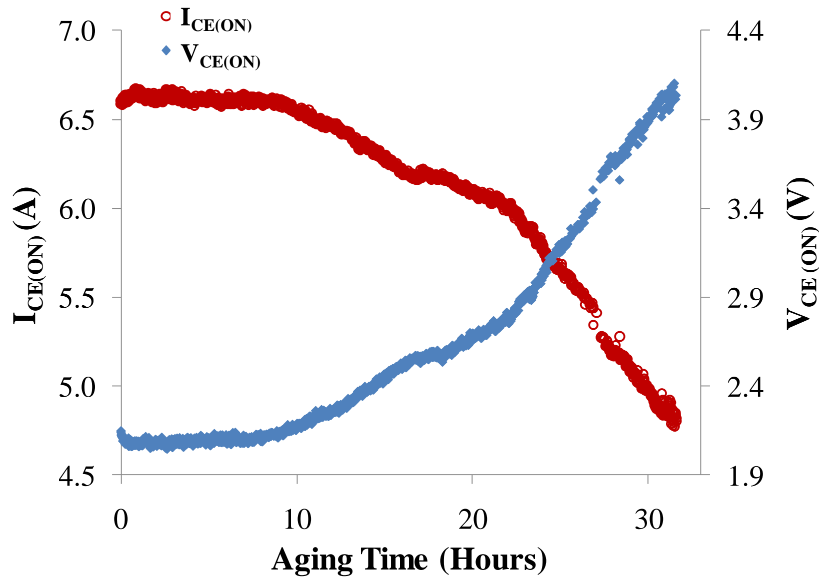

Figure 6-11: $I_{CE(ON)}$ and $V_{CE(ON)}$ vs. aging time for “NPT2” aged by test condition 2

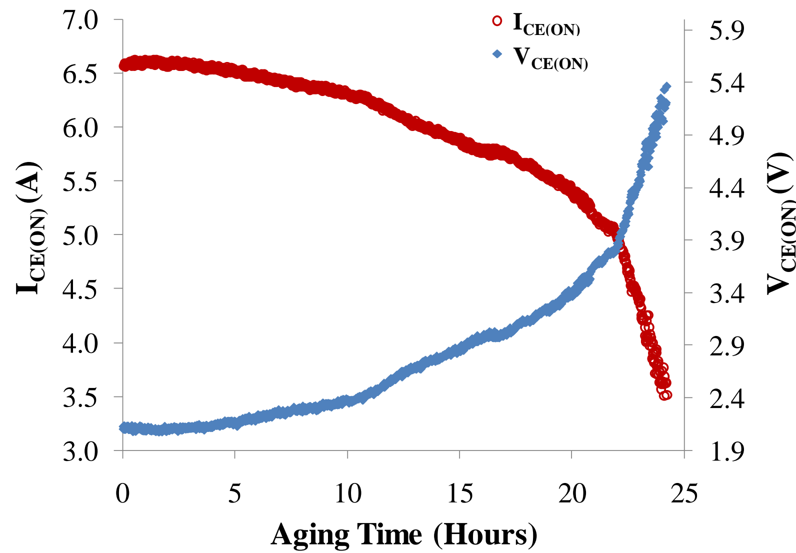

Figure 6-12: $I_{CE(ON)}$ and $V_{CE(ON)}$ vs. aging time for “NPT4” aged by test condition 2

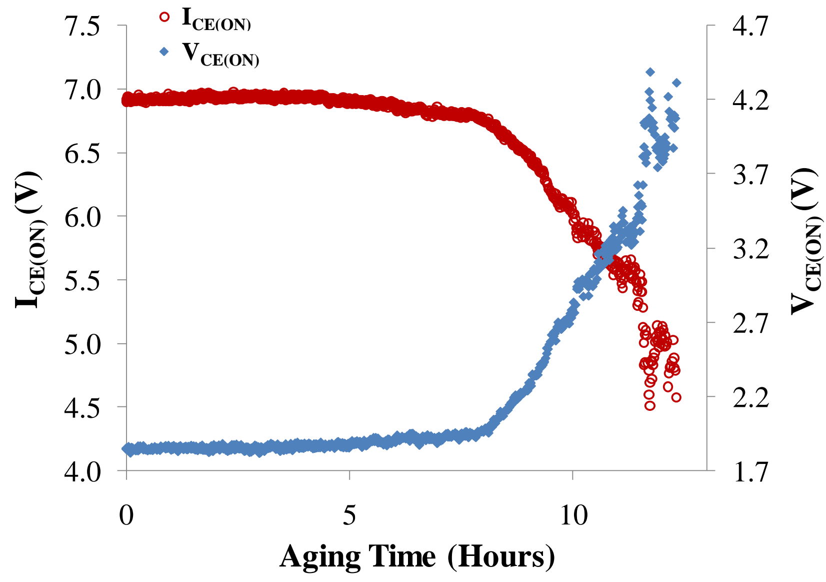

Figure 6-13: $I_{CE(ON)}$ and $V_{CE(ON)}$ vs. aging time for "NPT5" aged by test condition 2

Appendix B

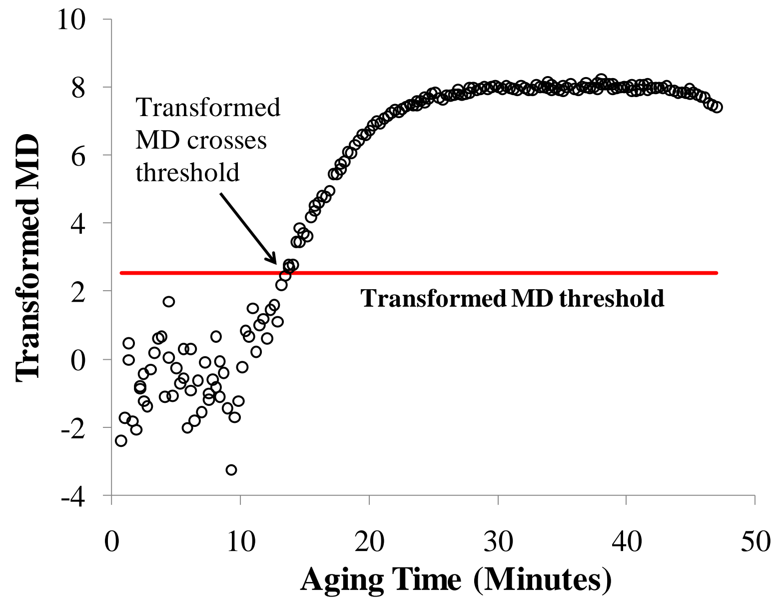

Figure 6-14: Transformed MD data vs. aging time for IGBT “N1”

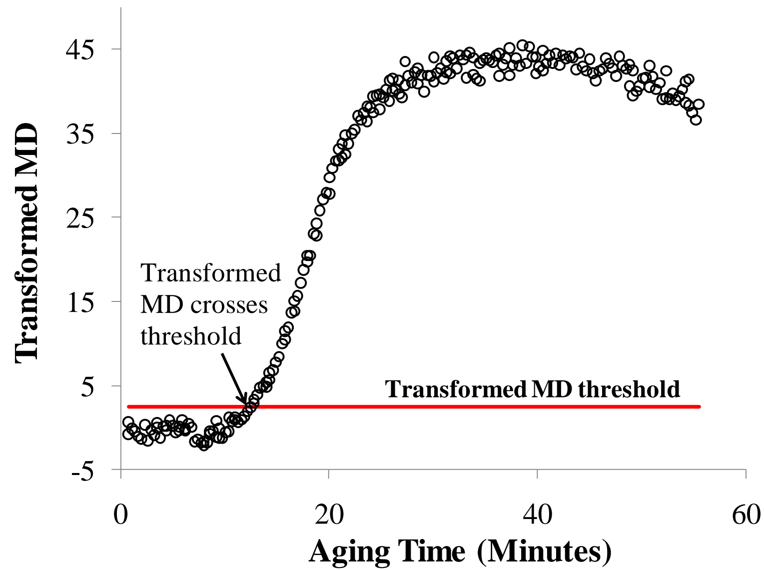

Figure 6-15: Transformed MD data vs. aging time for IGBT “N2”

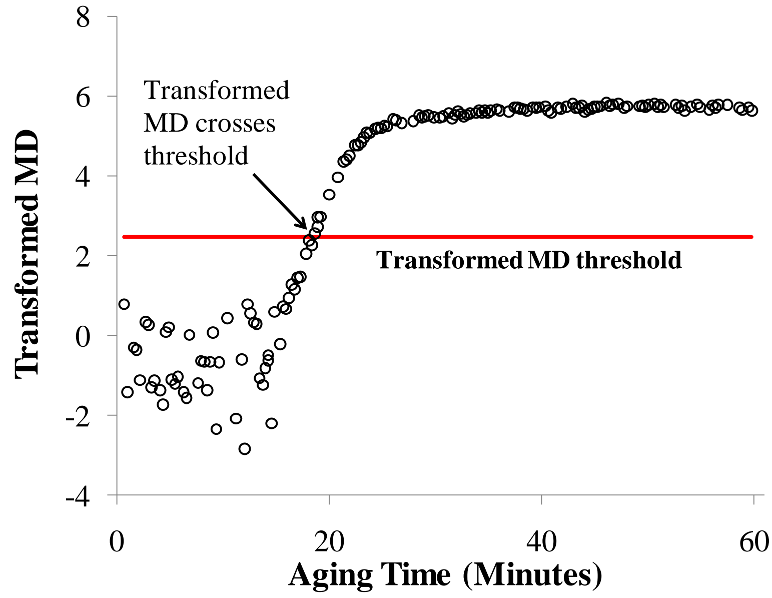

Figure 6-16: Transformed MD data vs. aging time for IGBT “N4”

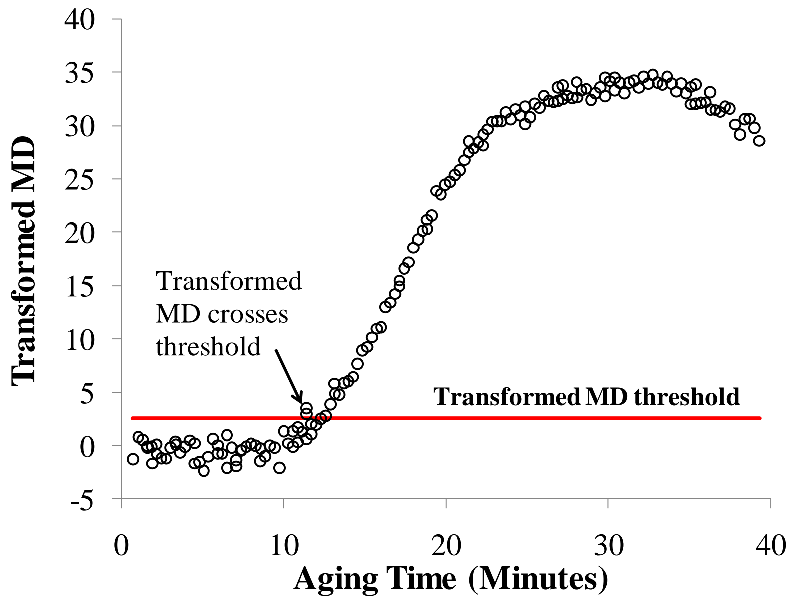

Figure 6-17: Transformed MD data vs. aging time for IGBT “N5”

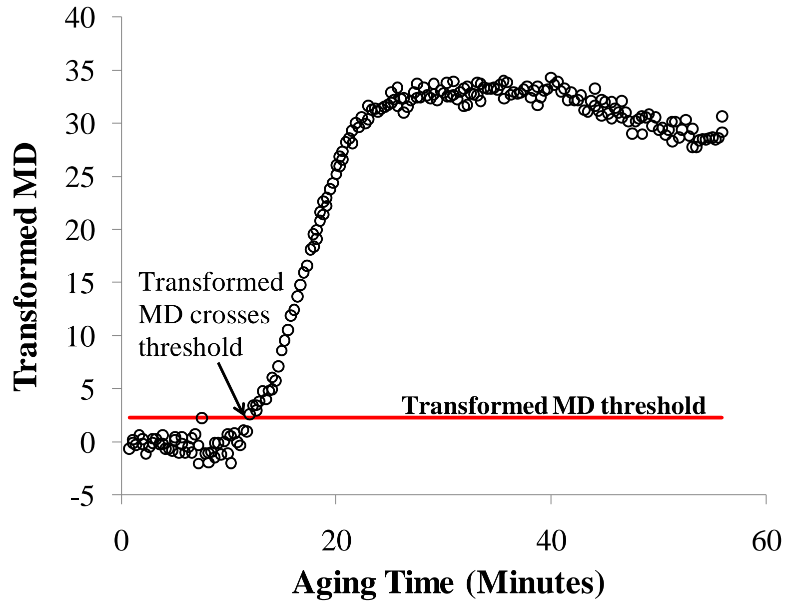

Figure 6-18: Transformed MD data vs. aging time for IGBT “N6”

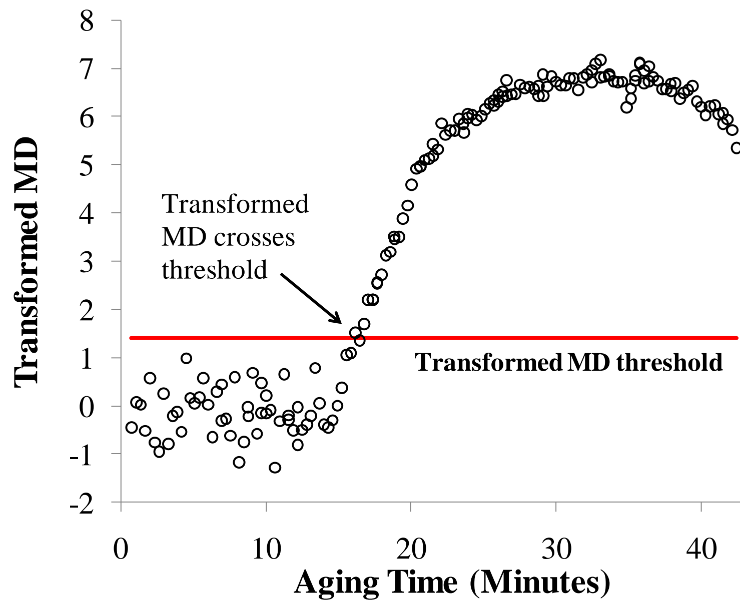

Figure 6-19: Transformed MD data vs. aging time for IGBT “N7”

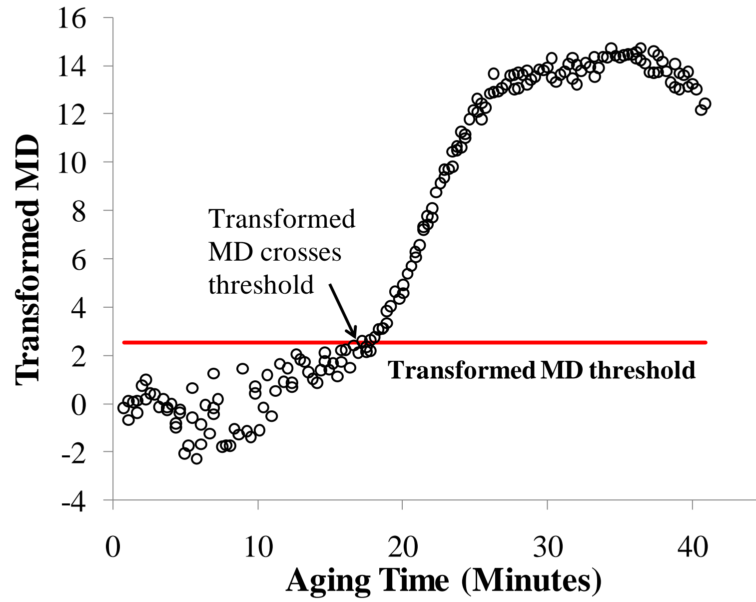

Figure 6-20: Transformed MD data vs. aging time for IGBT “N8”

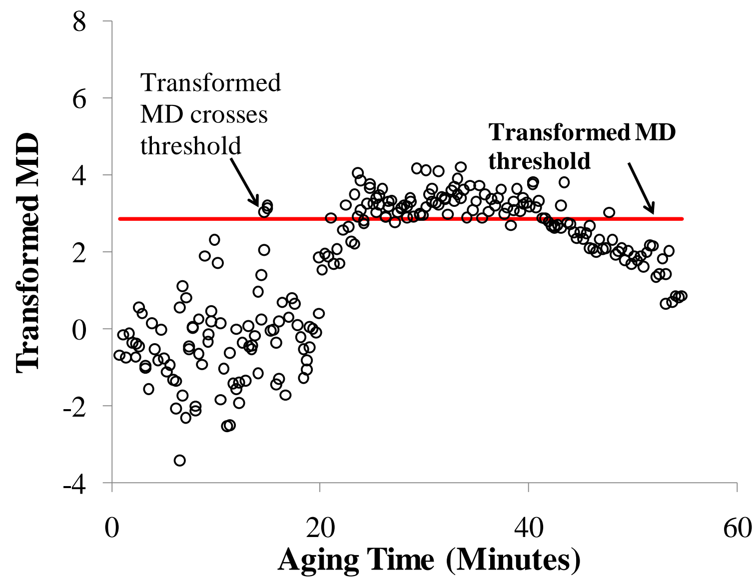

Figure 6-21: Transformed MD data vs. aging time for IGBT “N9”

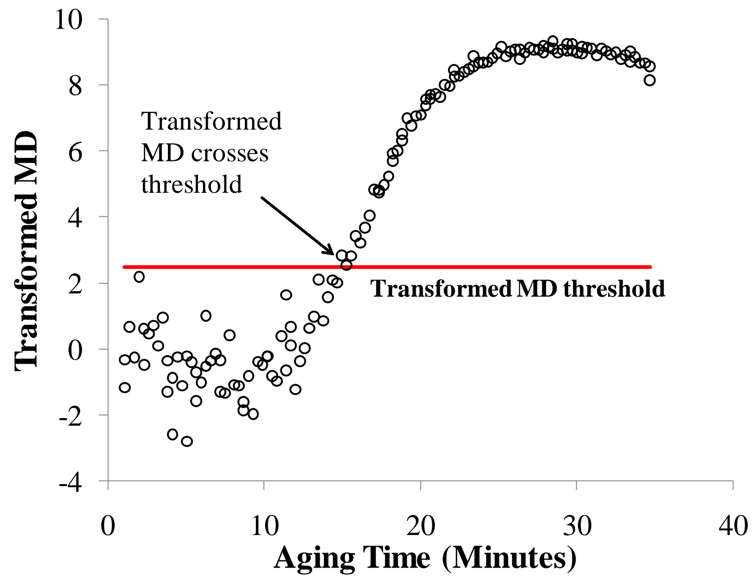

Figure 6-22: Transformed MD data vs. aging time for IGBT “N10”

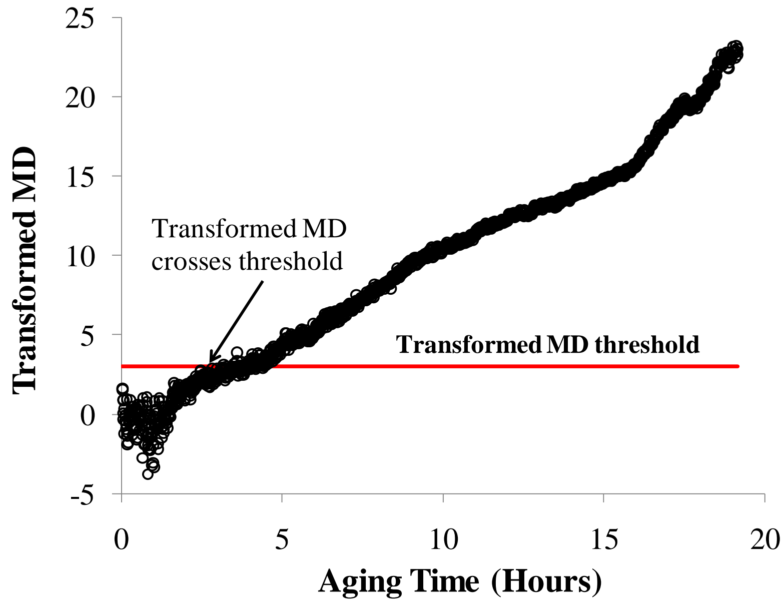

Figure 6-23: Transformed MD data vs. aging time for IGBT “NPT1”

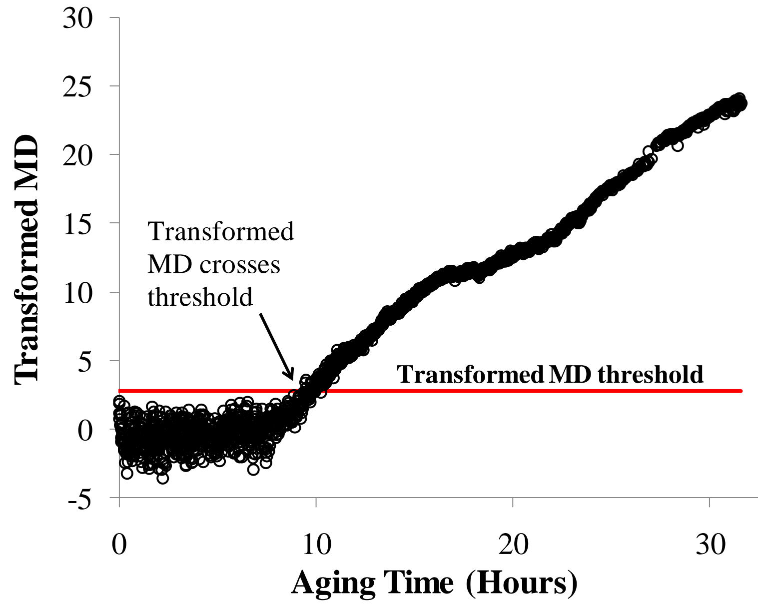

Figure 6-24: Transformed MD data vs. aging time for IGBT “NPT2”

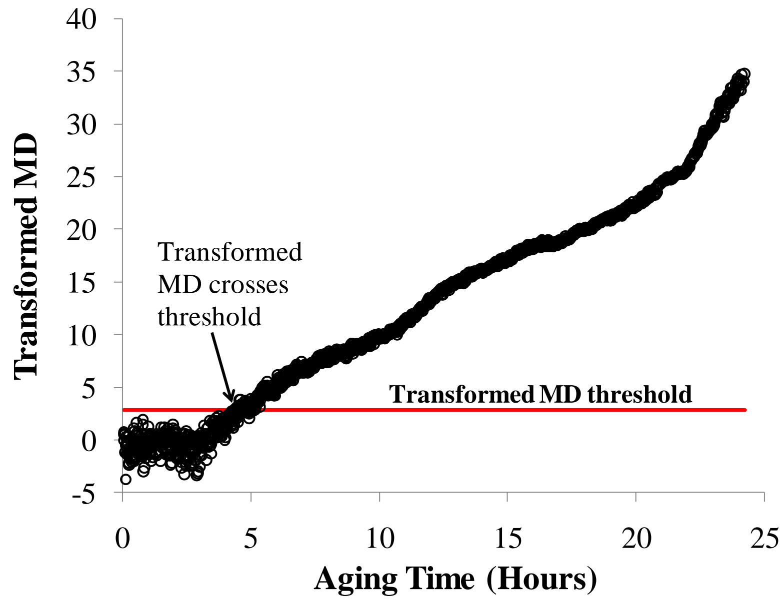

Figure 6-25: Transformed MD data vs. aging time for IGBT “NPT4”

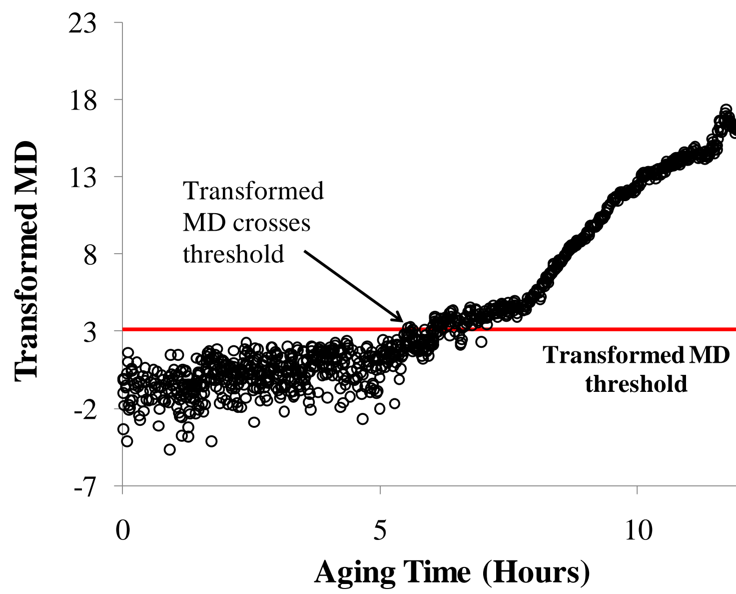

Figure 6-26: Transformed MD data vs. aging time for IGBT “NPT5”

Appendix C

Predictions for "N4" IGBT after 3, 6, 12 and 18 minutes

Prediction for10 particles

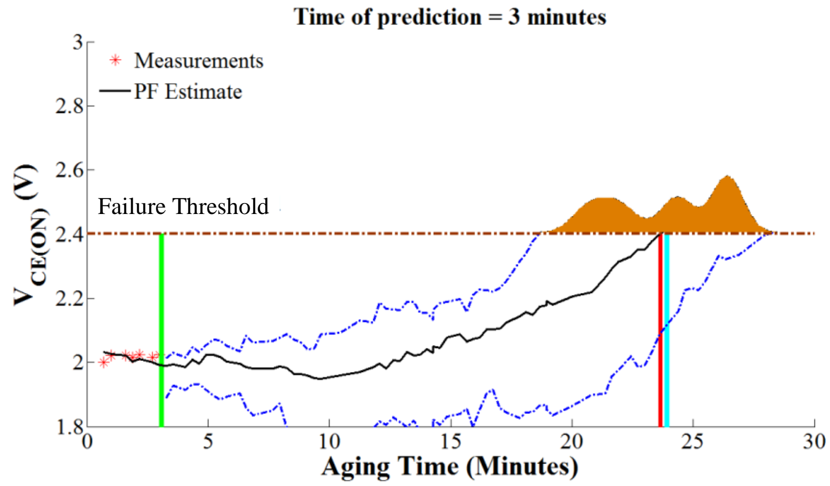

Figure 6-27: Prediction for N= 10 particles and time t= 3 minutes

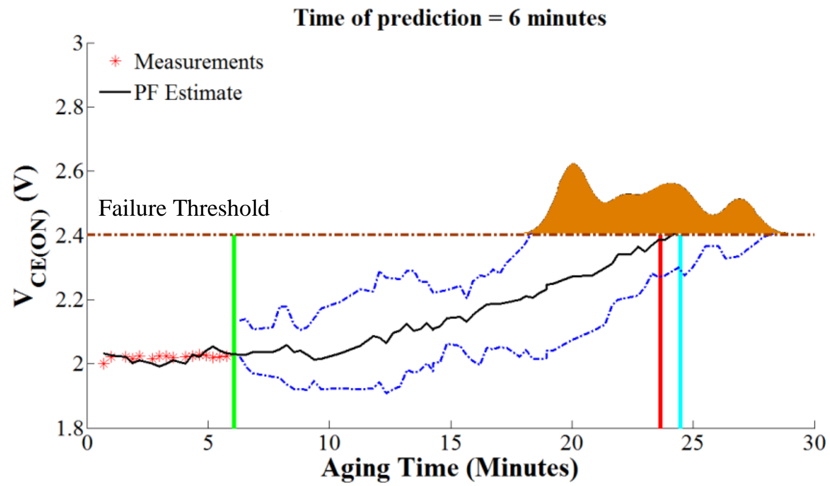

Figure 6-28: Prediction for N= 10 particles and time t= 6 minutes

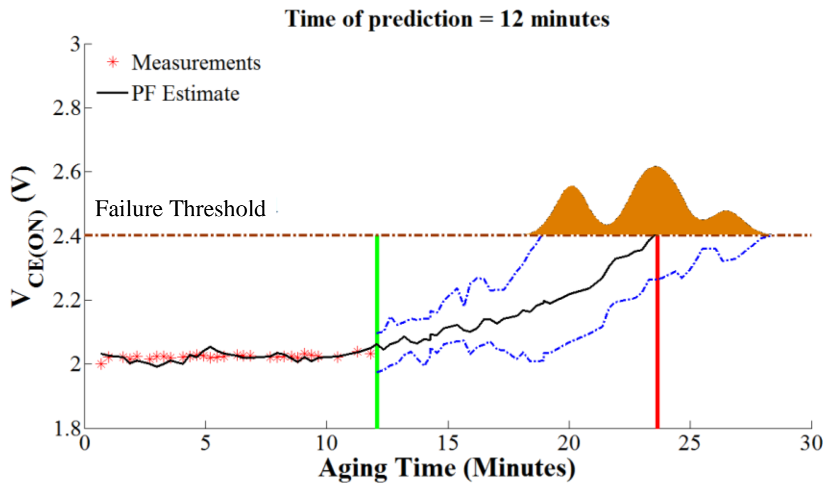

Figure 6-29: Prediction for N= 10 particles and time t= 12 minutes

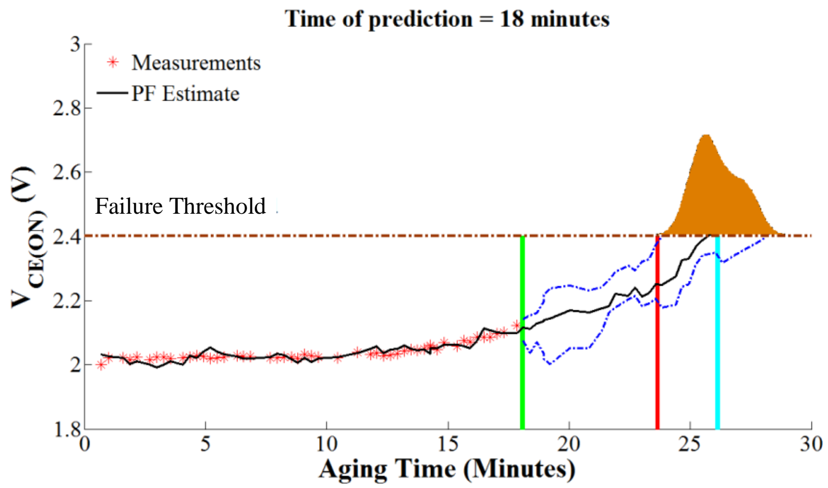

Figure 6-30: Prediction for N= 10 particles and time t= 18 minutes

Prediction for 30 particles

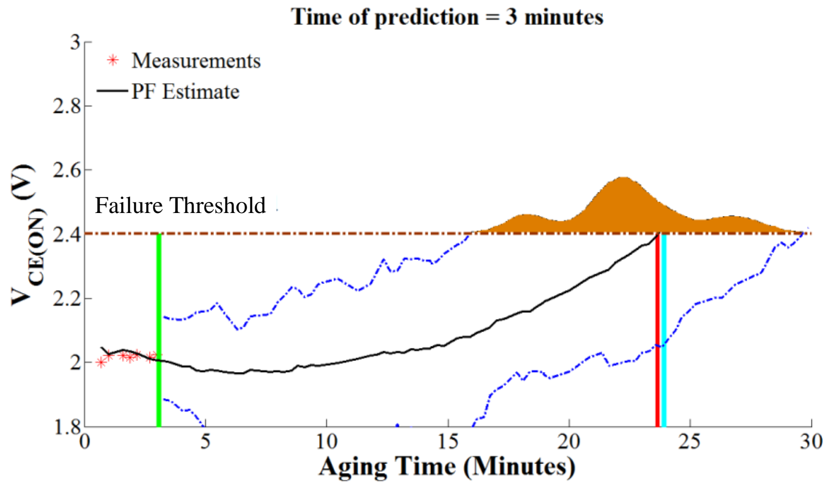

Figure 6-31: Prediction for N= 30 particles and time t= 3 minutes

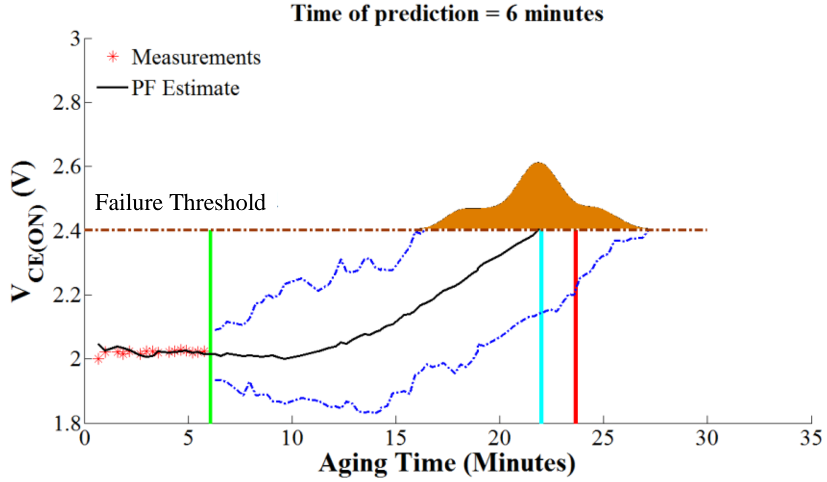

Figure 6-32: Prediction for N= 30 particles and time t= 6 minutes

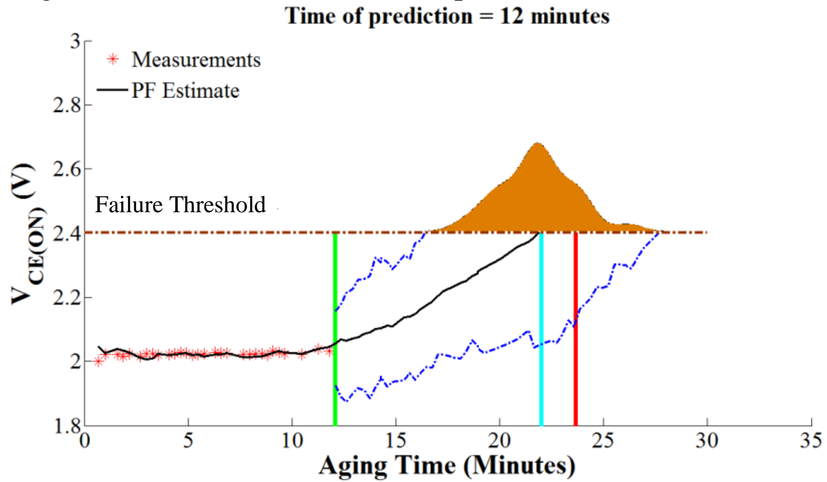

Figure 6-33: Prediction for N= 30 particles and time t= 12 minutes

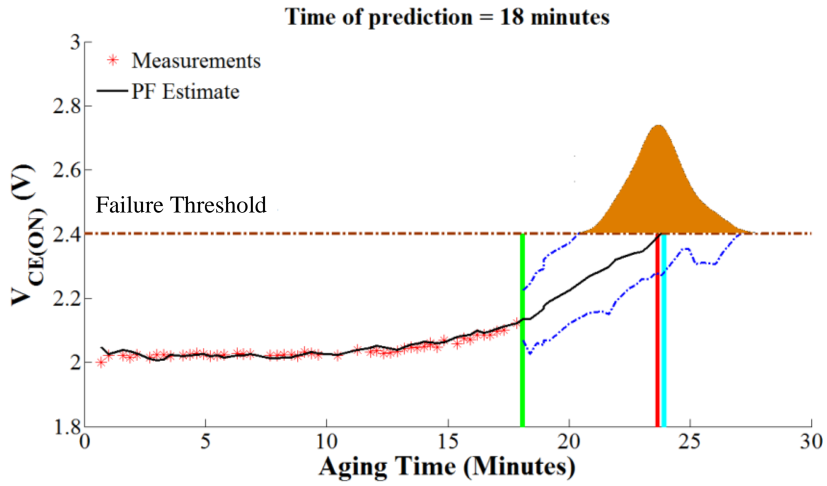

Figure 6-34: Prediction for N= 30 particles and time t= 18 minutes

Prediction for 100 particles

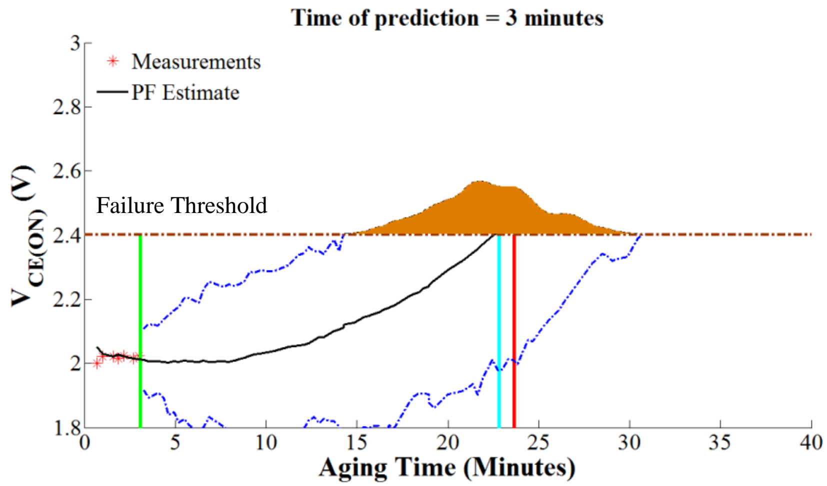

Figure 6-35: Prediction for N= 100 particles and time t= 3 minutes

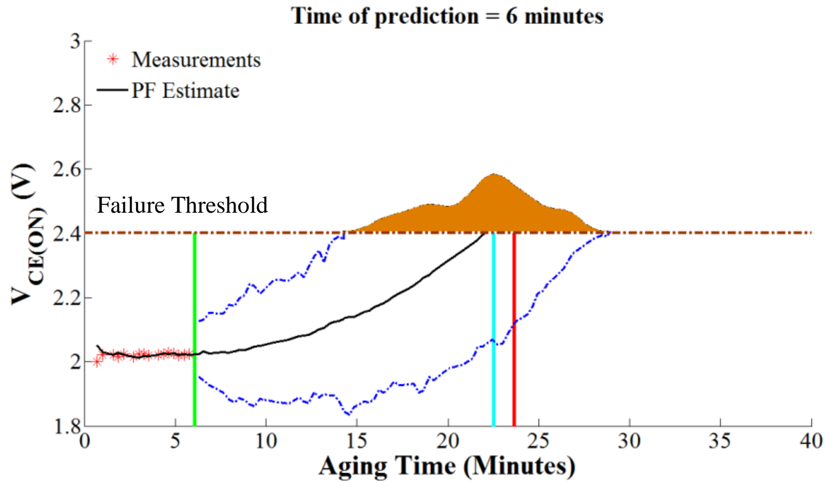

Figure 6-36: Prediction for N= 100 particles and time t= 6 minutes

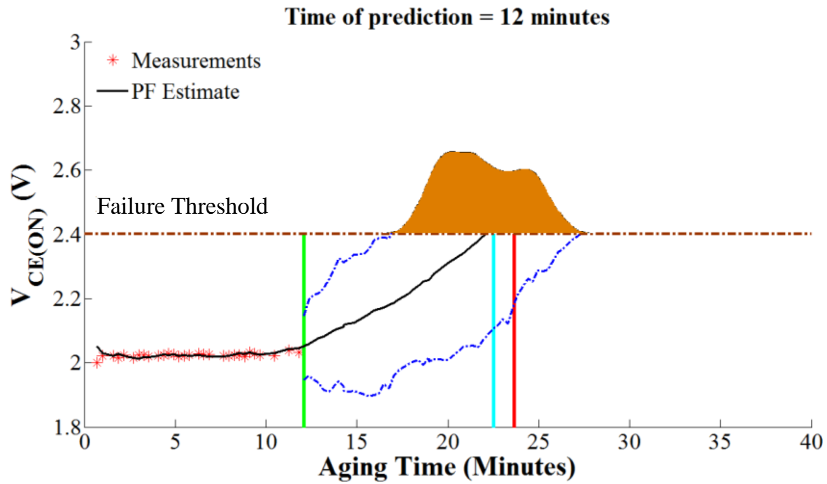

Figure 6-37: Prediction for N= 100 particles and time t= 12 minutes

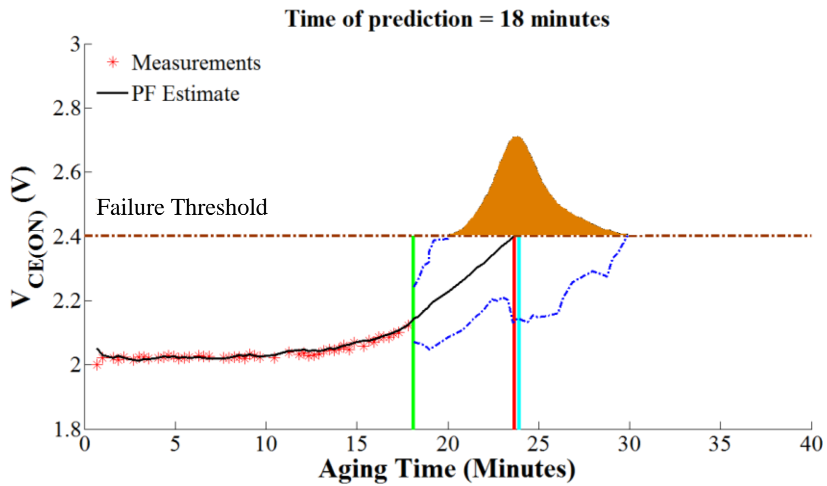

Figure 6-38: Prediction for N= 100 particles and time t= 18 minutes

Prediction for 300 particles

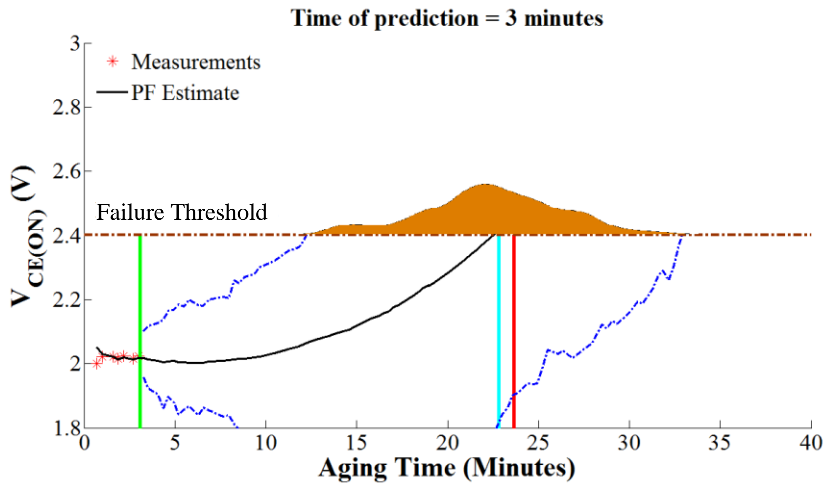

Figure 6-39: Prediction for N= 300 particles and time t= 3 minutes

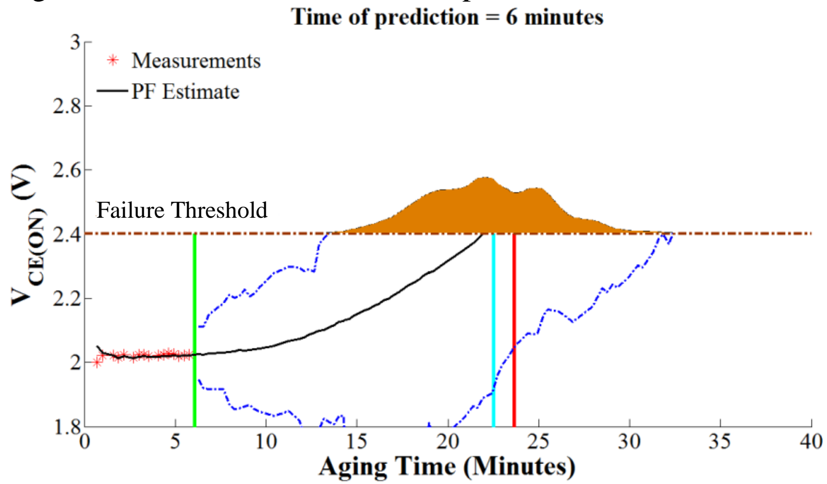

Figure 6-40: Prediction for N= 300 particles and time t= 6 minutes

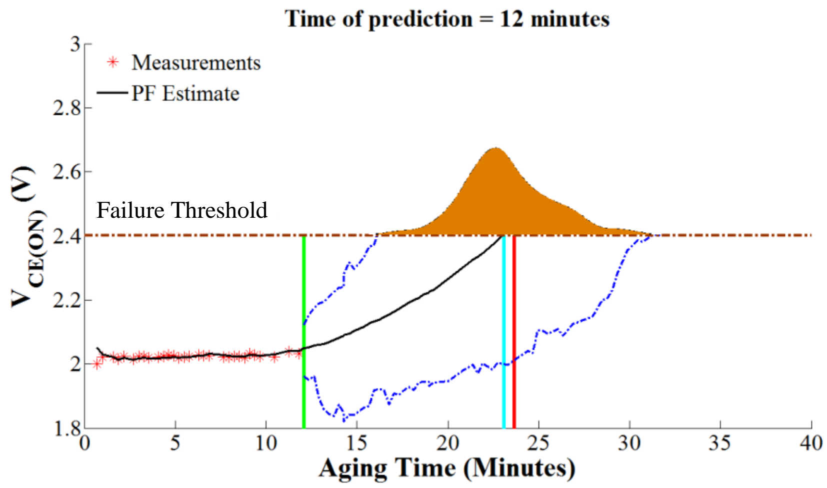

Figure 6-41: Prediction for N= 300 particles and time t= 12 minutes

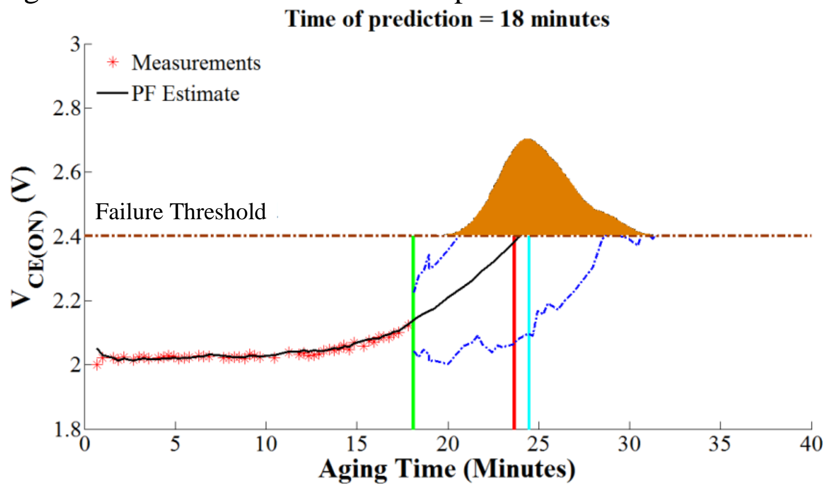

Figure 6-42: Prediction for N= 300 particles and time t= 18 minutes

Predictions for "N5" IGBT after 3, 6, 12 and 18 minutes

Prediction for 10 particles

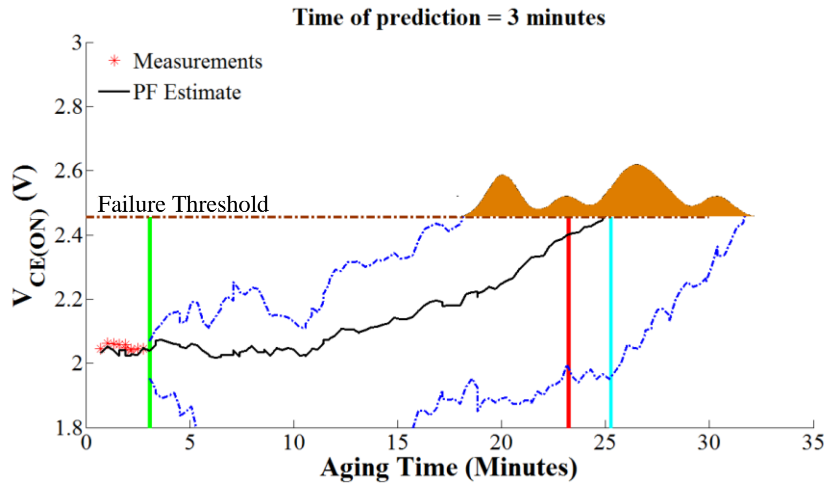

Figure 6-43: Prediction for N= 10 particles and time t= 3 minutes

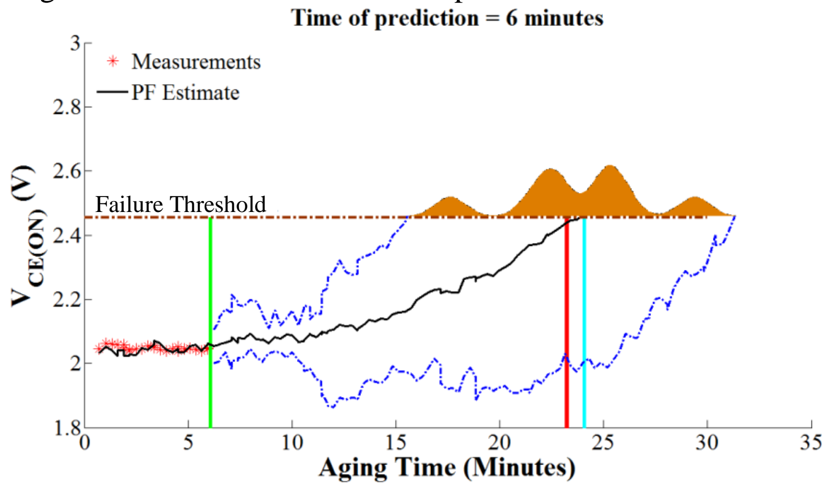

Figure 6-44: Prediction for N= 10 particles and time t= 6 minutes

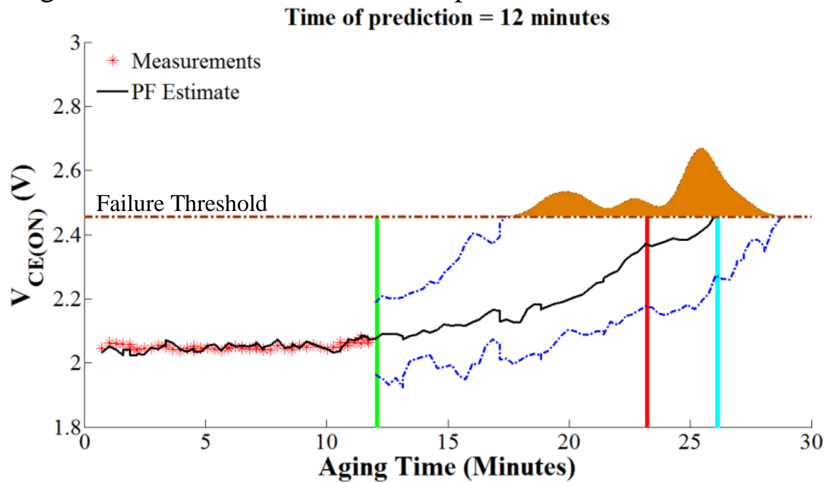

Figure 6-45: Prediction for N= 10 particles and time t= 12 minutes

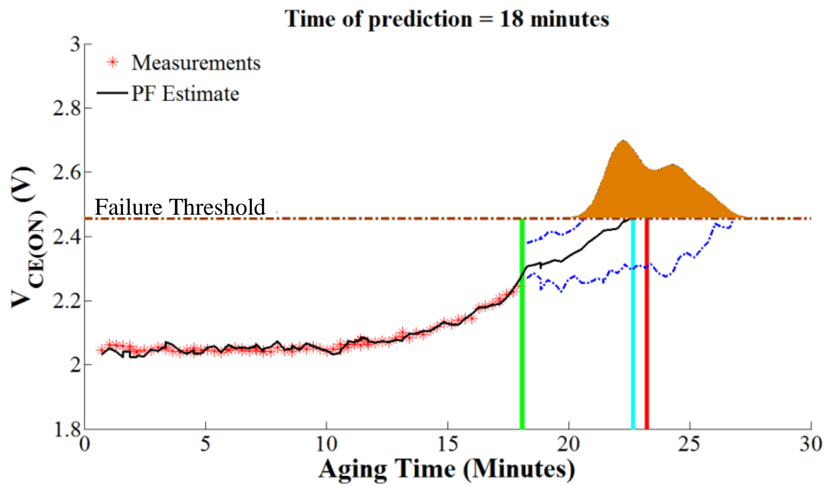

Figure 6-46: Prediction for N= 10 particles and time t= 18 minutes

Prediction for 30 particles

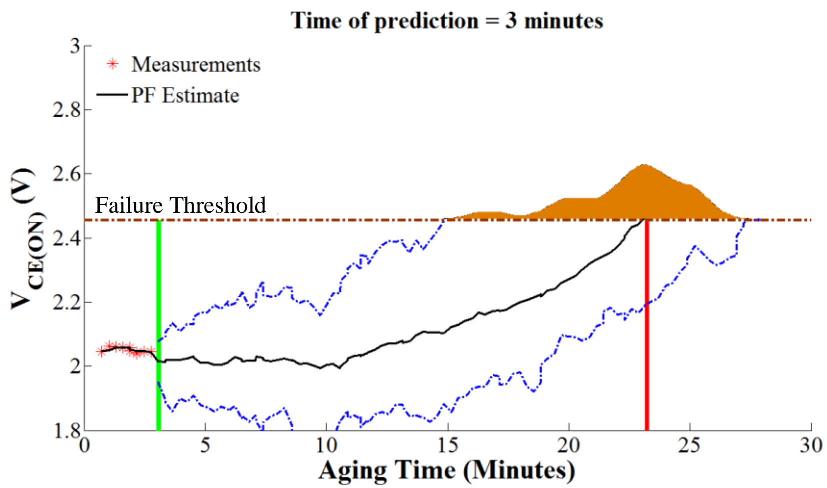

Figure 6-47: Prediction for N= 30 particles and time t= 3 minutes

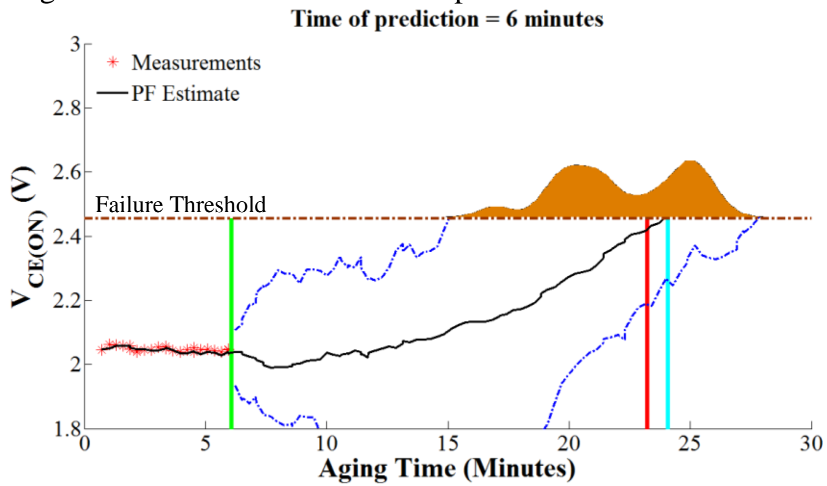

Figure 6-48: Prediction for N= 30 particles and time t= 6 minutes

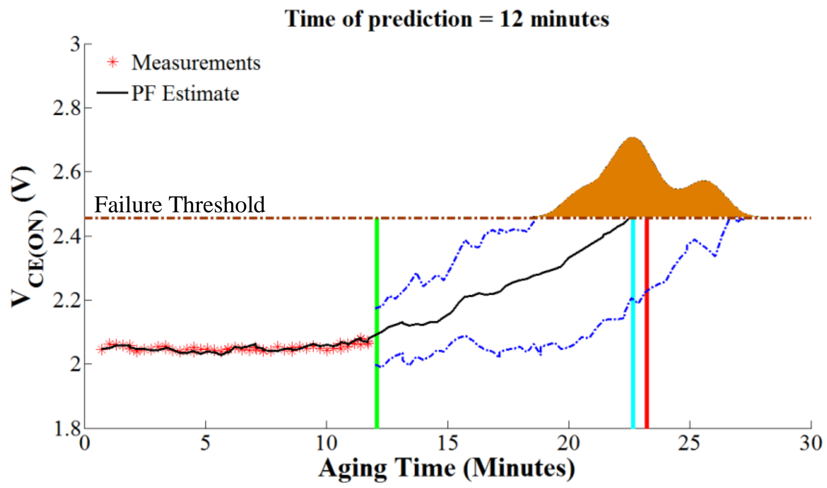

Figure 6-49: Prediction for N= 30 particles and time t= 12 minutes

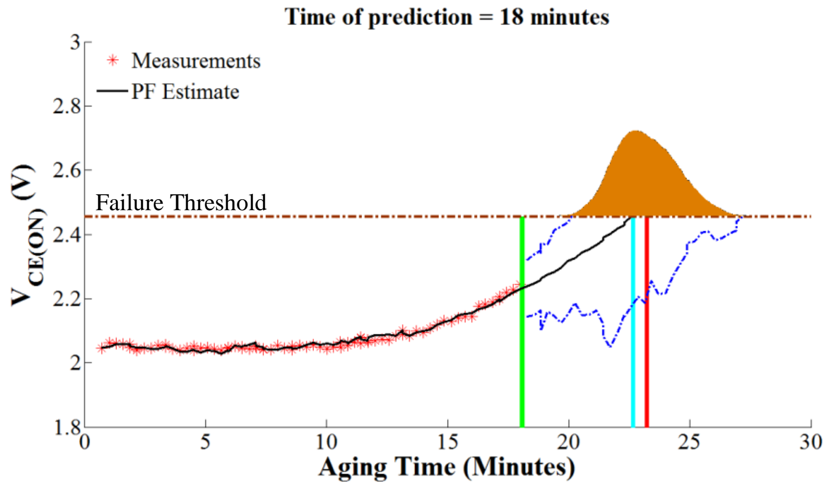

Figure 6-50: Prediction for N= 30 particles and time t= 18 minutes

Prediction for 100 particles

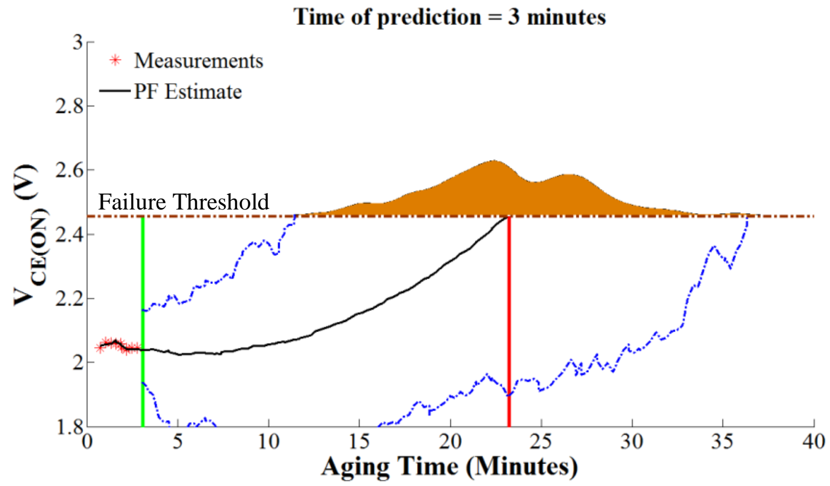

Figure 6-51: Prediction for N= 100 particles and time t= 3 minutes

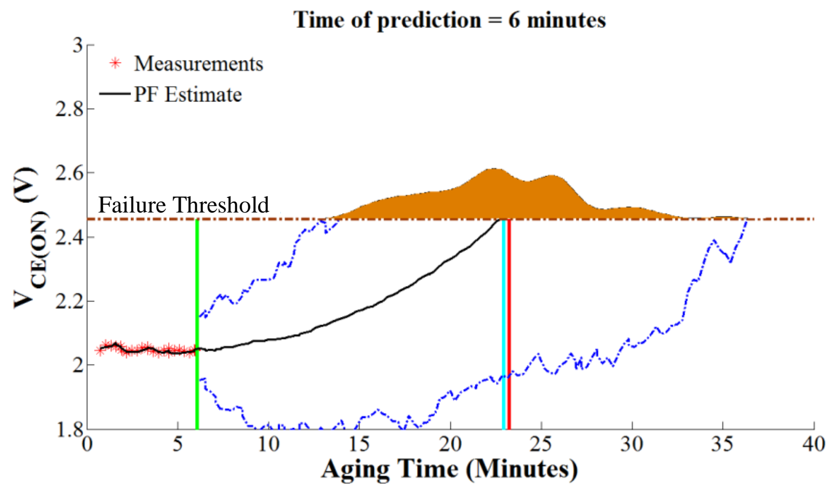

Figure 6-52: Prediction for N= 100 particles and time t= 6 minutes

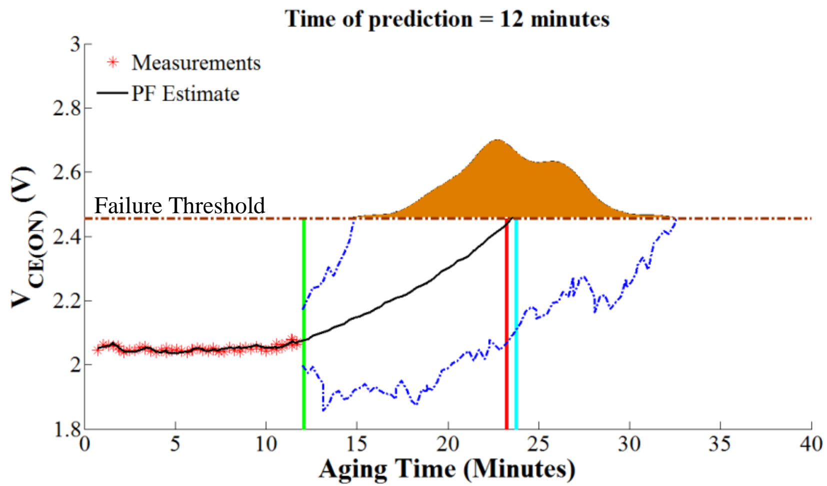

Figure 6-53: Prediction for N= 100 particles and time t= 12 minutes

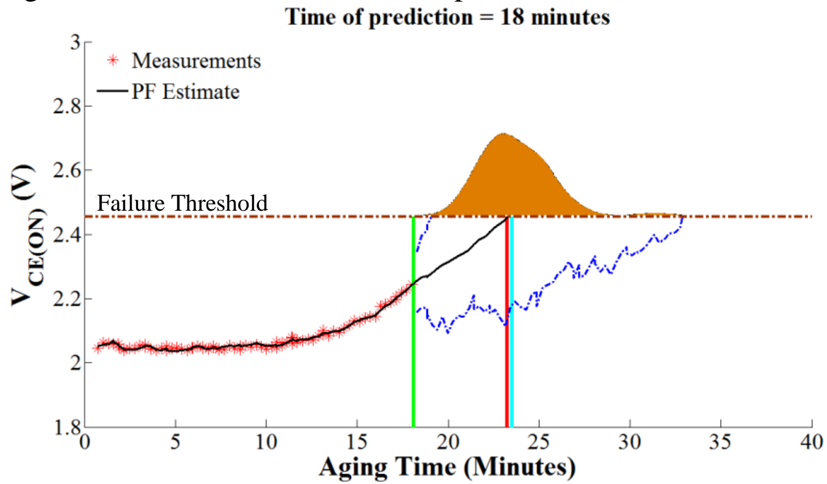

Figure 6-54: Prediction for N= 100 particles and time t= 18 minutes

Prediction for 300 particles

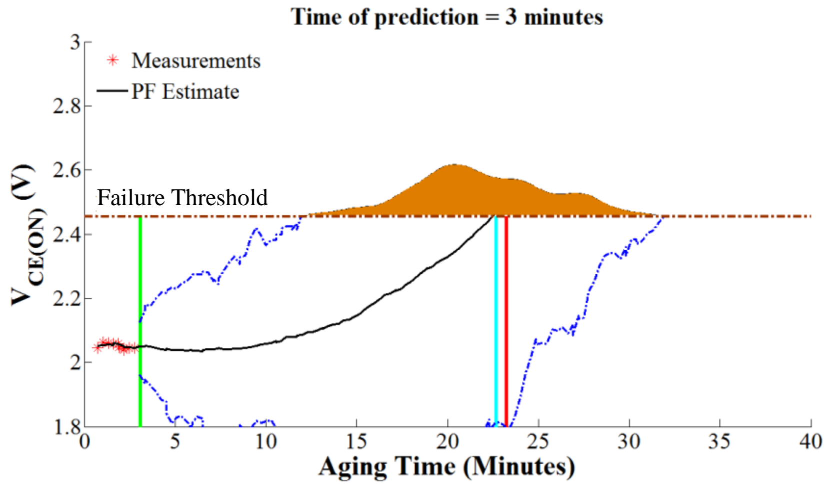

Figure 6-55: Prediction for N= 300 particles and time t= 3 minutes

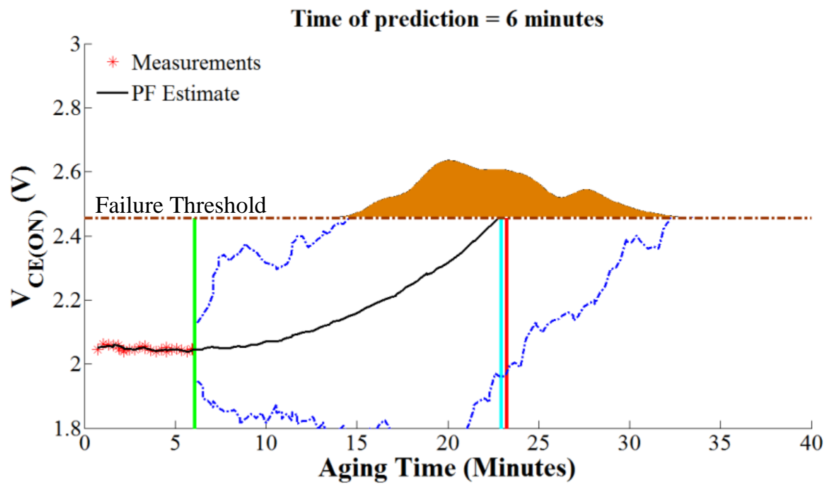

Figure 6-56: Prediction for N= 300 particles and time t= 6 minutes

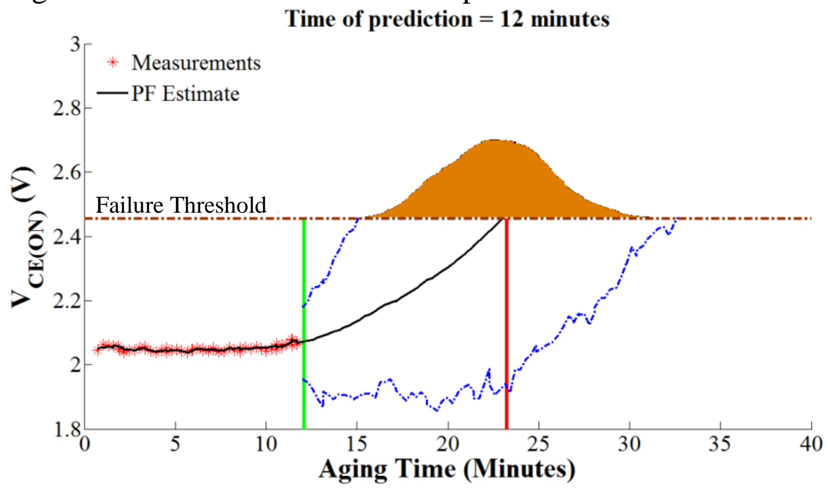

Figure 6-57: Prediction for N= 300 particles and time t= 12 minutes

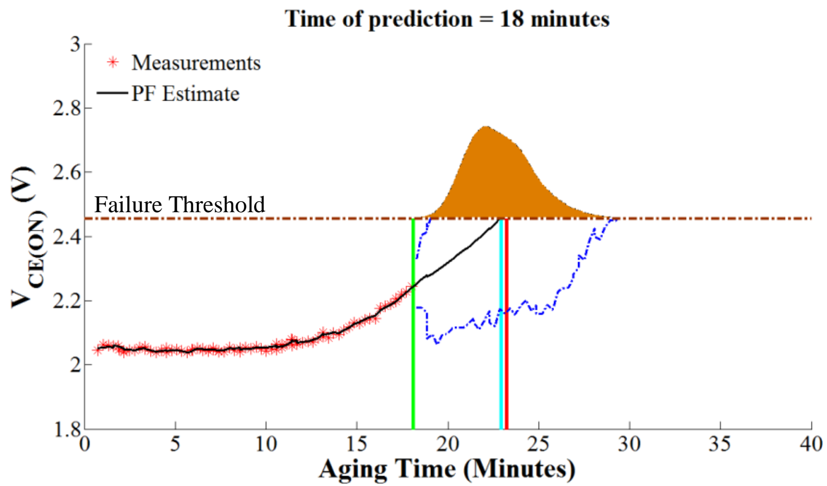

Figure 6-58: Prediction for N= 300 particles and time t= 18 minutes

Predictions for "N6" IGBT after 3, 6, 12 and 18 minutes

Prediction for 10 particles

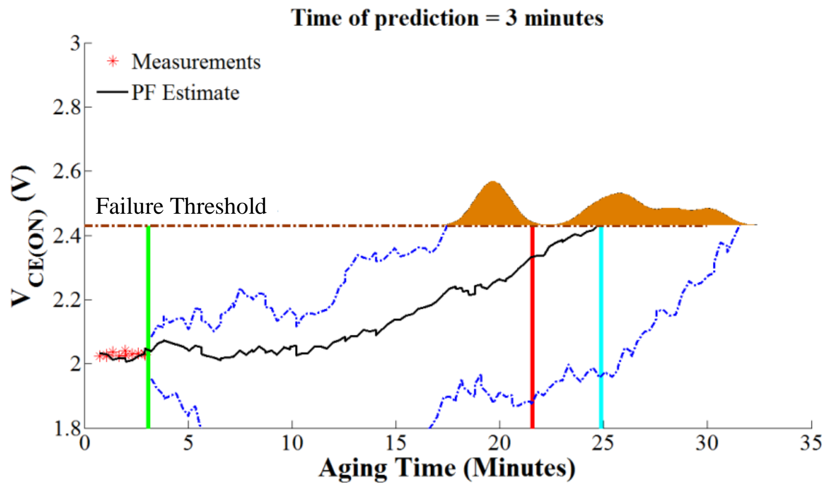

Figure 6-59: Prediction for N= 10 particles and time t= 3 minutes

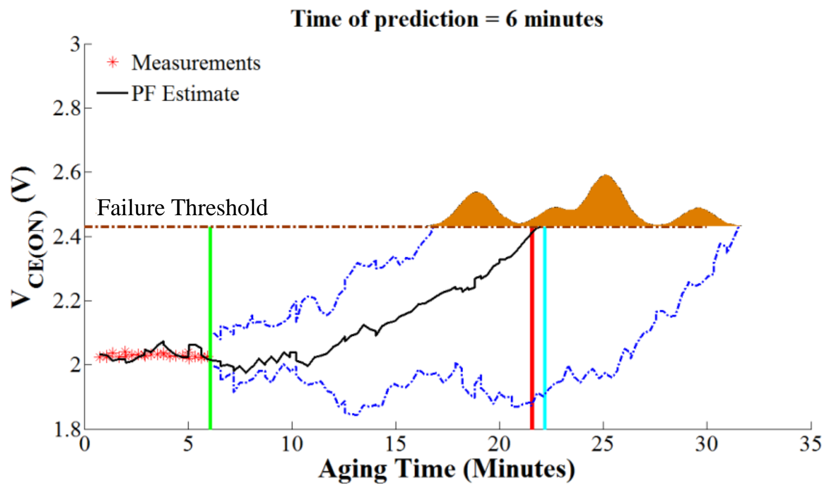

Figure 6-60: Prediction for N= 10 particles and time t= 6 minutes

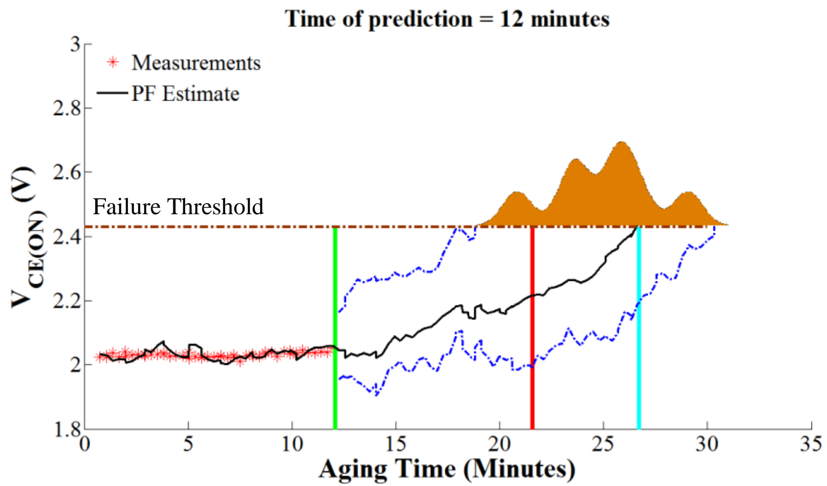

Figure 6-61: Prediction for N= 10 particles and time t= 12 minutes

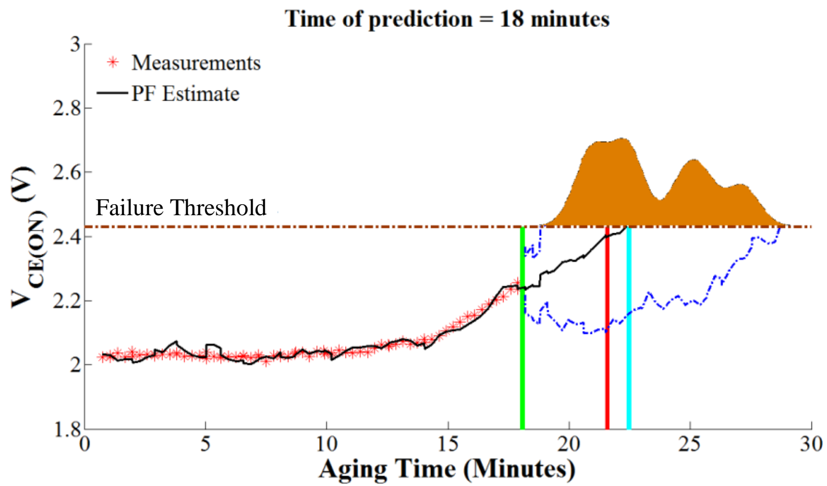

Figure 6-62: Prediction for N= 10 particles and time t= 18 minutes

Prediction for 30 particles

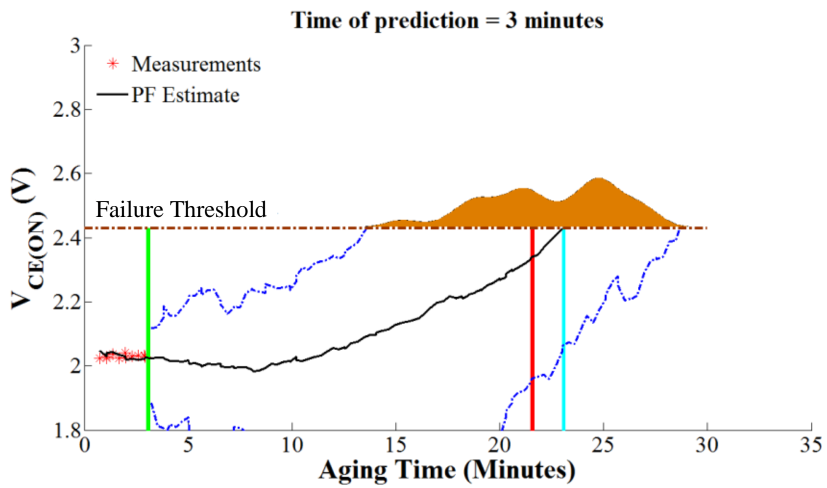

Figure 6-63: Prediction for N= 30 particles and time t= 3 minutes

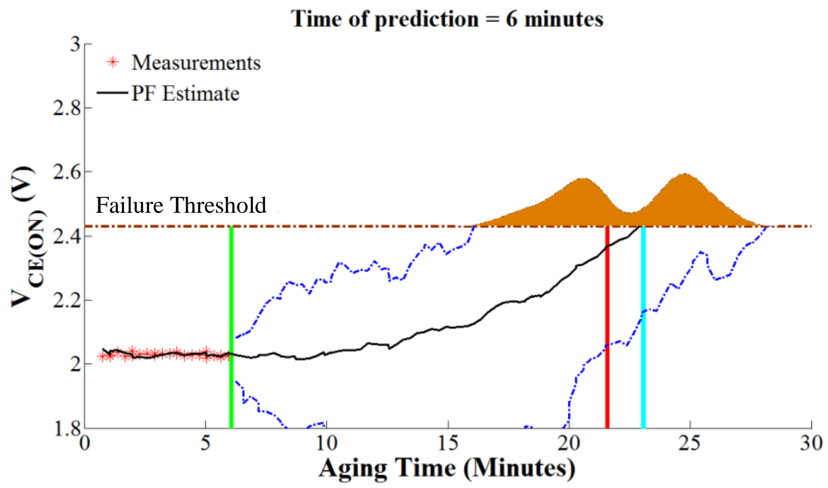

Figure 6-64: Prediction for N= 30 particles and time t= 6 minutes

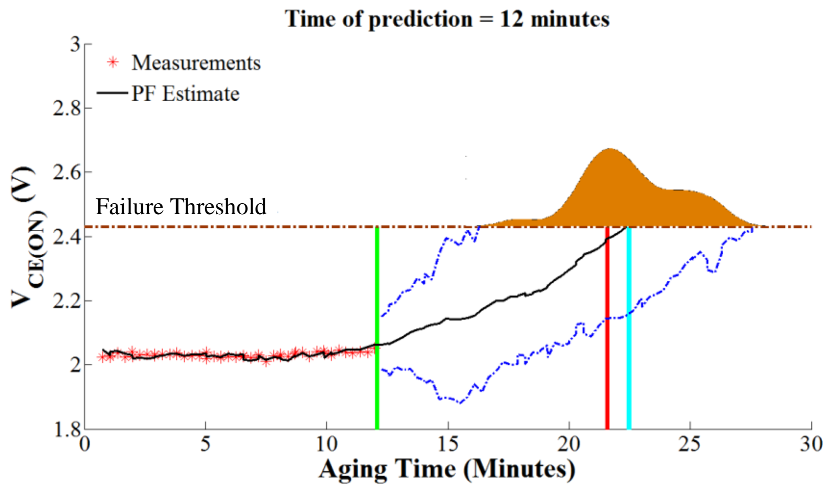

Figure 6-65: Prediction for N= 30 particles and time t= 12 minutes

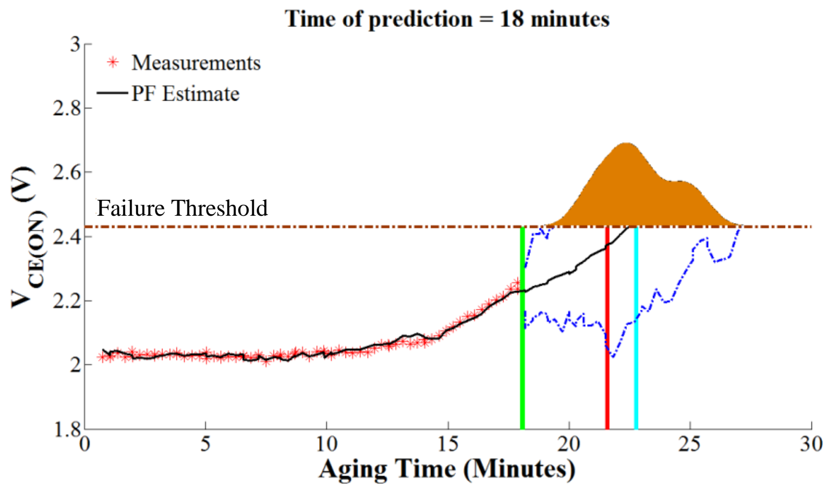

Figure 6-66: Prediction for N= 30 particles and time t= 18 minutes

Prediction for 100 particles

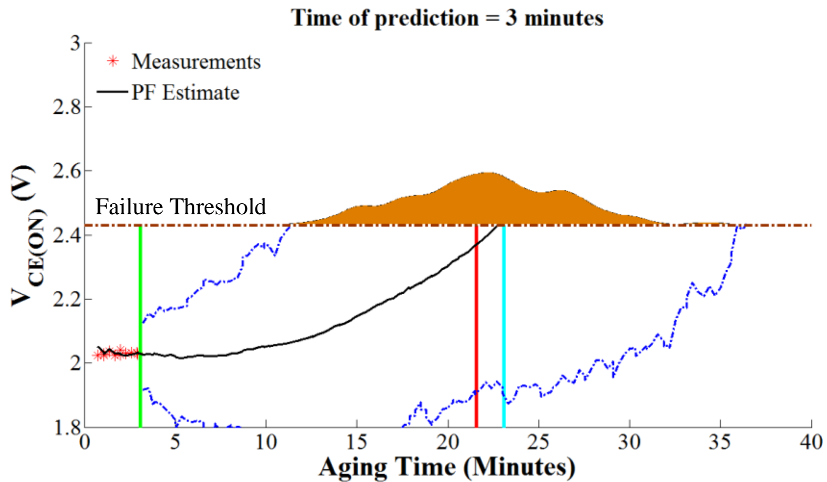

Figure 6-67: Prediction for N= 100 particles and time t= 3 minutes

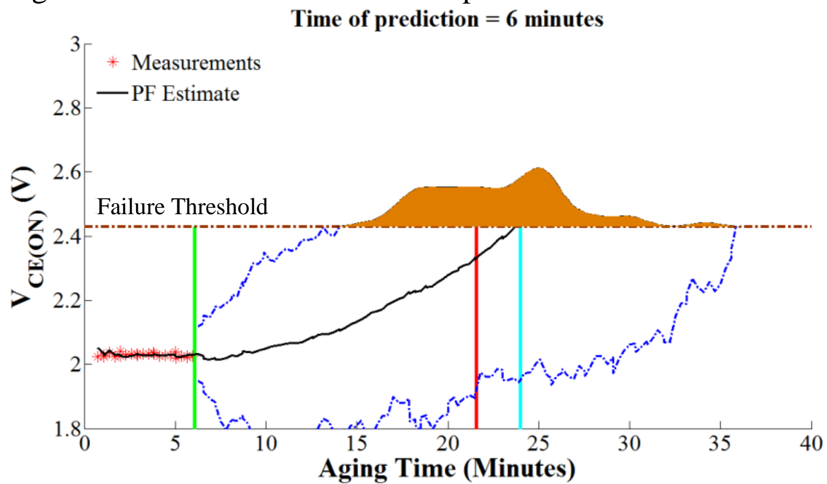

Figure 6-68: Prediction for N= 100 particles and time t= 6 minutes

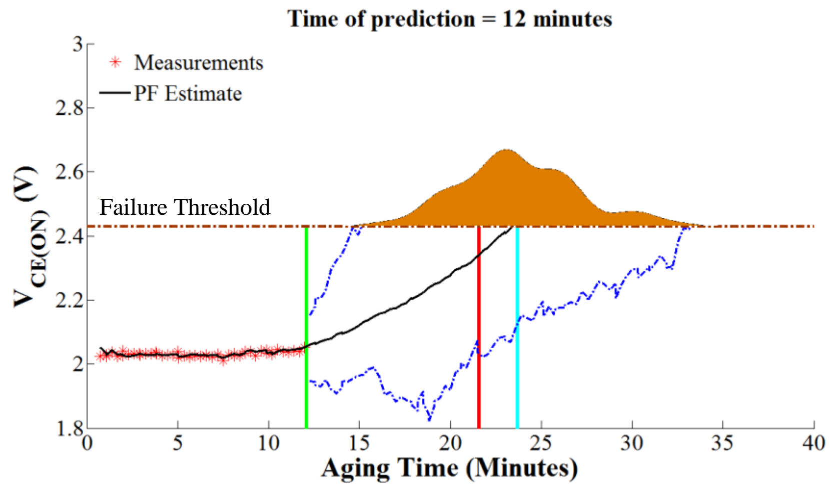

Figure 6-69: Prediction for N= 100 particles and time t= 12 minutes

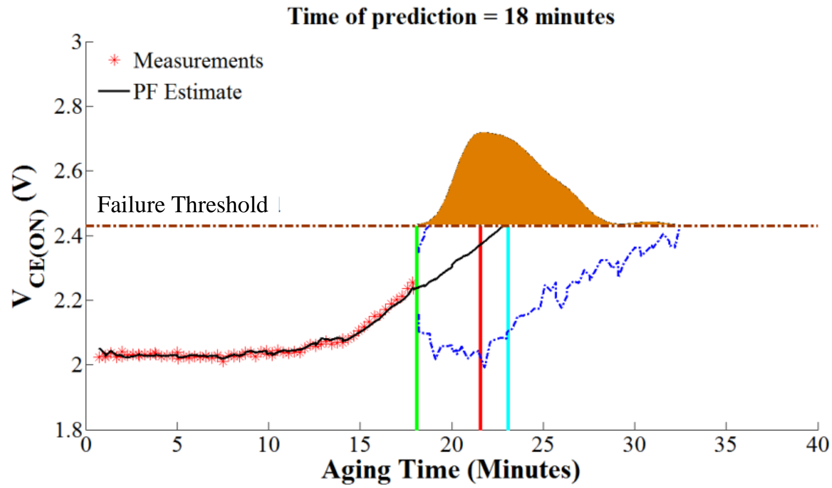

Figure 6-70: Prediction for N= 100 particles and time t= 18 minutes

Prediction for 300 particles

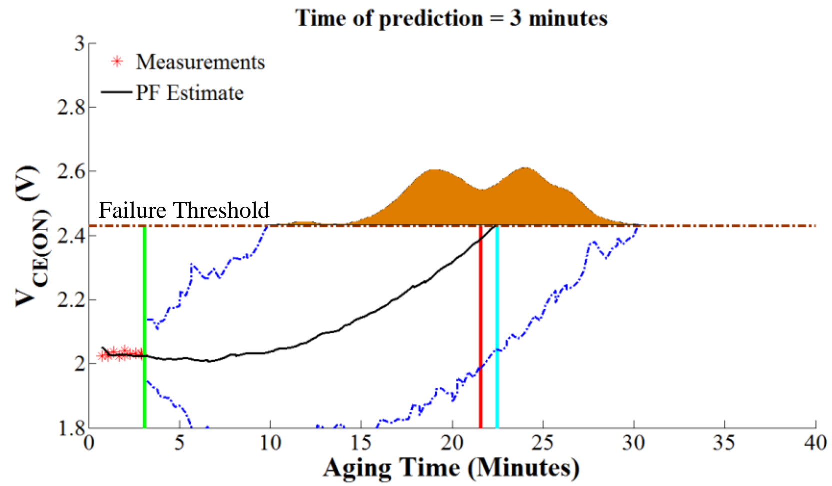

Figure 6-71: Prediction for N= 300 particles and time t= 3 minutes

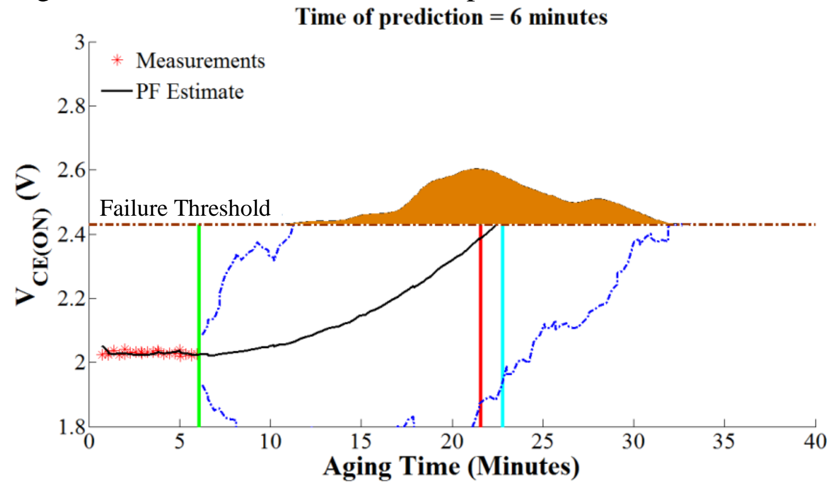

Figure 6-72: Prediction for N= 300 particles and time t= 6 minutes

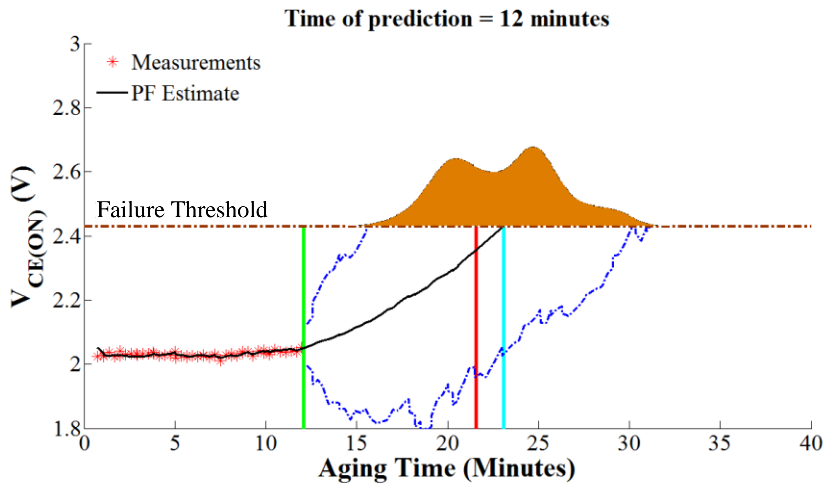

Figure 6-73: Prediction for N= 300 particles and time t= 12 minutes

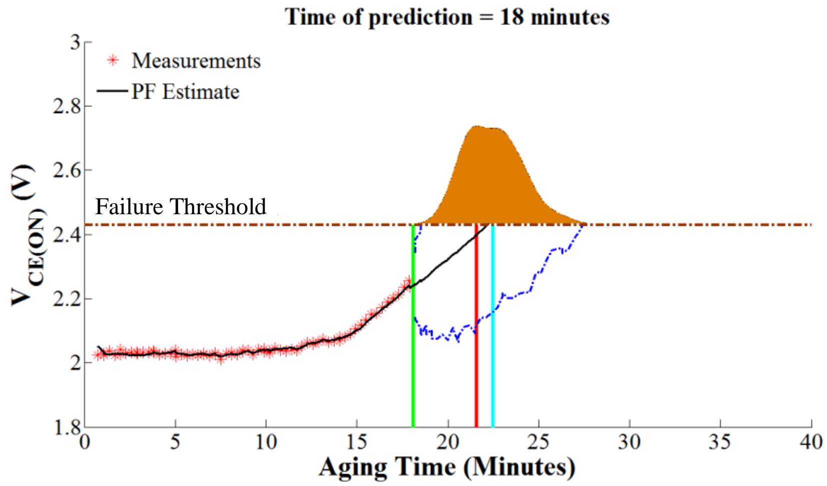

Figure 6-74: Prediction for N= 300 particles and time t= 18 minutes

Predictions for “N7” IGBT after 3, 6, 12 and 18 minutes

Prediction for 10 particles

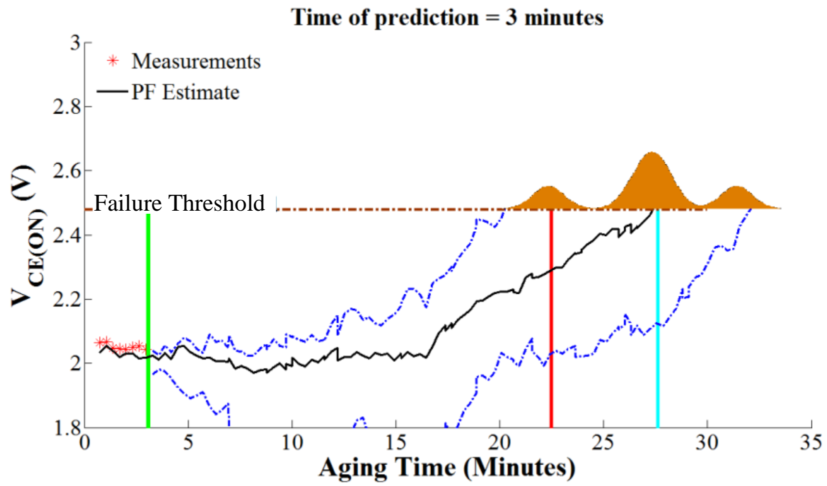

Figure 6-75: Prediction for N= 10 particles and time t= 3 minutes

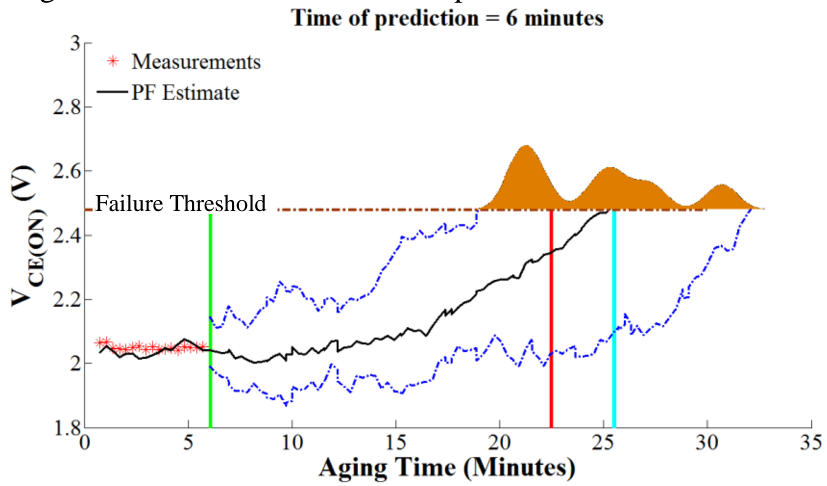

Figure 6-76: Prediction for N= 10 particles and time t= 6 minutes

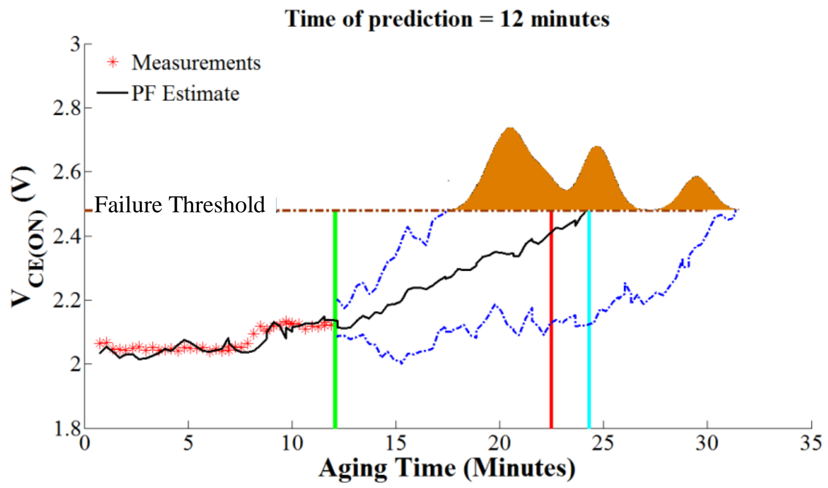

Figure 6-77: Prediction for N= 10 particles and time t= 12 minutes

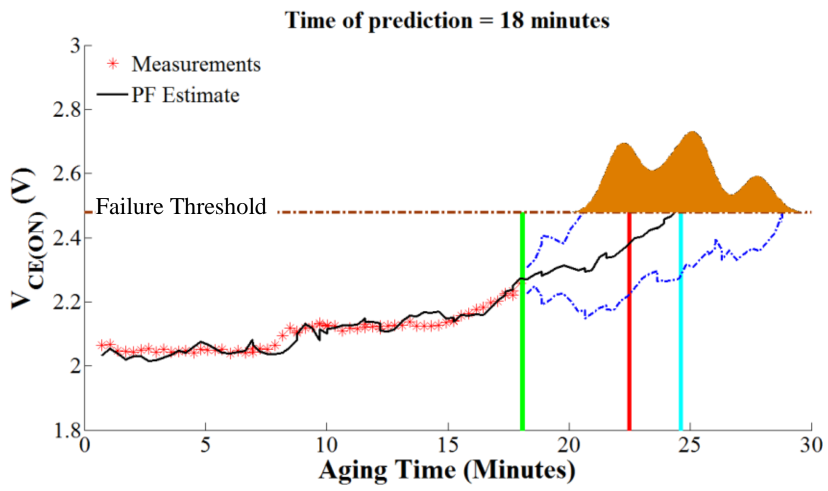

Figure 6-78: Prediction for N= 10 particles and time t= 18 minutes

Prediction for 30 particles

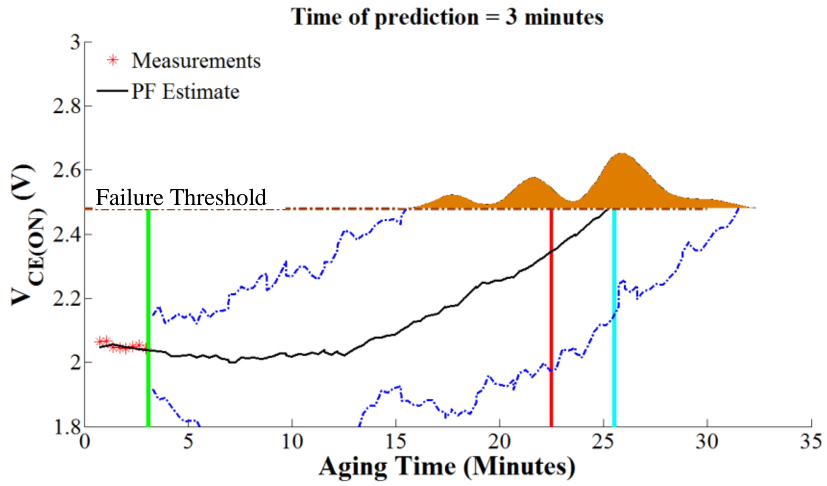

Figure 6-79: Prediction for N= 30 particles and time t= 3 minutes

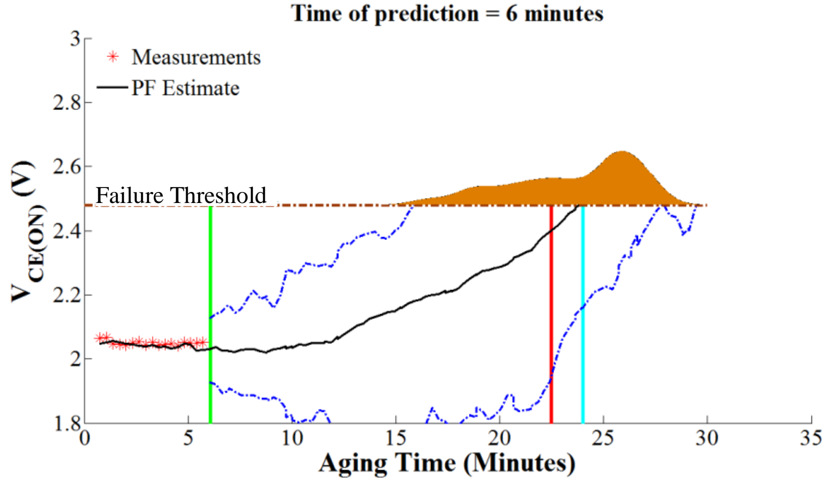

Figure 6-80: Prediction for N= 30 particles and time t= 6 minutes

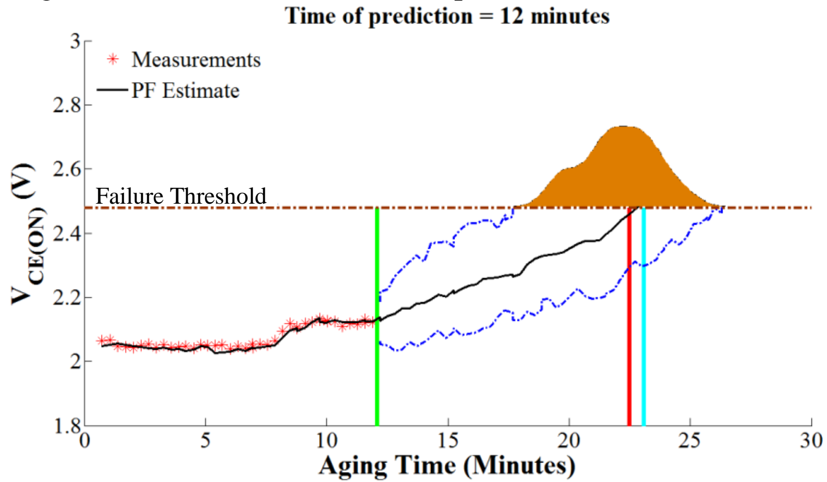

Figure 6-81: Prediction for N= 30 particles and time t= 12 minutes

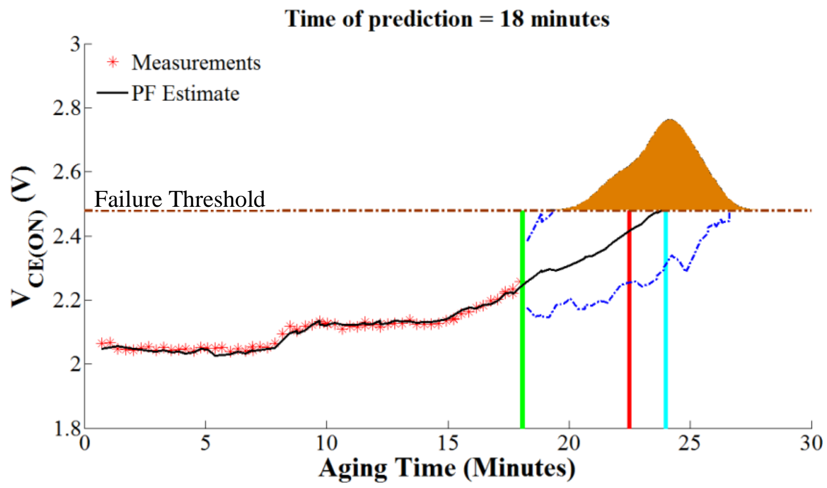

Figure 6-82: Prediction for N= 30 particles and time t= 18 minutes

Prediction for 100 particles

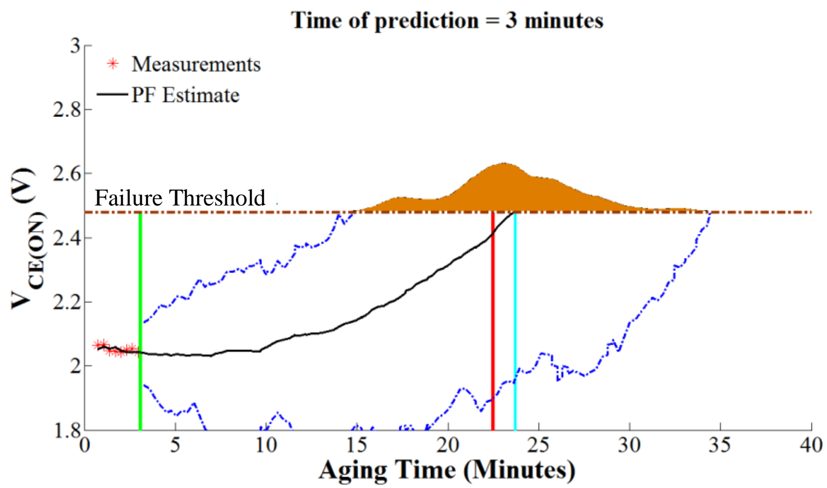

Figure 6-83: Prediction for N= 100 particles and time t= 3 minutes

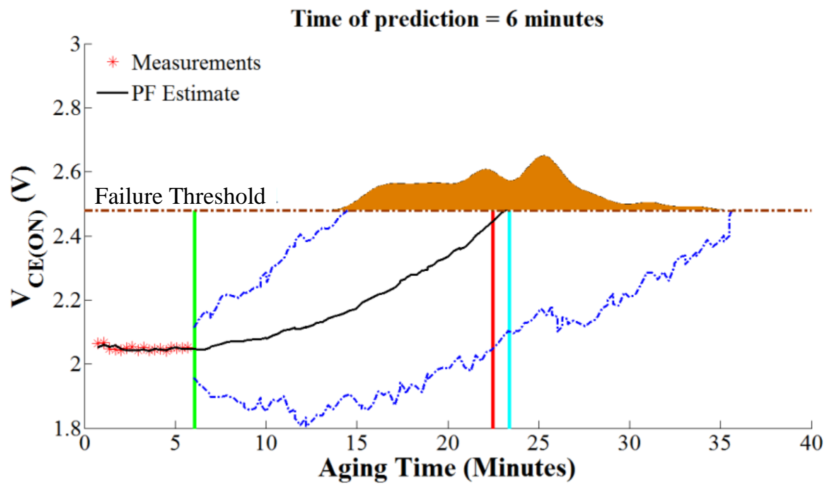

Figure 6-84: Prediction for N= 100 particles and time t= 6 minutes

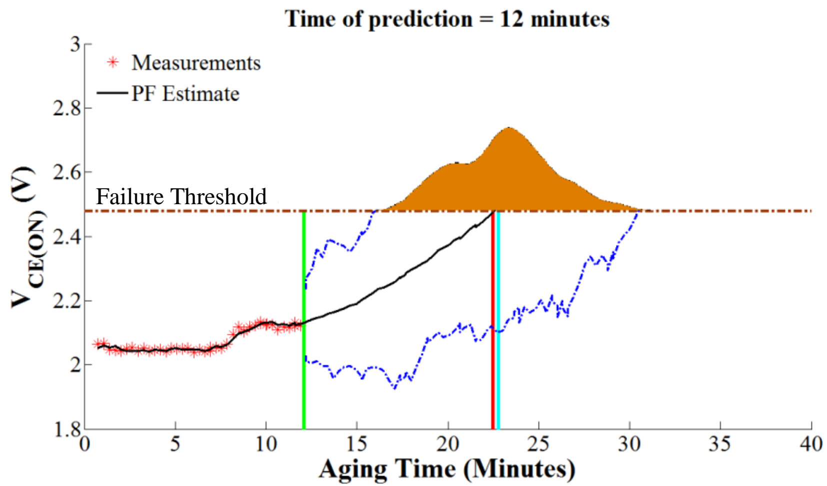

Figure 6-85: Prediction for N= 100 particles and time t= 12 minutes

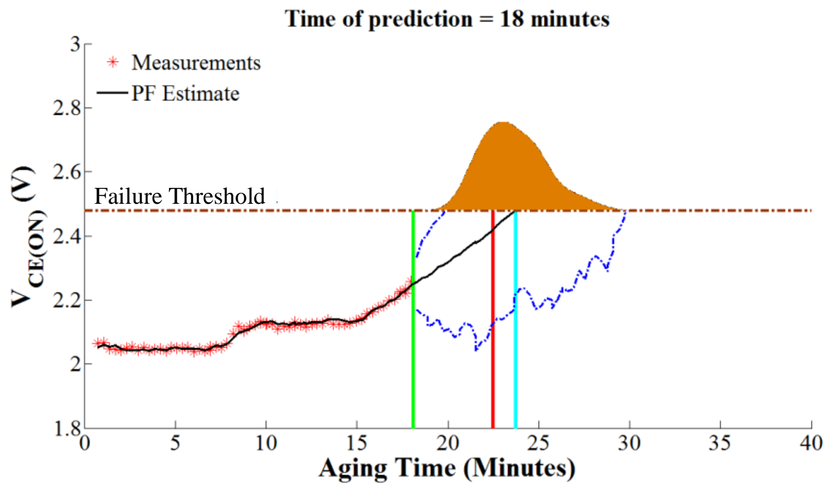

Figure 6-86: Prediction for N= 100 particles and time t= 18 minutes

Prediction for 300 particles

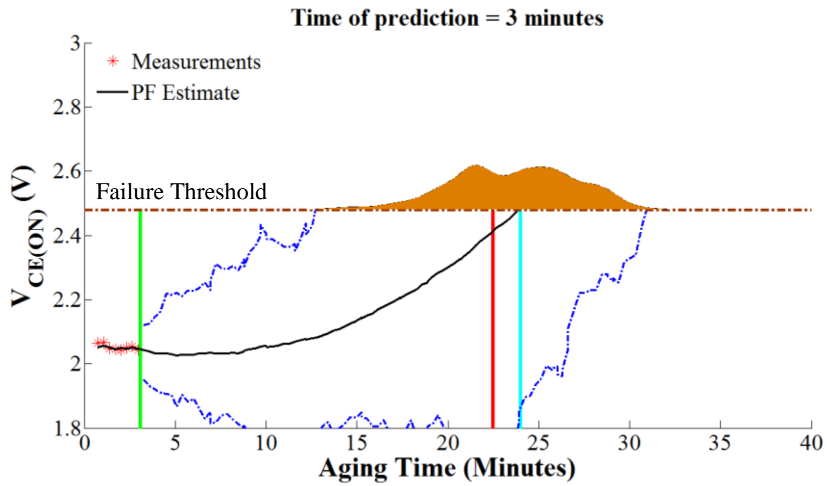

Figure 6-87: Prediction for N= 300 particles and time t= 3 minutes

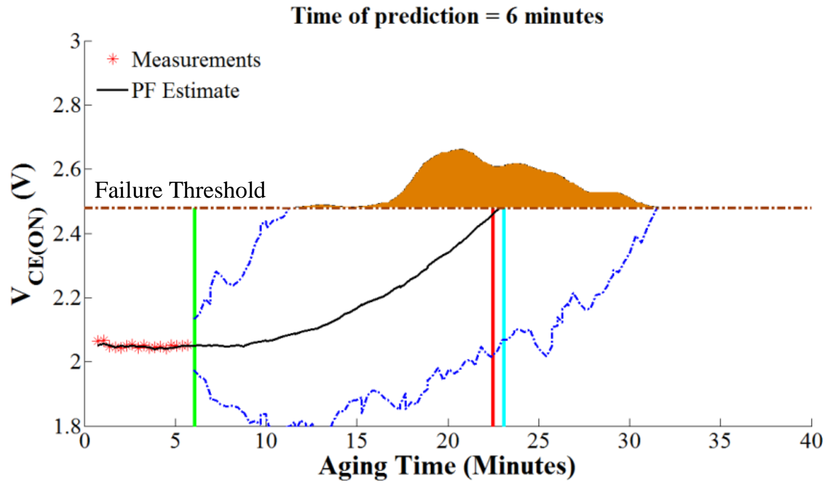

Figure 6-88: Prediction for N= 300 particles and time t= 6 minutes

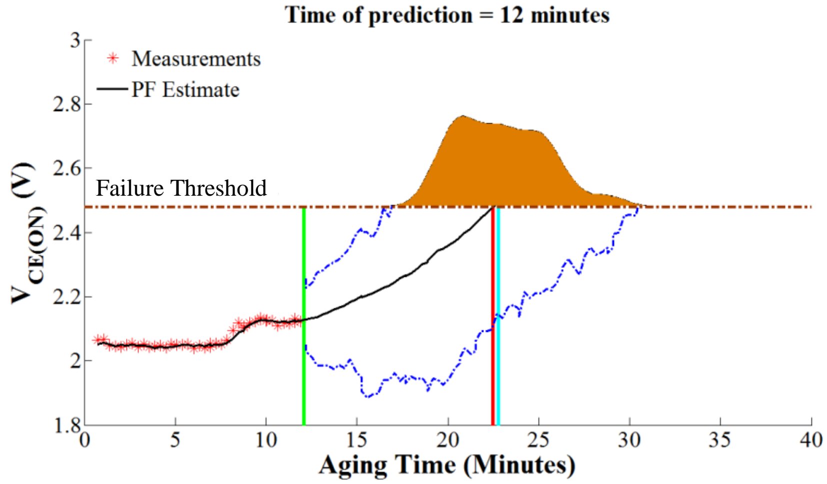

Figure 6-89: Prediction for N= 300 particles and time t= 12 minutes

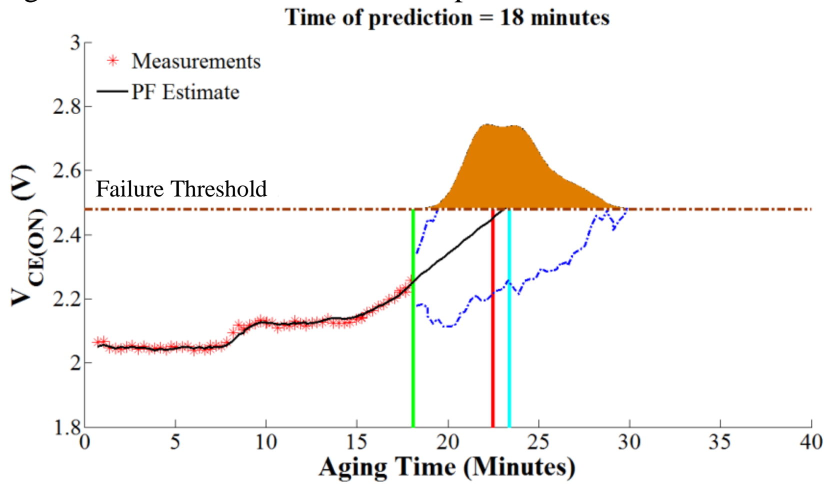

Figure 6-90: Prediction for N= 300 particles and time t= 18 minutes

Predictions for "N8" IGBT after 3, 6, 12 and 18 minutes

Prediction for 10 particles

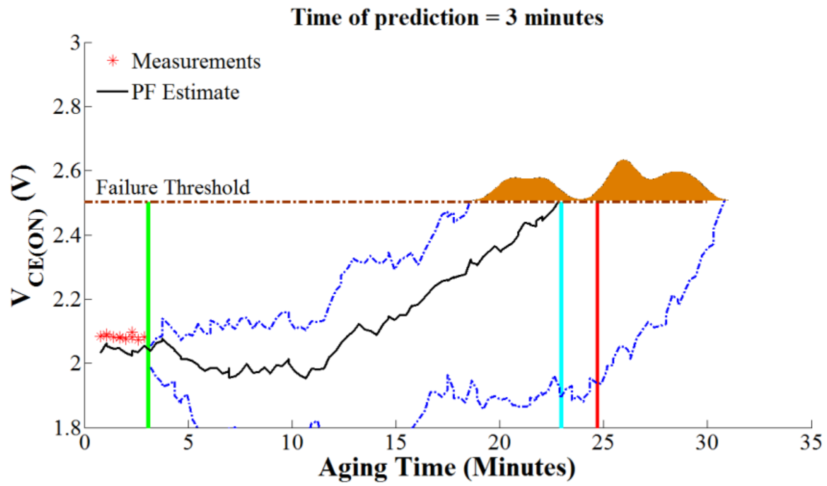

Figure 6-91: Prediction for N= 10 particles and time t= 3 minutes

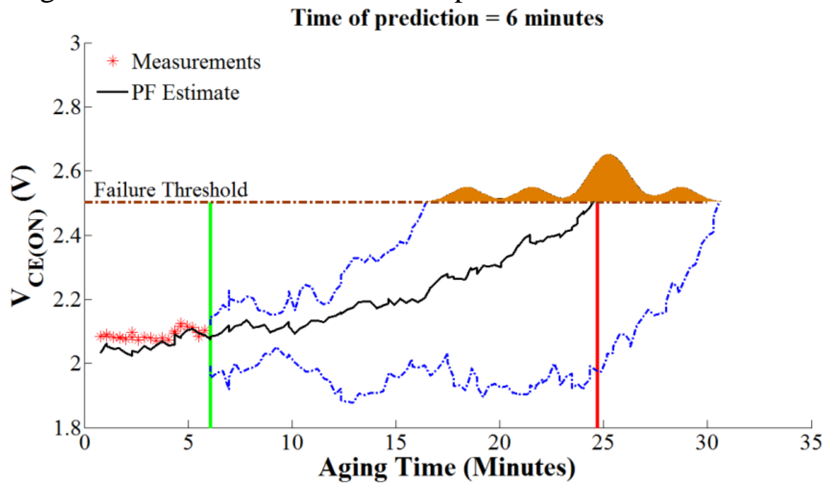

Figure 6-92: Prediction for N= 10 particles and time t= 6 minutes

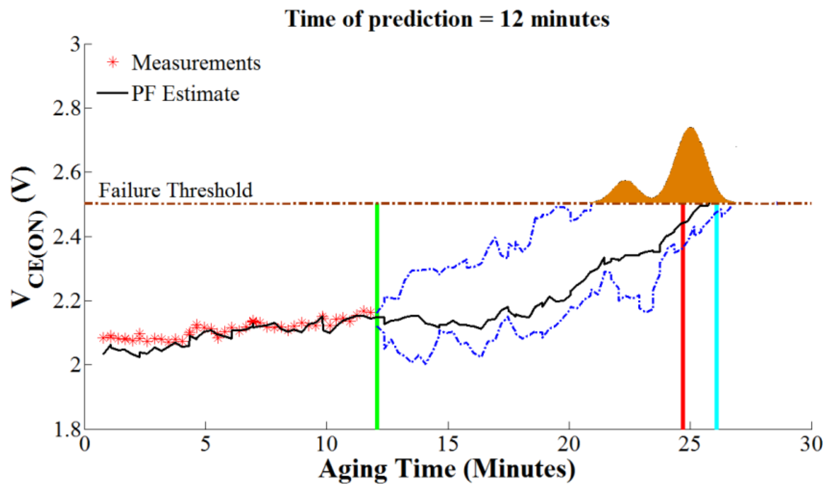

Figure 6-93: Prediction for N= 10 particles and time t= 12 minutes

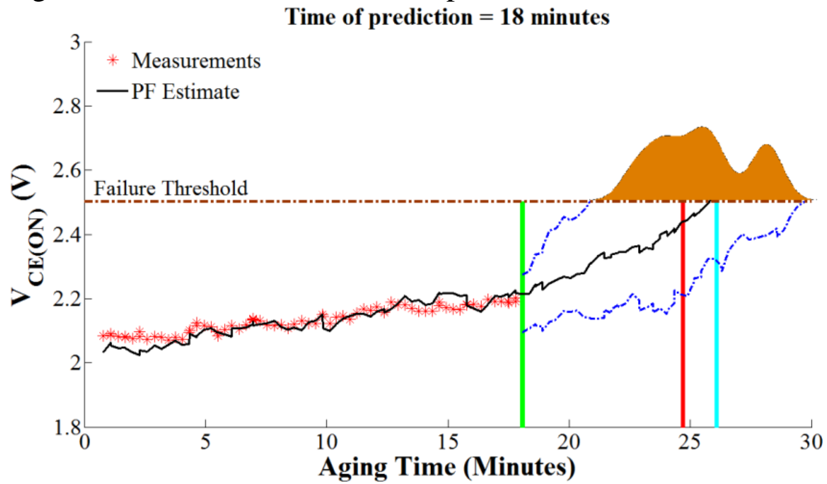

Figure 6-94: Prediction for N= 10 particles and time t= 18 minutes

Prediction for 30 particles

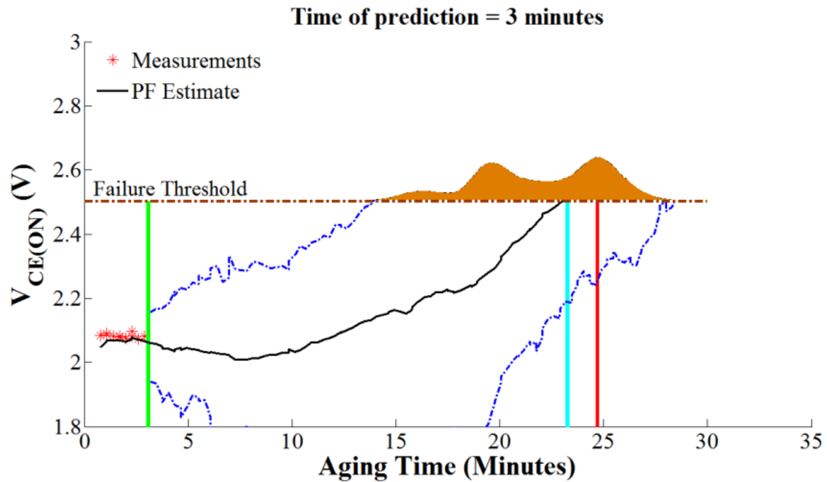

Figure 6-95: Prediction for N= 30 particles and time t= 3 minutes

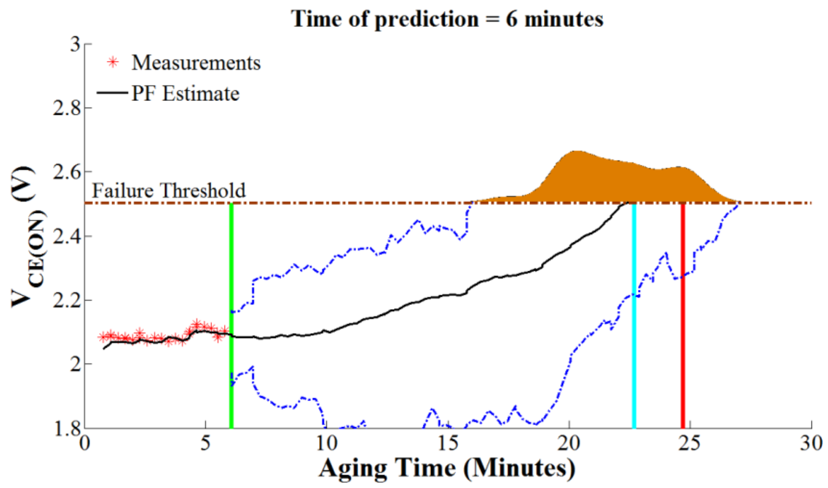

Figure 6-96: Prediction for N= 30 particles and time t= 6 minutes

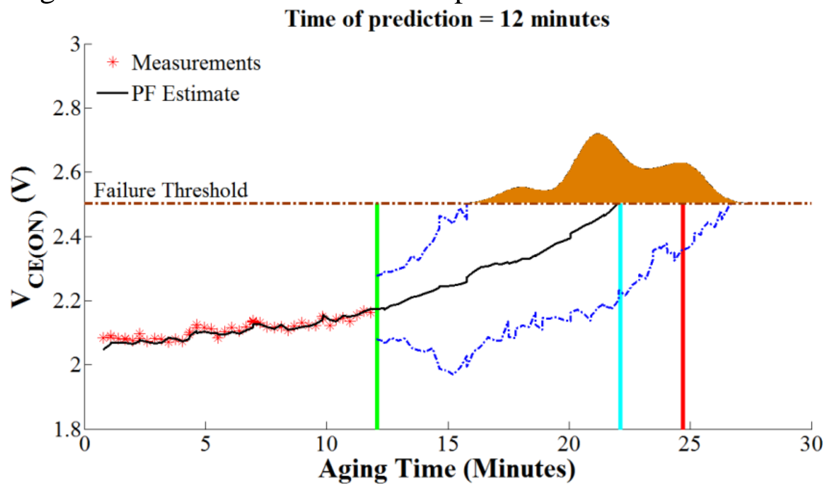

Figure 6-97: Prediction for N= 30 particles and time t= 12 minutes

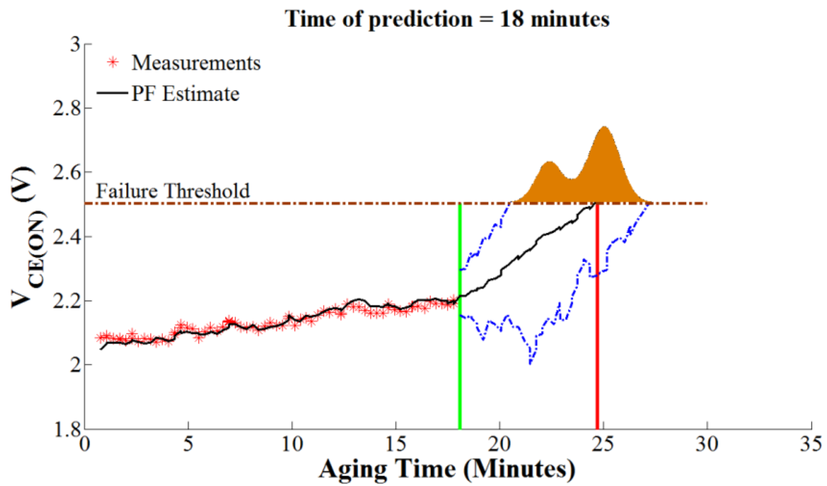

Figure 6-98: Prediction for N= 30 particles and time t= 18 minutes

Prediction for 100 particles

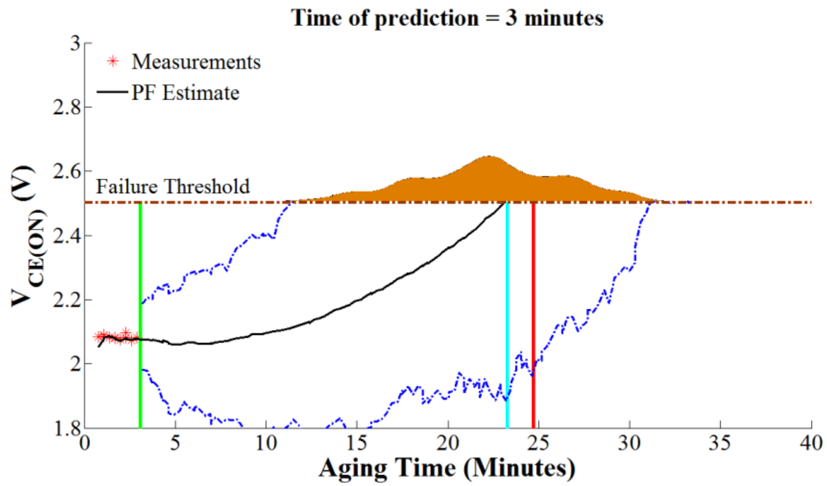

Figure 6-99: Prediction for N= 100 particles and time t= 3 minutes

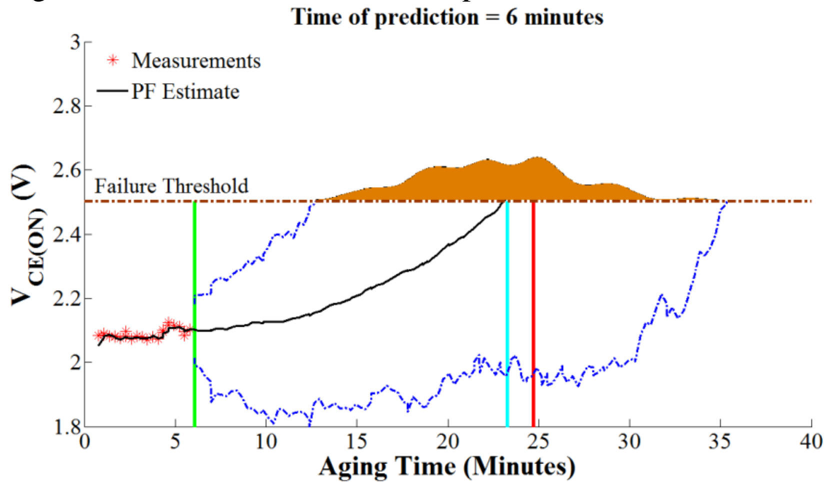

Figure 6-100: Prediction for N= 100 particles and time t= 6 minutes

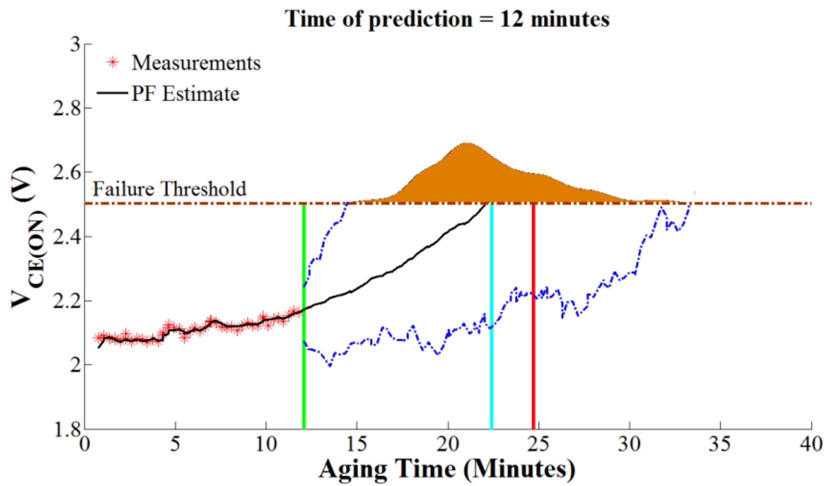

Figure 6-101: Prediction for N= 100 particles and time t= 12 minutes

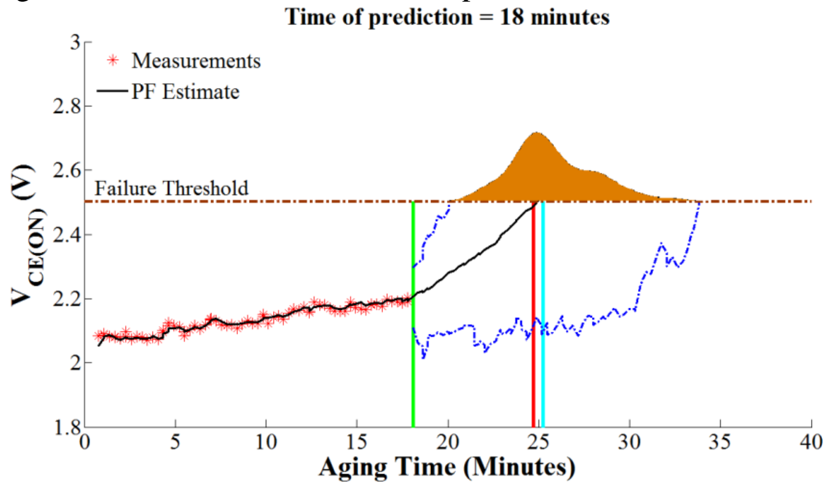

Figure 6-102: Prediction for N= 100 particles and time t= 18 minutes

Prediction for 300 particles

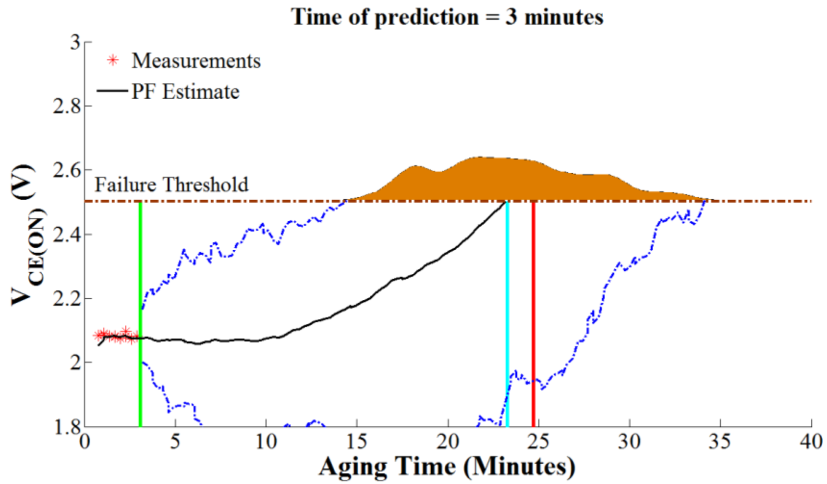

Figure 6-103: Prediction for N= 300 particles and time t= 3 minutes

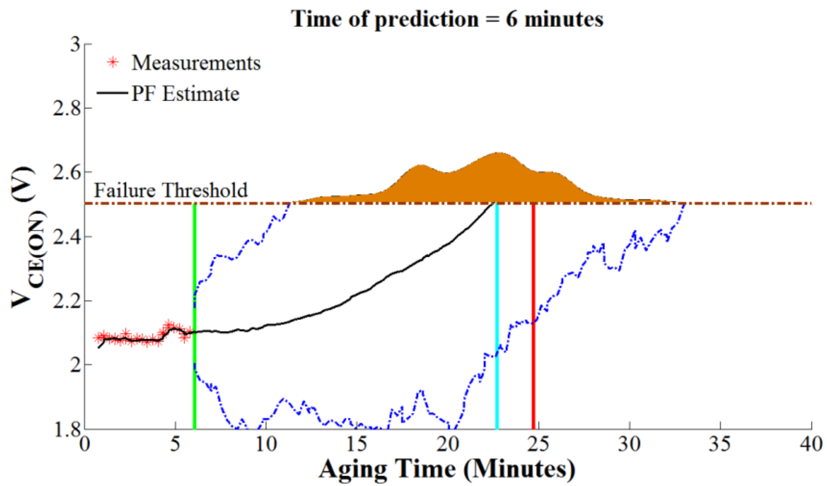

Figure 6-104: Prediction for N= 300 particles and time t= 6 minutes

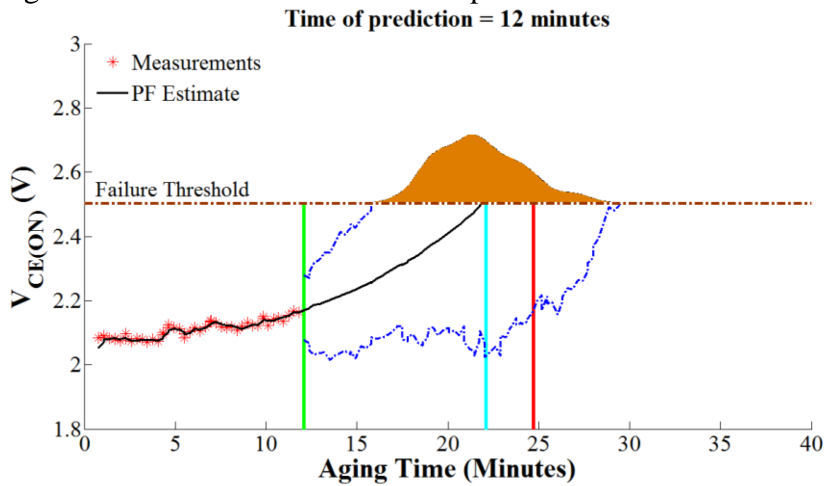

Figure 6-105: Prediction for N= 300 particles and time t= 12 minutes

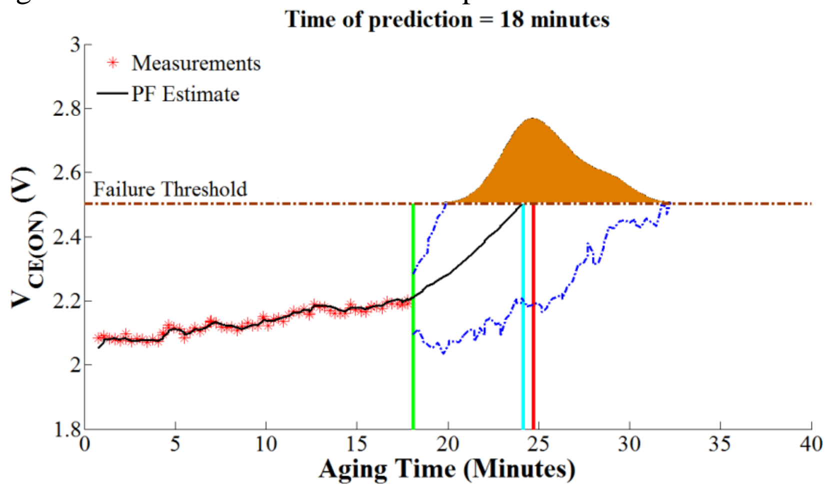

Figure 6-106: Prediction for N= 300 particles and time t= 18 minutes

Predictions for "N9" IGBT after 3, 6, 12 and 18 minutes

Prediction for 10 particles

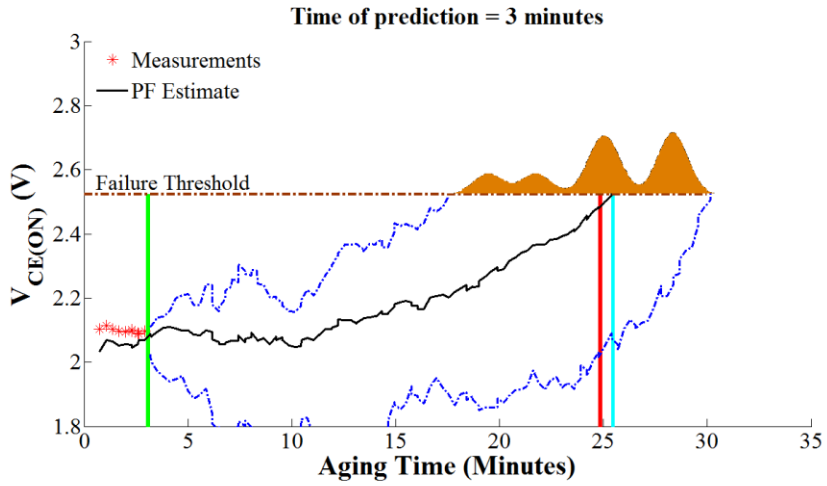

Figure 6-107: Prediction for N= 10 particles and time t= 3 minutes

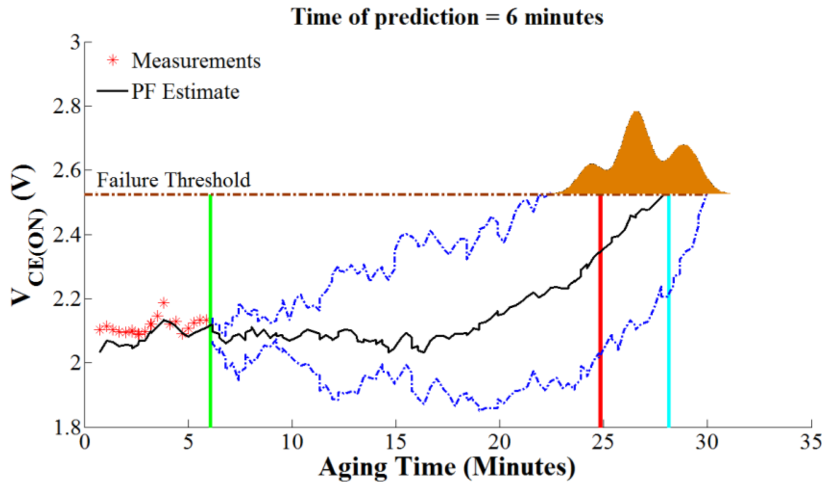

Figure 6-108: Prediction for N= 10 particles and time t= 6 minutes

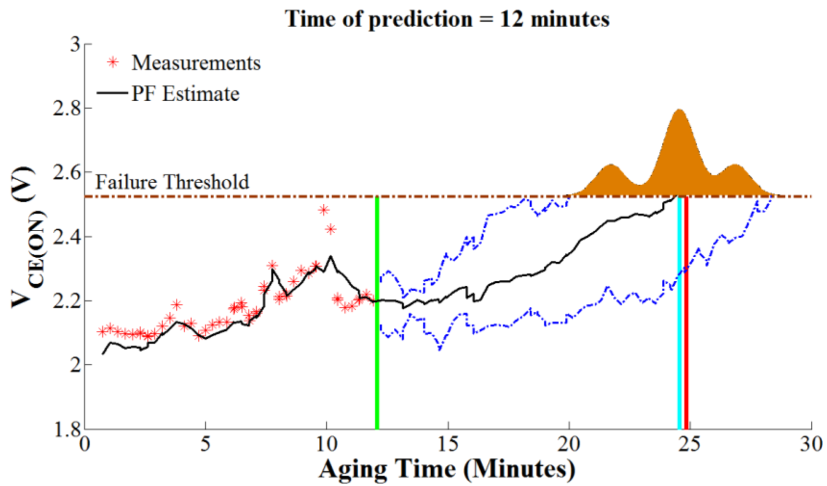

Figure 6-109: Prediction for N= 10 particles and time t= 12 minutes

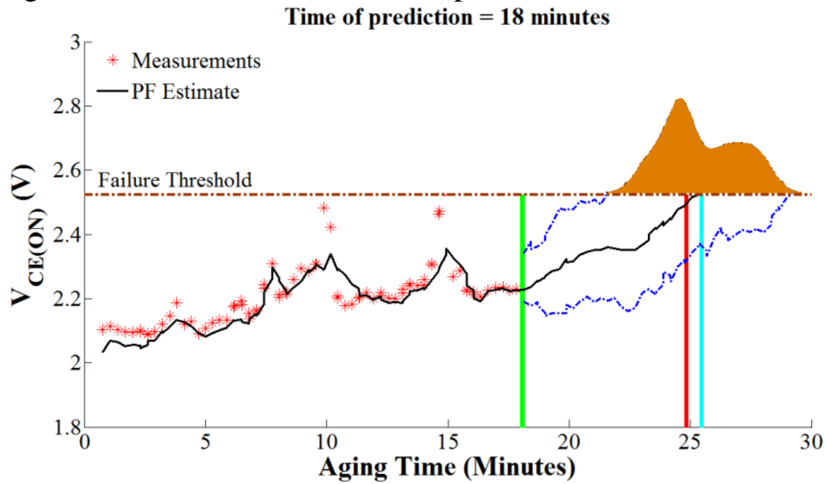

Figure 6-110: Prediction for N= 10 particles and time t= 18 minutes

Prediction for 30 particles

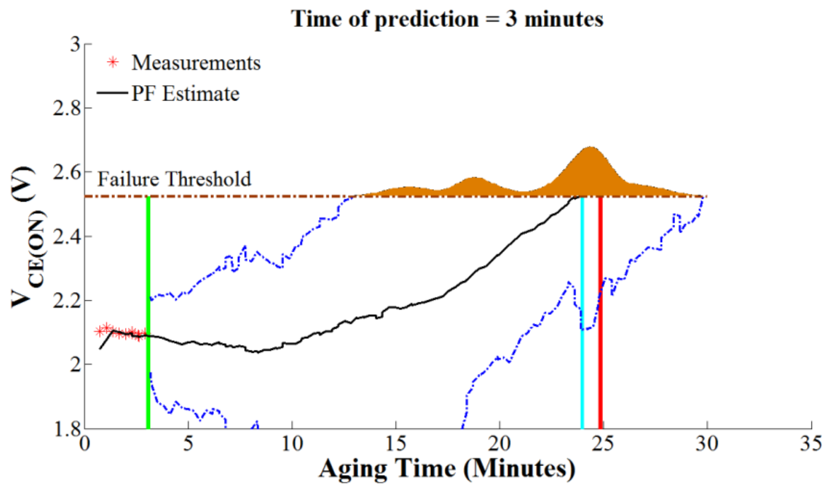

Figure 6-111: Prediction for N= 30 particles and time t= 3 minutes

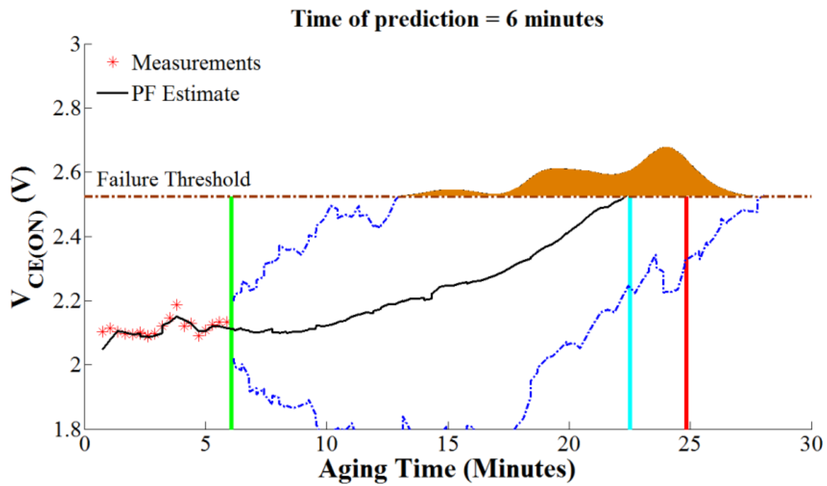

Figure 6-112: Prediction for N= 30 particles and time t= 6 minutes

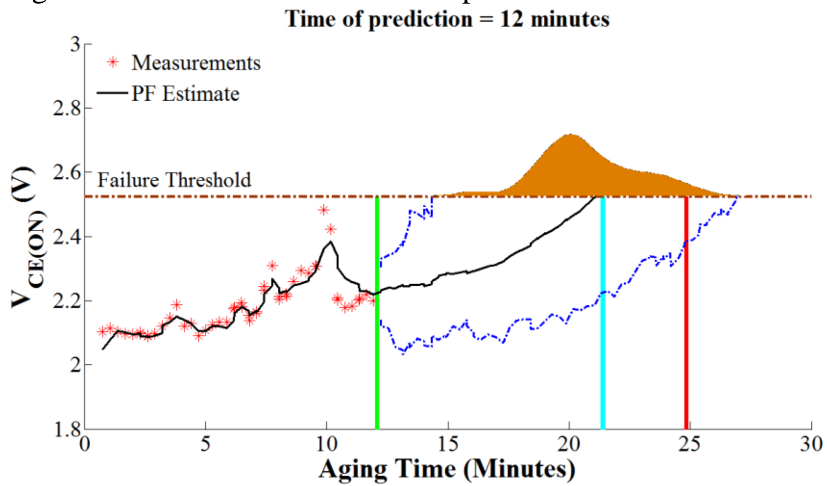

Figure 6-113: Prediction for N= 30 particles and time t= 12 minutes

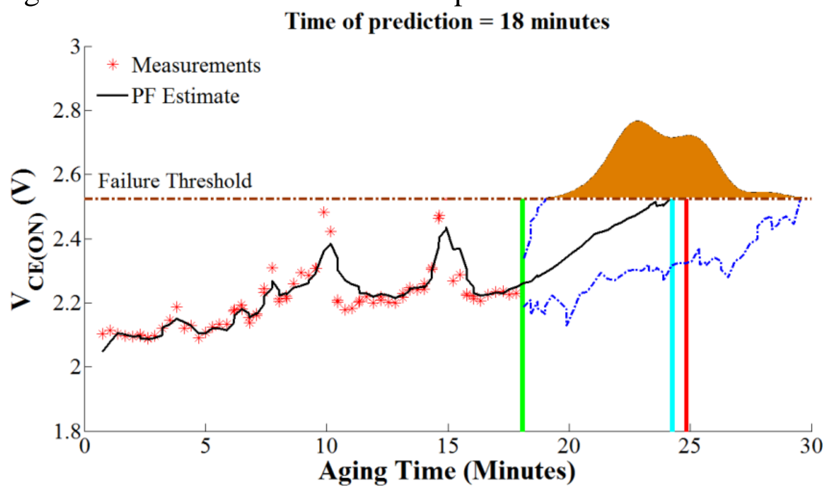

Figure 6-114: Prediction for N= 30 particles and time t= 18 minutes

Prediction for 100 particles

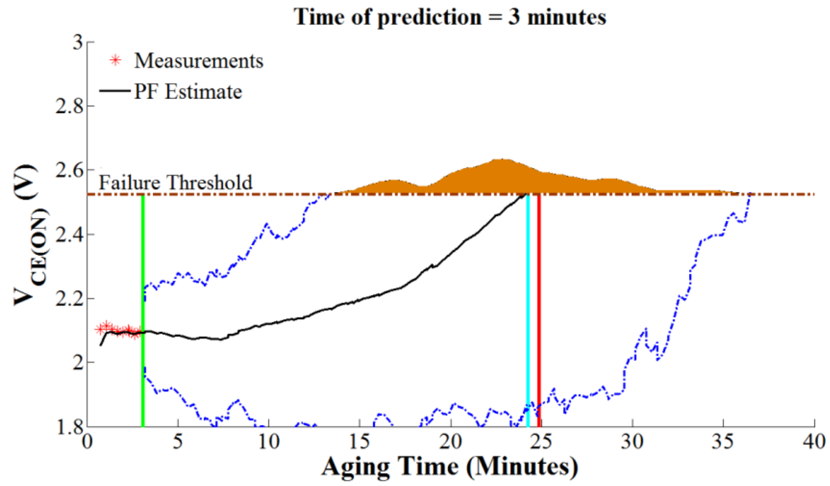

Figure 6-115: Prediction for N= 100 particles and time t= 3 minutes

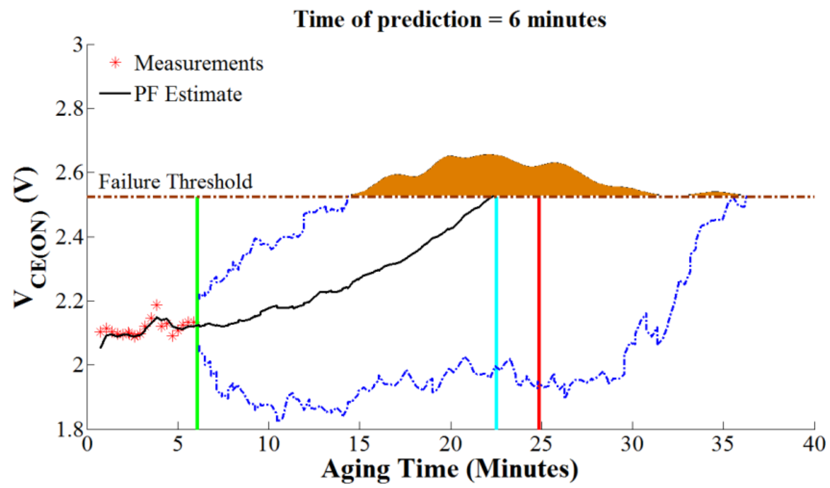

Figure 6-116: Prediction for N= 100 particles and time t= 6 minutes

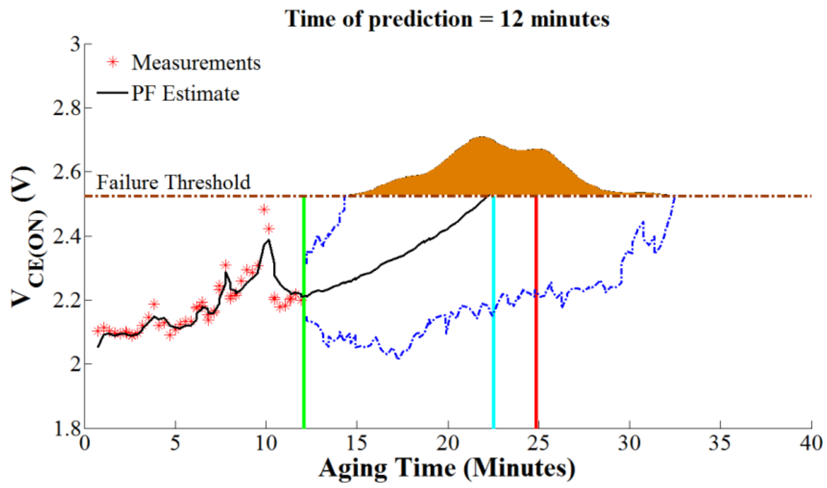

Figure 6-117: Prediction for N= 100 particles and time t= 12 minutes

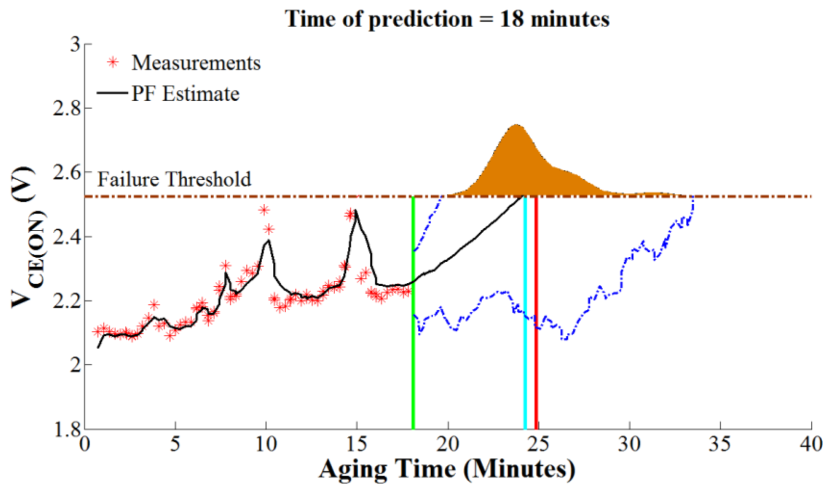

Figure 6-118: Prediction for N= 100 particles and time t= 18 minutes

Prediction for 300 particles

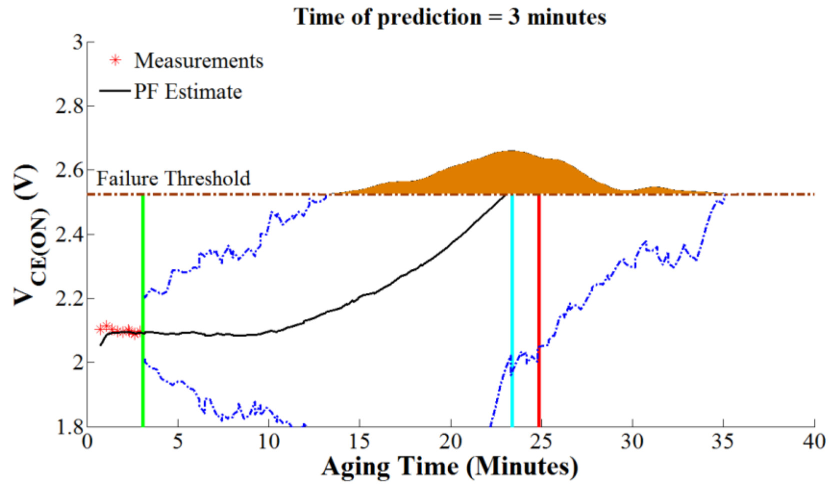

Figure 6-119: Prediction for N= 300 particles and time t= 3 minutes

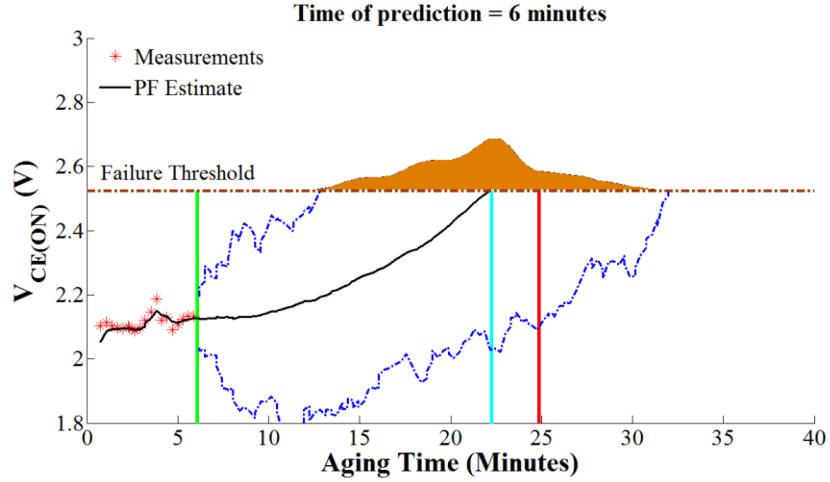

Figure 6-120: Prediction for N= 300 particles and time t= 6 minutes

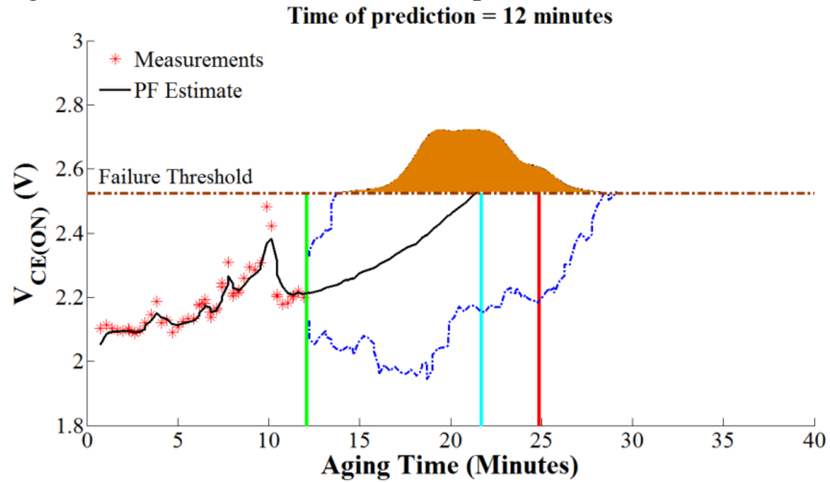

Figure 6-121: Prediction for N= 300 particles and time t= 12 minutes

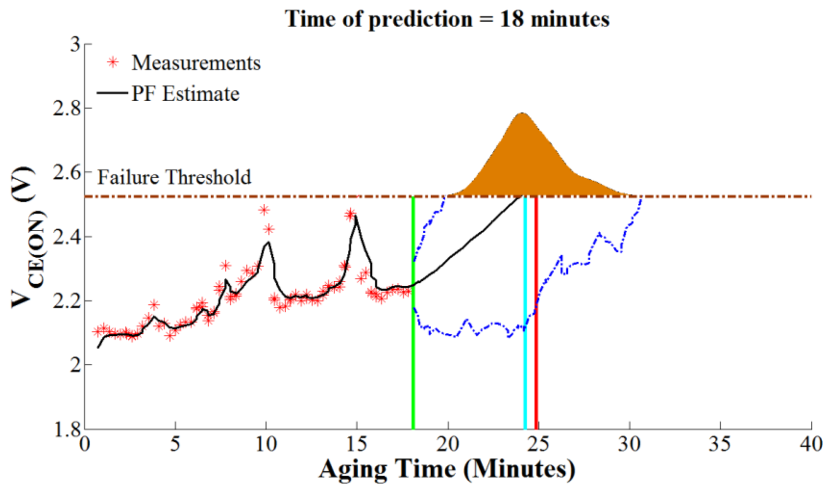

Figure 6-122: Prediction for N= 300 particles and time t= 18 minutes

Predictions for "N10" IGBT after 3, 6, 12 and 18 minutes

Prediction for 10 particles

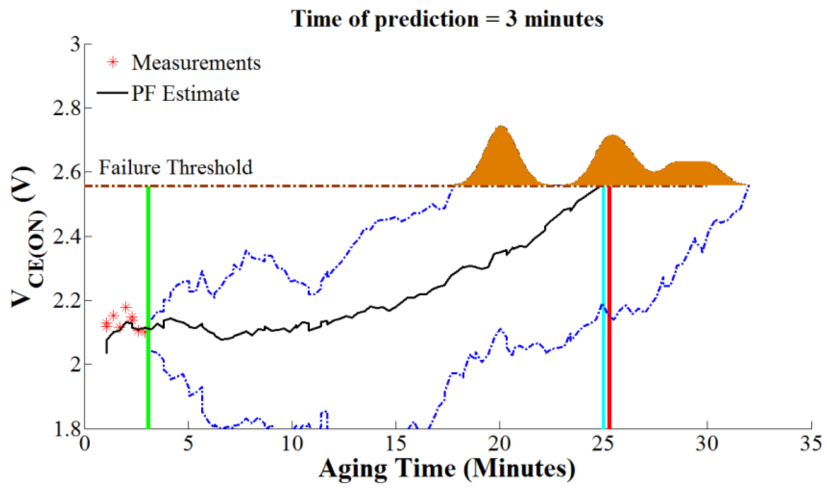

Figure 6-123: Prediction for N= 10 particles and time t= 3 minutes

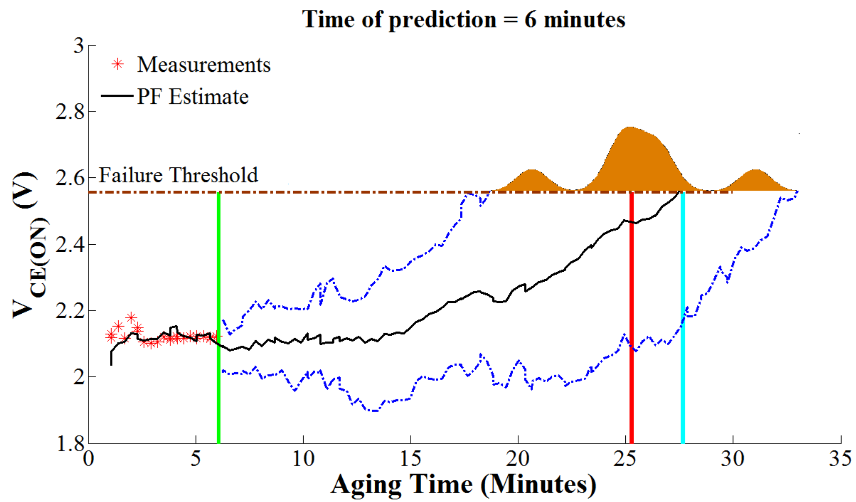

Figure 6-124: Prediction for N= 10 particles and time t= 6 minutes

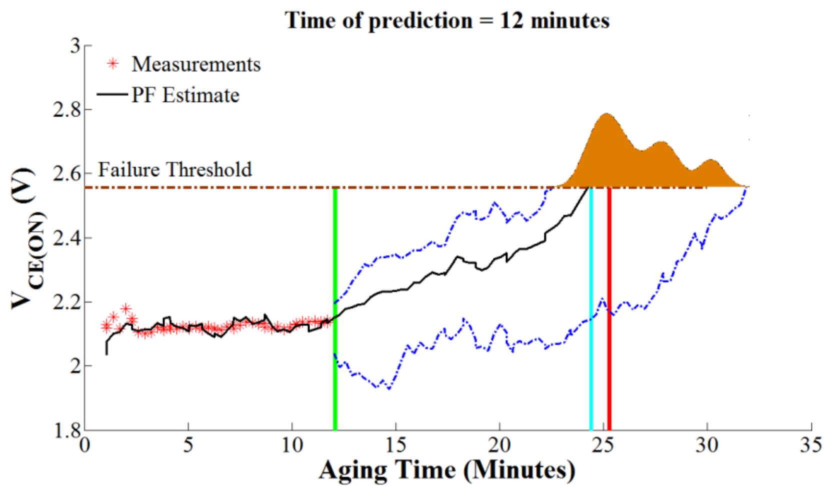

Figure 6-125: Prediction for N= 10 particles and time t= 12 minutes

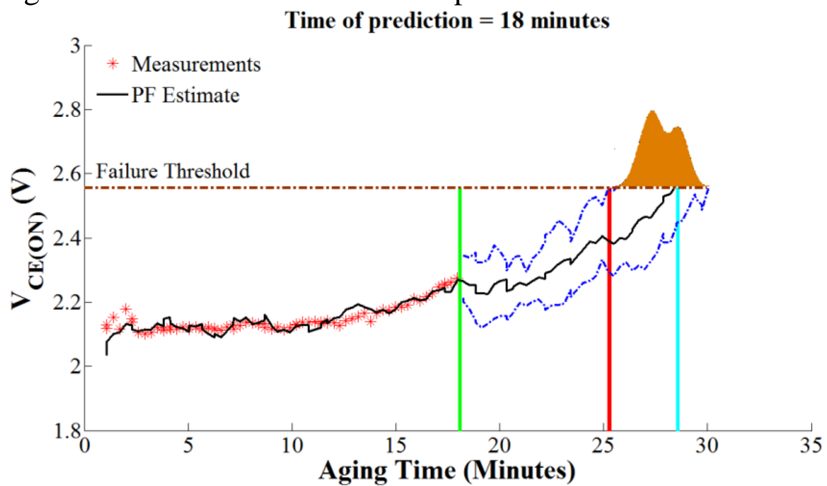

Figure 6-126: Prediction for N= 10 particles and time t= 18 minutes

Prediction for 30 particles

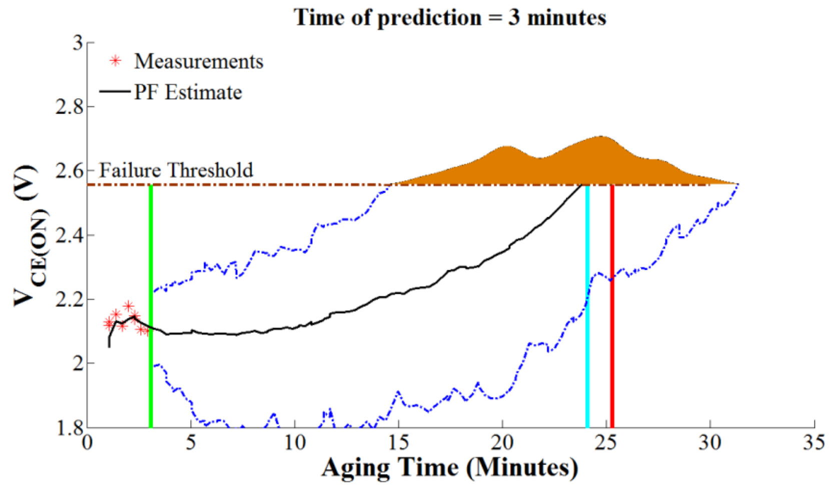

Figure 6-127: Prediction for N= 30 particles and time t= 3 minutes

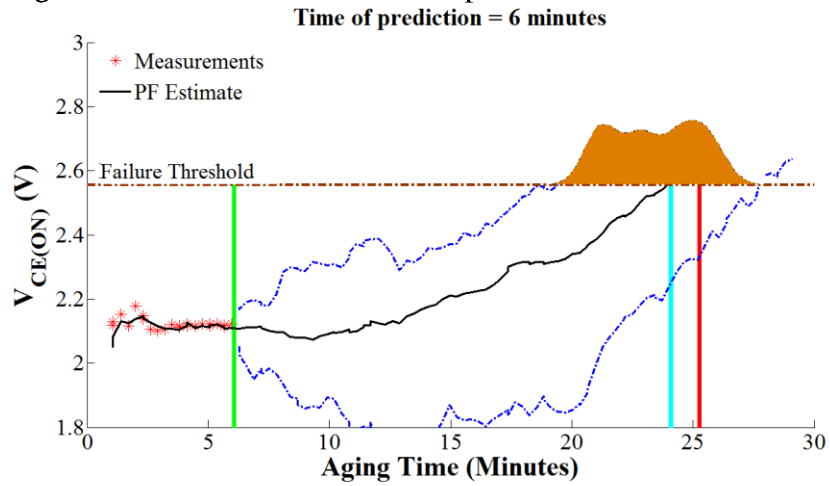

Figure 6-128: Prediction for N= 30 particles and time t= 6 minutes

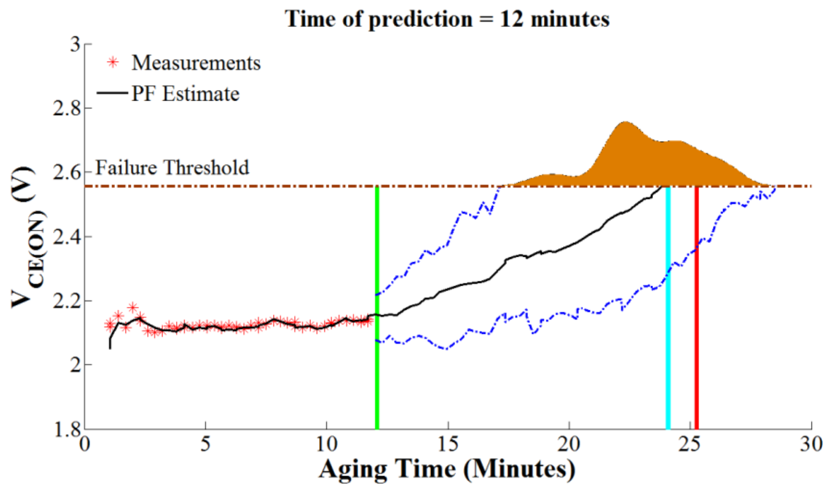

Figure 6-129: Prediction for N= 30 particles and time t= 12 minutes

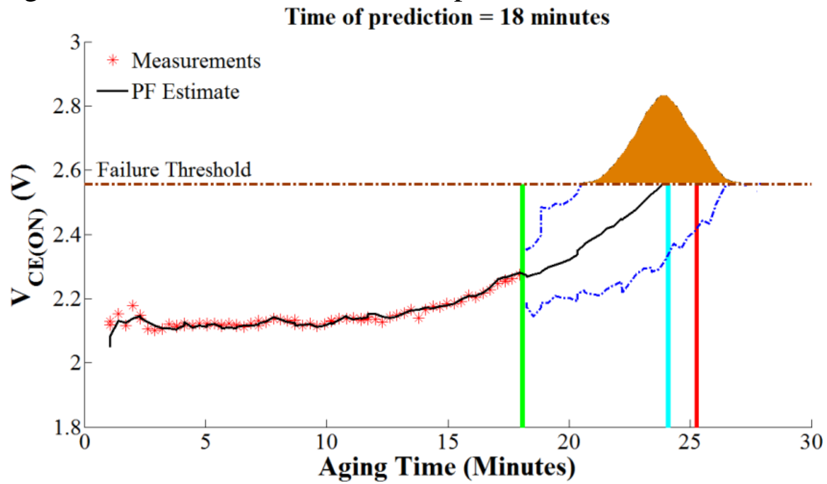

Figure 6-130: Prediction for N= 30 particles and time t= 18 minutes

Prediction for 100 particles

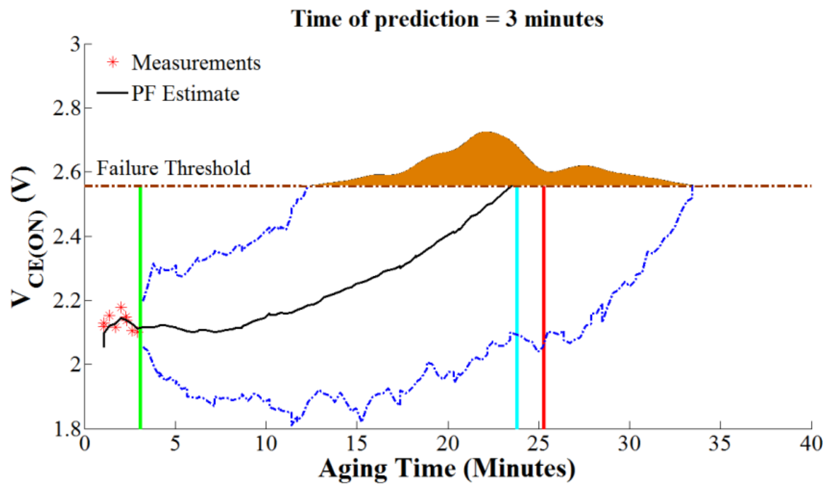

Figure 6-131: Prediction for N= 100 particles and time t= 3 minutes

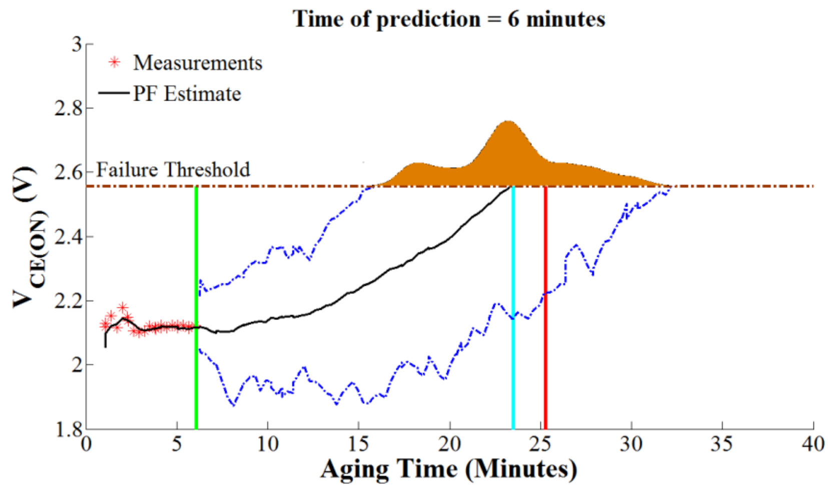

Figure 6-132: Prediction for N= 100 particles and time t= 6 minutes

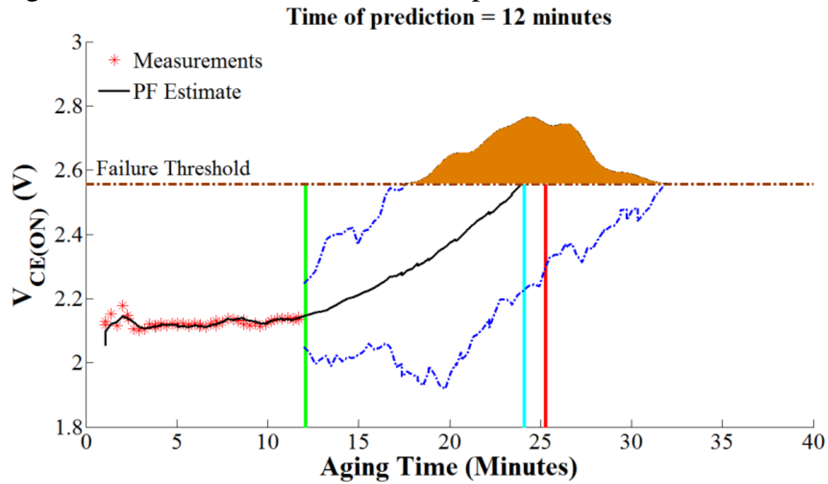

Figure 6-133: Prediction for N= 100 particles and time t= 12 minutes

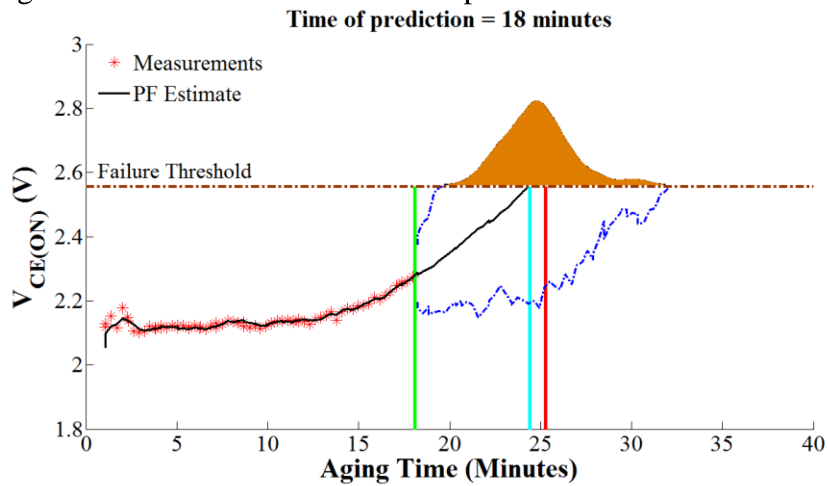

Figure 6-134: Prediction for N= 100 particles and time t= 18 minutes

Prediction for 300 particles

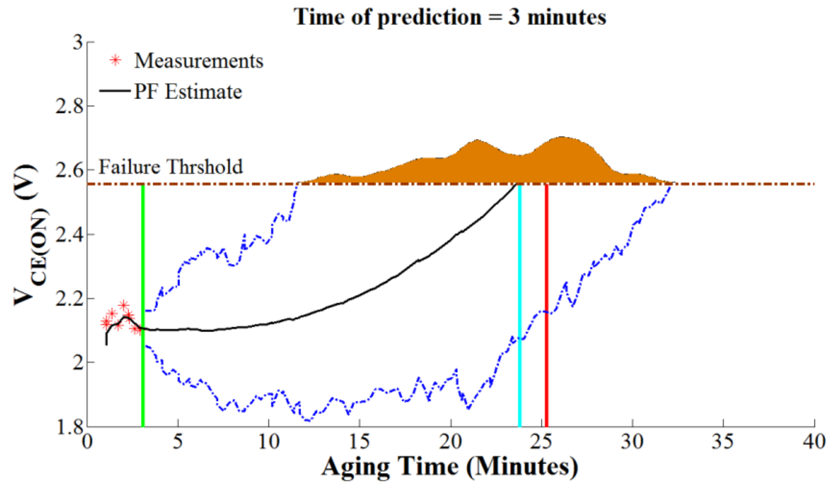

Figure 6-135: Prediction for N= 300 particles and time t= 3 minutes

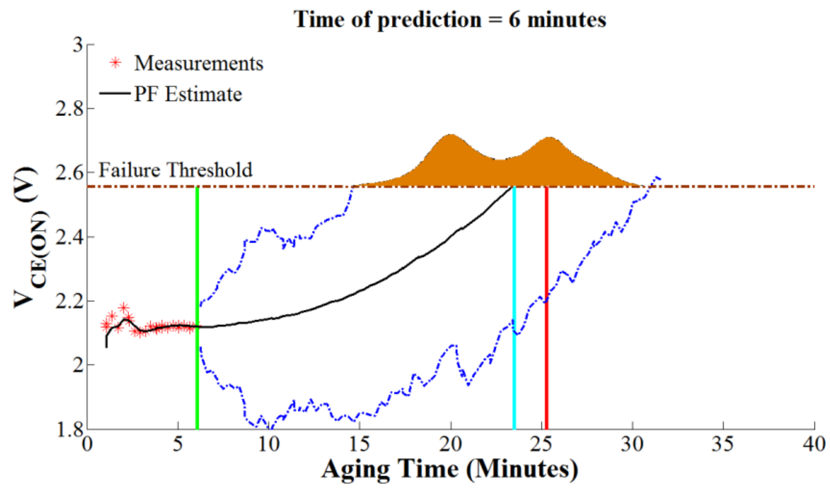

Figure 6-136: Prediction for N= 300 particles and time t= 6 minutes

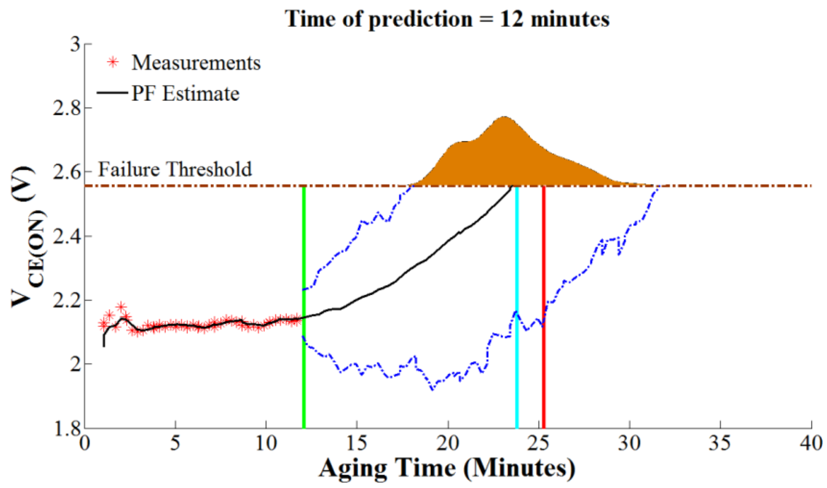

Figure 6-137: Prediction for N= 300 particles and time t= 12 minutes

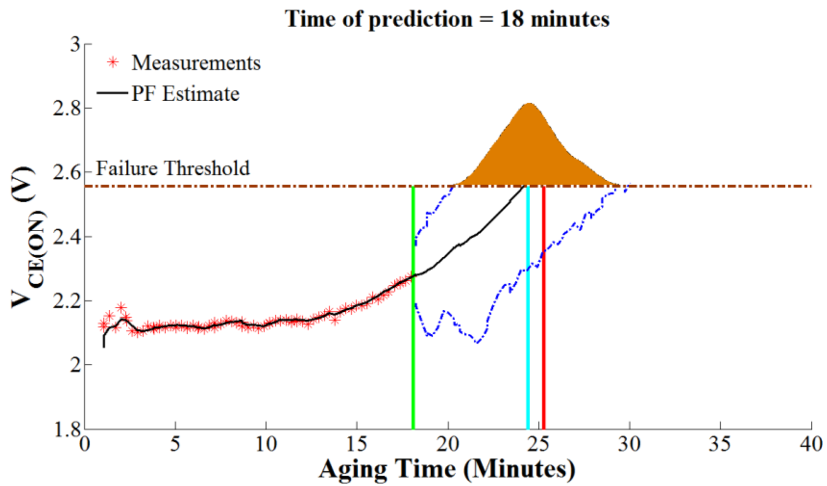

Figure 6-138: Prediction for N= 300 particles and time t= 18 minutes

Bibliography

[1] B. Baliga, "Power Semiconductor Devices," Springer, New York, 2008.

[2] B. Lu and S. Sharma, "A Literature Review of IGBT Fault Diagnostic and Protection Methods for Power Inverters," IEEE Transactions on Industry Applications, vol.45, No. 5, pp.1770-1777, 2009.

[3] M. Arifujjaman, M. Iqbal, and J. Quaicoe, "Reliability Analysis of Grid Connected Small Wind Turbine Power Electronics," Applied Energy, vol. 86, pp. 1617-1623, 2009.

[4] D. Hirschmann, D. Tissen, S. Schroder, and R. W. De Doncker, "Reliability Prediction for Inverters in Hybrid Electrical Vehicles," IEEE Transactions on Power Electronics, vol.22, pp.2511-2517, 2007.

[5] X. Perpina, J. Serviere, X. Jorda, A. Fauquet, S. Hidalgo, J. Urresti-Ibanez, J. Rebollo, and M. Mermet-Guyennet, "IGBT Module Failure Analysis in Railway Applications," Microelectronics Reliability, vol. 48, pp. 1427-1431, 2008.

[6] M. Pecht, "Prognostics and Health Management of Electronics," Wiley-Interscience, New York, NY, 2008.

[7] V. Khanna, "IGBT: Theory and Design," IEEE Press/Wiley Interscience, Hoboken, NJ, 2003.

[8] J. Baliga, "Enhancement- and Depletion-Mode Vertical-Channel M.O.S. Gated Thyristors," Electronics Letters, vol.15, no.20, pp.645-647, 1979.

[9] J. Plummer and B. Scharf, "Insulated-Gate Planar Thyristors: I—Structure and Basic Operation," IEEE Transactions on Electron Devices, vol.27, no.2, pp. 380- 387, 1980.

[10] J. Plummer and B. Scharf, "Insulated-Gate Planar Thyristors: II—Quantitative Modeling," IEEE Transactions on Electron Devices, vol.27, no.2, pp. 387- 394, 1980.

[11] H. Becke and C. Wheatley, "Power MOSFET with an Anode Region," US Patent No: 4,364,073, 1982.

[12] J. Baliga, "Power Semiconductor Devices," PWS Publishing Company, Boston, Massachusetts, 1996.

[13] M. Pecht and R. Jaai, “A Prognostics and Health Management Roadmap for Information and Electronics-Rich Systems, Microelectronics Reliability, vol. 50, pp. 317-323, 2010.

[14] G. Vachtsevanos, F. Lewis, M. Roemer, A. Hess, and B. Wu, “Intelligent Fault Diagnosis and Prognosis for Engineering Systems,” John Wiley & Sons, Hoboken, New Jersey, 2006.

[15] J. Gu, D. Barker and M. Pecht, “Prognostics Implementation of Electronics under Vibration Loading,” Microelectronics Reliability, vol. 47, Issue 12, pp. 1849-1856, 2007.

[16] B. Saha, K. Goebel, S. Poll, and J. Christophersen, “Prognostics Methods for Battery Health Monitoring Using a Bayesian Framework,” IEEE Transactions on Instrumentation and Measurement, vol. 58, pp.291-296, 2009.

[17] D. Goodman, “Prognostic Methodology for Deep Submicron Semiconductor Failure Modes,” IEEE Transactions on Components and Packaging Technologies, Vol. 24, pp. 109-111, 2001.

[18] N. Vichare and M. Pecht, “Prognostics and Health Management of Electronics,” IEEE Transactions on Components and Packaging Technologies, Vol. 29, pp. 222-229, 2006.

[19] S. Kumar, V. Sotiris and M. Pecht, “Health Assessment of Electronic Products using Mahalanobis Distance and Projection Pursuit Analysis,” International Journal of Computer Information, System Science and Engineering, Vol. 2, No. 4, pp. 242-250, 2008.

[20] Y. Xiong, Xu. Cheng, Z. Shen, C. Mi, H. Wu, and V. Garg, “Prognostic and Warning System for Power-Electronic Modules in Electric, Hybrid Electric, and Fuel-Cell Vehicles,” IEEE Transactions on Industrial Electronics, Vol. 55, No. 6, pp. 2268-2276, 2008.

[21] A. Ginart, D. Brown, P. Kalgren and M. Roemer, “Online Ringing Characterization as a Diagnostic Technique for IGBTs in Power Drives,” IEEE Transactions on Instrumentation and Measurement, Vol.58, No.7, pp.2290-2299, 2009.

[22] H. Lu, C. Bailey and C. Yin, “Design for reliability of power electronics modules,” Microelectronics Reliability, vol. 49, pp, 1250-1255, 2009.

[23] A. Oukaour, B. Tala-Ighil, B. Pouderoux, M. Tounsi, M. Bouarroudj-Berkani, S. Lefebvre and B. Boudart, “Ageing Defect Detection on IGBT Power Modules by Artificial Training Methods Based on Pattern Recognition,” Microelectronics Reliability, In Press, Corrected Proof, Available online 24 September 2010.

[24] B. Saha, J. Celaya, P. Wysocki, and K. Goebel, "Towards Prognostics For Electronics Components," Proceedings of the IEEE Aerospace Conference, Big Sky, MT, pp.1-7, 2009.

[25] G. Sonnenfeld, K. Goebel and J. Celaya, "An Agile Accelerated Aging, Characterization and Scenario Simulation System for Gate Controlled Power Transistors," Proceedings of the IEEE Autotest Conference, pp. 208-215, 2008.

[26] P. Cova, and F. Fantini, “On the Effect of Power Cycling Stress on IGBT Modules,” Microelectronics Reliability, vol. 38, pp. 1347-1352, 1998.

[27] B. Farokhzad, P. Türkes, E. Wolfgang and K. Goser, “Reliability Indicators for Lift-Off of Bond Wires in IGBT Power Modules,” Microelectronics Reliability, vol. 36, pp. 1863–1866, 1996.

[28] W. Wu, M. Held, P. Jacob, P. Scacco, A. Birolini, “Investigation on the Long Term Reliablity of Power IGBT Modules,” Proceedings of the International Symposium on Power Semiconductor Devices and ICs, pp. 443–448, 1995.

[29] F. Auerbach and A. Lenniger, “Power Cycling Stability of IGBT Modules,” Proceedings of the IEEE Industry Applications Society Annual Meeting, pp. 1248-1252, 1997.

[30] H. Ye, M. Lin and C. Basaran, “Failure Modes and FEM Analysis of Power Electronic Packaging,” Finite Elements in Analysis and Design, vol. 38, pp. 601–612, 2002.

[31] M. Bouarroudj, Z. Khatir, J.P. Ousten, F. Badel, L. Dupont, S. Lefebvre, “Degradation Behavior of 600 V-200 A IGBT Modules under Power Cycling and High Temperature Environment Conditions, “ Microelectronics Reliability, vol. 47, pp. 1719-1724, 2007.

[32] A. Morozumi, K. Yamada, T. Miyasaka, S. Sumi and Y. Seki, "Reliability of Power Cycling for IGBT Power Semiconductor Modules," IEEE Transactions on Industry Applications, vol. 39, pp. 665-671, 2003.

[33] J. Naderman and R. T. H. Rongen, "Thermal Resistance Degradation of Surface Mounted Power Devices During Thermal Cycling," Microelectronics Reliability, Vol. 39, pp. 123-132, 1999.

[34] B. Baliga, "Temperature Behavior of Insulated Gate Transistor Characteristics," Solid-State Electronics, Vol.28, pp.289-297, 1985.

[35] S. Pendharkar, M. Trivedi, and K. Shenai, "Electrothermal Simulations in Punch Through and Non-Punch Through IGBT's," IEEE Transactions on Electron Devices, vol.45, pp.2222-2231, 1998.

[36] R. Schmidt and U. Scheuermann, "Using the Chip as a Temperature Sensor — The Influence of Steep Lateral Temperature Gradients on the $V_{CE}(T)$ Measurement," Proceedings of the IEEE Power Electronics and Applications Conference, 2009.

[37] V. Chandola, A. Banerjee, and V. Kumar, "Anomaly Detection - A Survey," ACM Computing Surveys, vol. 41, no. 3, Article 15, 2009.

[38] K. Rothenhagen and F. Fuchs, "Performance of Diagnosis Methods for IGBT Open Circuit Faults in Voltage Source Active Rectifiers," Proceedings of the IEEE Power Electronics Specialists Conference, pp. 4348-4354, 2004.

[39] T. Aoki, "A Discussion on the Temperature Dependence of Latch-Up Trigger Current in CMOS/BiCMOS Structures," IEEE Transactions on Electron Devices, Vol. 40, No. 11, pp. 2023-2028, 1993.

[40] S. Kumar, T.W.S. Chow, M. Pecht, "Approach to Fault Identification for Electronic Products Using Mahalanobis Distance," IEEE Transactions on Instrumentation and Measurement, vol.59, pp.2055-2064, 2010.

[41] R. De Maesschalck, D. Jouan-Rimbaud, and D. Massart, "The Mahalanobis Distance," Chemometrics and Intelligent Laboratory Systems, vol. 50, pp. 1-18, 2000.

[42] L. Nie, M. Azarian, M. Keimasi, and M. Pecht, “Prognostics Of Ceramic Capacitor Temperature-Humidity-Bias Reliability using Mahalanobis Distance Analysis, Circuit World, vol. 33, pp. 21-28, 2007.

[43] G. Box and D. Cox, “An Analysis of Transformations,” Journal of the Royal Statistical Society. Series B (Methodological), vol. 26, pp. 211–252, 1964.

[44] M. Held, P. Jacob, G. Nicoletti, P. Scacco, and M.H. Poech, “Fast Power Cycling Test for Insulated Gate Bipolar Transistor Modules in Traction Application,” International Journal of Electronics, vol. 86, pp. 1193-1204, 1999.

[45] G. Coquery, G. Lefranc, T. Licht, R. Lallemand, N. Seliger, and H. Berg, “High Temperature Reliability on Automotive Power Modules Verified by Power Cycling Tests up to 150°C,” Microelectronics Reliability, vol. 43, pp. 1871-1876, 2003.

[46] M. Orchard and G. Vachtsevanos, “A Particle Filtering Approach for On-Line Fault Diagnosis and Failure Prognosis,” Transactions of the Institute of Measurement and Control, vol. 31, pp. 221-246, 2009.

[47] B. Saha, K. Goebel and J. Christophersen, “Comparison of Prognostic Algorithms for Estimating Remaining Useful Life of Batteries”, Transactions of the Institute of Measurement & Control, vol. 31, pp. 293-308, 2009.

[48] M. Arulampalam, S. Maskell, N. Gordon and T. Clapp, “A Tutorial on Particle Filters for Online Nonlinear/Non-Gaussian Bayesian Tracking,” IEEE Transactions on Signal Processing, vol. 50, pp. 174–88, 2002.

[49] M. Ciappa and M. Fichtner, "Lifetime Prediction of IGBT Modules for Traction Applications," Proceedings of the IEEE International Reliability Physics Symposium, pp.210-216, 2000.

[50] V. Sankaran, C. Chen, C. Avant and X.Xu, "Power Cycling Reliability of IGBT Power Modules," Proceedings of the IEEE Industry Applications Conference, pp.1222-1227, 1997.